Title

The Submesoscale in Salinity-Stratified Oceans: Dynamics and Climate Change Impacts

Permalink

https://escholarship.org/uc/item/053656xd

Author

McKie, Taylor

Publication Date

2024

Peer reviewed|Thesis/dissertation

UNIVERSITY OF CALIFORNIA SAN DIEGO

The Submesoscale in Salinity-Stratified Oceans: Dynamics and Climate Change Impacts

A dissertation submitted in partial satisfaction of the requirements
for the degree Doctor of Philosophy

in

Oceanography

by

Taylor McKie

Committee in charge:

Professor Andrew Lucas, Chair
Professor Jennifer Burney
Professor Sarah Giddings
Professor Jennifer MacKinnon
Professor Katharine Ricke

2024

The dissertation of Taylor McKie is approved, and it is acceptable in quality and form for publication on microfilm and electronically.

University of California San Diego

2024

TABLE OF CONTENTS

LIST OF FIGURES

LIST OF TABLES

ACKNOWLEDGEMENTS

I would like to acknowledge Professor Andrew Lucas for his support and training over the years. I’ve learned so much from his guidance and wisdom, especially when it comes to approaching and understanding our data. His questions and constructive feedback always pushed my research exactly where it needed to go, and this work has seen substantial improvements because of him. I’m also very grateful to have had an advisor that supported of all my endeavors outside of research and encouraged my creativity and academic freedom within research.

I would also like to acknowledge Professor Jennifer MacKinnon for her consistent support, presence, and care. Her guidance was instrumental to my dissertation and development as a scientist and because of her support, I believe I was able to reach this milestone. I’ve learned a lot from her insights and compassionate leadership, and I could only wish to resemble just a fraction of the mentor she is to me and so many others.

I would also like to acknowledge the remainder of my committee, for their guidance and support throughout this process. To Professor Katharine Ricke, thank you for your guidance and support as a GPS Science Policy Fellow and for including me in your work and publications. To Professor Sarah Giddings, thank you for your teachings during my first year and for your guidance on my dissertation throughout this process. To Professor Jennifer Burney, thank you for inspiring me to consider policy and for your constant support and encouragement.

I would like to acknowledge my co-authors, Dr. Leah Johnson and Dr. Tamara Schlosser, for their support and guidance for the first chapter of this dissertation. This work could not have advanced without them, and I appreciate their patience and willingness to take the time to meet with me, answer my many, many questions, and run many, many model simulations.

I would like to acknowledge everyone in the Multiscale Ocean Dynamics Lab (MOD) at Scripps, for their work in designing, building, and deploying the extraordinary instruments that provided the data presented in this dissertation. I would also like to thank them for all of their support over the years in the form of technical advice, feedback, and friendly faces. Thank you for always making me feel at home at Scripps.

To my community at Scripps, thank you all for being amazing colleagues and friends. The first couple years with my CASPO cohort and experiences with friends in GPSA-Climate Action and Policy Committee were formative, and much in part to the way many of them inspired me with their curiosities and brilliance. To my community at UCSD as a whole, in particularly the Black Graduate community, thank you for being my support system and second family. Your presence and friendships brought me through the more difficult times of this journey, and I will cherish the memories and friendships from this community for a lifetime.

To my family, thank you for all your love, support, and encouragement throughout my life and within this process. I’m very grateful to have a family that has cheered me on every step of the way. To my parents, thank you for instilling a sense of confidence in me from a very young age, that I could do anything I set my mind to. Thank you for all the sacrifices you made so that I could live a life achieving my goals and dreams. Thank you for getting me through the more difficult periods of this journey with your gentle encouragement and reminding me why I’ve worked towards this goal. I would have never gotten to this point in my education and career without you all.

And to my partner JoJo, thank you for your love and support throughout my graduate career, especially the latter half. As a founding member of the Black Graduate and Professional Student Association, you set the tone for my doctoral journey, creating a support network and community that carried me and so many others through UCSD. And later as my partner, you brought joy and friendship to my life. It is difficult to imagine getting through this last phase of my Ph.D. without you. My last year was one of the most arduous in completing my dissertation, but with you, you made it easy with your loving companionship, generous and selfless partnership, technical support, moments of laughter and fun, shoulders to cry on, and of course, nutritional support.

Chapter 1, in full, has been submitted for publication of the material as it may appear in Journal of Geophysical Research: Oceans 2024. McKie, Taylor; Johnson, Leah; Schlosser, Tamara; MacKinnon, Jennifer; Lucas, Andrew, Wiley Online Library, 2024. The dissertation author was the primary investigator and author of this paper. This work was supported by Office of Naval Research Grants N00014-17-1-2511 and ONR N00014-17-1-2391. This material is also based upon work supported by the National Science Foundation Graduate Research Fellowship Program under Grant No. DGE-2038238. Any opinions, findings, and conclusions or recommendations expressed in this material are those of the author(s) and do not necessarily reflect the views of the National Science Foundation. The authors would like to express gratitude towards the science party and crew of the Summer 2019 ASIRI MISO-BoB Cruise onboard R/V Sally Ride as well as all technical staff with the Multiscale Ocean Dynamics Laboratory at Scripps Institution of Oceanography and Woods Hole Oceanographic Institution (WHOI) for their work and contributions in collecting and managing the in-situ data. We would especially like to thank Tom Farrar and the Upper Ocean Processes Group at WHOI for their contributions and efforts towards DBASIS.

Chapter 2, in full, is a reprint of the material as it appears in Journal of Geophysical Research: Oceans 2024. McKie, Taylor; Lucas, Andrew; MacKinnon, Jennifer, Wiley Online

Library, 2024. The dissertation author was the primary investigator and author of this paper. This work was supported by Office of Naval Research Grants N00014-17-1-2511 and ONR N00014-17-1-2391. This material is also based upon work supported by the National Science Foundation Graduate Research Fellowship Program under Grant No. DGE-2038238. The authors would like to express gratitude towards the science party and crew of the Summer 2019 MISO-BoB Cruise onboard R/V *Sally Ride* as well as all technical staff with the Multiscale Ocean Dynamics Laboratory at Scripps Institution of Oceanography and Woods Hole Oceanographic Institution for their work and contributions in collecting and managing the in-situ data. We would also like to thank Dan Rudnick for his help in carrying out the Omega equation calculations. Finally, we would like to thank two anonymous reviewers for ideas and suggestions that helped improve the paper.

Chapter 3, in part, is currently being prepared for submission for publication of the material. McKie, Taylor; MacKinnon, Jennifer; Ricke, Katharine; Lucas, Andrew. The dissertation author was the primary investigator and author of this paper. This material is also based upon work supported by the National Science Foundation Graduate Research Fellowship Program under Grant No. DGE-2038238. We’d also like to acknowledge Professor Sarah Giddings for her support and guidance in the drafting of this chapter.

VITA

2017	Bachelor of Science in Environmental Engineering, Georgia Institute of Technology
2019-2024	Graduate Research Assistant, Scripps Institution of Oceanography, University of California San Diego
2024	Doctor of Philosophy in Oceanography, Scripps Institution of Oceanography, University of California San Diego

PUBLICATIONS

McKie, Taylor, Andrew J. Lucas, and Jennifer MacKinnon. "Submesoscale dynamics in the Bay of Bengal: Inversions and instabilities." Journal of Geophysical Research: Oceans 129.3 (2024): e2023JC020563.

ABSTRACT OF THE DISSERTATION

The Submesoscale in Salinity-Stratified Oceans: Dynamics and Climate Change Impacts

by

Taylor McKie

Doctor of Philosophy in Oceanography

University of California San Diego, 2024

Professor Andrew Lucas, Chair

This dissertation explores submesoscale dynamics in salinity-stratified oceans that are strongly influenced by freshwater input through rivers and storms. The submesoscale describes a regime of dynamics that occur at lateral scales of *O*(1-10 km), where the planetary vorticity is in balance with the relative vorticity of the flow, and are typically associated with fronts and filaments. At these scales, vertical velocities, facilitated by various instabilities, become large leading to the vertical exchange of heat, salt, and nutrients within the ocean boundary layer. The first chapter observes patchy rain on an ocean that varies in stratification using high-resolution in-situ observations and satellite data in the Bay of Bengal. Inspired by the spatial variability of the rain and surface ocean, we investigate the relative impacts of 1-D processes on frontogenesis using a general ocean turbulence model. The results of this chapter suggest that rain can be conditionally frontogenetic with implications for small-scale instabilities. The second chapter captures these small-scale instabilities in action through high-resolution in-situ observations of the subduction of a cold and salty filament in the Bay of Bengal. Through a stability analysis, we discover the importance of small-scale lateral temperature variability, creating inversions within barrier layers facilitated through symmetric and inertial instabilities and secondary circulations. The third chapter focuses on the temporal evolution of the mesoscale in the Gulf of Mexico, which cascades to the submesoscale, and shifting dynamics in the Loop Current region. A novel analysis of satellite-derived products reveals changes in Loop Current behavior and justification for an increasingly energetic basin. The results suggest that recent years have witnessed prolonged Loop Current retracted phases due to large cyclonic eddies while increases in the kinetic energy of the basin may be attributed to increases in sea level anomalies. In the Bay of Bengal, the findings of this dissertation can improve our understanding of air-sea interactions and support the parameterization of models for monsoon forecasting. In the Gulf of Mexico, the results highlight possible shifts in circulation patterns, important to the transport of biological, chemical, and thermal properties throughout the basin.

Chapter 1 PRECIPITATING FRONTS ON THE BAY OF BENGAL

1.1 Introduction

Freshwater influx into basins, especially those that are salinity-stratified, act to strengthen the stability of the water column, enhance lateral variability, modify the surface velocity field, shoal the mixed layer depth, suppress the vertical mixing of heat and momentum, and impact boundary layer turbulence (Sengupta et al., 2006; Krishnamohan et al., 2019; Shcherbina et al., 2019). Precipitation, as the freshwater input, creates thin and highly stratified “lenses” or “slippery layers” that can sustain for hours at the surface before mixing down into the interior (Soloviev et al., 2015; Shcherbina et al., 2019; Thompson et al., 2019; Iyer & Drushka, 2021; Shackelford et al., 2022). Through wind and the lateral advection of these layers, near-surface currents are generated within the time and spatial scales that allow for interactions with the submesoscale (Kudryavtsev & Soloviev, 1990; Wijesekera et al., 1999; Shcherbina et al., 2019; Laxague & Zappa, 2020; Reverdin et al., 2020; Moulin et al., 2021). The submesoscale resides on spatial scales of *O*(1-10 km) and are characterized by motions at which the relative vorticity is the same order as the planetary vorticity, resulting in the slumping of horizontal density gradients and generating vertical exchange between the surface waters and the interior (Boccaletti et al., 2007; Thomas et al., 2008; Spiro Jaeger & Mahadevan, 2018; Gula et al., 2022). The instabilities that occur along submesoscale fronts allow for the forward cascade of energy from the mesoscale to turbulence and dissipation (McWilliams, 2016; Sarkar et al., 2016). Precipitation could create shallow mixed layers in frontal regions that are sensitive to heating and cooling, prompting a rapid response in sea surface temperature (SST). Cooling of these shallow layers may result in the restratification of fronts through temperature compensation (Tozuka & Cronin, 2014; Spiro

Jaeger & Mahadevan, 2018). Rain layers have also been found to be characteristic of buoyant gravity currents (Wijesekera et al., 1999; Shcherbina et al., 2019; Laxague & Zappa, 2020; Moulin et al., 2021). These are a few processes in which precipitation may influence the interactions between the ocean and atmosphere at the submesoscale (Thomas et al., 2008; MacKinnon et al., 2016; Mahadevan et al., 2016).

The Bay of Bengal (BoB) is a salinity-driven region where it may be particularly important to consider these dynamics, as it experiences an abundance of submesoscale features from its relatively higher frontogenesis potential and a significant freshwater input from riverine runoff and precipitation (Sengupta et al., 2006; MacKinnon et al., 2016; Mahadevan et al., 2016; Jaeger et al., 2020). Models have indicated that regions with shallow salinity stratification tend to warm significantly through surface heat fluxes and vertical mixing, which creates ideal conditions for monsoon formation in the BoB (Vinayachandran et al., 2002; Krishnamohan et al., 2019). Atmospheric convection is largest in the tropics due to high surface temperatures and results in high precipitation contributing to the monsoon, which in turn contributes to surface freshening (Shenoi et al., 2002; Vinayachandran et al., 2013). While 60% of the freshwater impacting the surface advects from the Ganges-Brahmaputra-Meghna and Irrawaddy River systems to the center of the BoB, precipitation also significantly freshens the surface waters (Sengupta et al., 2006; Papa et al., 2010; Mahadevan et al., 2016; Sengupta et al., 2016).

Rain events throughout the Bay can be characterized as convective or stratiform. Convective rain events are caused by thermally induced diurnal circulations and occur on smaller spatiotemporal scales. They typically produce intense rain rates, some reaching up to 100 mm/hr (Liu et al., 2008; Iyer & Drushka, 2021). On the other hand, stratiform rain is generated by remote convection and large-scale atmospheric dynamics. This type has a longer duration and less intense rain rates (Tokay & Short, 1996; Iyer & Drushka, 2021). The differences in the rain rates and duration of these events lead to differential responses in the surface ocean. The response is also dependent on other parameters including wind speed, temperature of the rain, the structure of the surface ocean, and time of day (Iyer & Drushka, 2021). Wind influences the rate at which the fresh, stratified layer is eroded. A higher wind stress at the surface will generate more turbulence, deepening the mixed layer faster and shortening the lifespan of the fresh layer (Drushka et al., 2016, 2019; Iyer & Drushka, 2021).

Near-surface, pre-existing stratification is influential, as stratification created by rain superimposed on a strongly stratified region can dampen the deepening of the fresh layer (Iyer et al., 2021; Shackelford et al., 2022). Precipitation can also lead to complex stratification and generate a layer between the highly stratified halocline and the thermocline below, typically called the barrier layer. The barrier layer can form through buoyancy input at the surface from rain or through advection of the fresh slippery layer (Thadathil et al., 2002). It can be relatively warmer than the surface during periods of cooling and the suppression of mixing by the halocline allows for the barrier layer to maintain its heat (Thadathil et al., 2002; Sengupta et al., 2016; Spiro Jaeger & Mahadevan, 2018). This layer reduces entrainment cooling from beneath the thermocline, resulting in elevated surface temperatures (Veneziani et al., 2014; Sengupta et al., 2016). Frontal regions can also create thick barrier layers beneath their shallow haloclines, inhibiting homogenized mixing throughout the boundary layer (Veneziani et al., 2014; McKie et al., 2024). Ultimately, the modification of the upper ocean heat budget by the barrier layer allows for the regulation of the intraseasonal oscillations of the monsoon and the intensification of cyclones (George et al., 2019; Thadathil et al., 2016; Balaguru et al., 2012; Yu & McPhaden, 2011). Eventually, convection penetrates and erodes the stratification of a rain generated halocline, mixing the freshwater down into the interior (Drushka et al., 2019).

Though the literature characterizing precipitation and the submesoscale in the Bay of Bengal is extensive, the dynamics are evaluated separately, with the exception of the advection of rain or river runoff enhancing lateral variability. Given our recent observations of precipitation directly interacting with the submesoscale presented here and in McKie et al. (2024), it is apparent that these dynamics ought to be considered when improving models. Current models mischaracterize the depth and lateral variability of the mixed layer, simplify and underestimate salinity-stratification, disregard 3-dimensional processes, and lack the resolution needed to sufficiently describe observed thermohaline variability at the surface (Benshila et al., 2014; Chowdary et al., 2016; Lucas et al., 2016; Sengupta et al., 2016). Parameterizing the submesoscale, with the consideration of precipitation, may improve the predictions for the onset and duration of the monsoon. This would be especially imperative given that this region is becoming more susceptible to increased rainfall due to a changing climate (Goswami et al., 2006; Kumar et al., 2011; Mishra et al., 2019; Goswami et al., 2021).

This study explores one-dimensional impacts of precipitation on a salinity-stratified boundary layer through observations and idealized modeling, then considers the potential implications of these findings on variability in lateral buoyancy gradients in the surface ocean. The motivating observations and instrumentation used will be illustrated and described in Section 1.2. Section 1.3 will detail the idealized model design, parameterizations, theoretical framework for model evaluation, and model results. Section 1.4 will discuss the observational and modeling results, implications on lateral variability, and limitations. Concluding statements will be presented in Section 1.5.

1.2 Observations and Motivation

During the summer 2019 cruise of the Office of Naval Research Funded Research Initiative: Monsoon Intraseasonal Oscillations in the Bay of Bengal (MISO-BOB) on board R/V *Sally Ride*, we collected 31 days of high-resolution measurements from multiple instrument platforms in both the upper ocean and lower atmosphere in the Northern BoB. The overall objective of the project was to improve the monsoon predictions through a better understanding of upper ocean processes. Specifically, the fieldwork was organized to investigate the evolution of the ocean surface boundary layer in response to MISO events, characterize the evolution of near-surface fronts, stratification, SST, and explore the resulting air-sea interactions (Wijesekera et al., 2016; Shroyer et al., 2021). Throughout the cruise, a coastally-upwelled, cold and salty filament was tracked by the ship as it advected between two mesoscale eddies, being pulled into the Central BoB between the latitudes of 15N and 18N and longitudes of 87E and 90E as shown in Figures 1-1 and 1-2(a). The following observations are a subset of the observational survey, representing four days of data (July 15th - July 18th) through both in-situ and satellite measurements.

1.2.1 Instrumentation and Measurements

Much of the filament was captured in-situ by the shipboard high-resolution FastCTD profiler, complemented by the Drogued Buoy Air-Sea Interaction System (DBASIS) that drifted along with eastward-flowing mesoscale currents for the duration of the cruise. The FastCTD was equipped with SBE49 temperature, conductivity, pressure, and backscatter sensors. It was towed by the ship between speeds of 2 and 5 knots and is profiled down to 200 meters depth with about a 2-minute duration for each cast. This allowed for a horizontal resolution of 200 m between profiles. Data from each profile was averaged into 1-meter bins. Throughout the entire survey, the FastCTD was cast to a total of 12,051 profiles, of which the data presented here (391 profiles) represents a small subset.

The Drogued Buoy Air-Sea Interaction System (DBASIS) is a joint instrument package between Scripps Institution of Oceanography and Woods Hole Oceanographic Institution. DBASIS consists of a surface buoy collecting high-quality meteorological and surface ocean data, an ocean-wave-powered Wirewalker (WW) vehicle profiling between the surface and 100-meter depths (Pinkel et al., 2011), and RBR Solo temperature sensors attached to a line extending 100 meters below, spaced every 9-10 meters. Three DBASIS systems were deployed during this cruise, but this study will feature approximately 3 days of profiles from one of the systems that was deployed for a total of 17 days. The Wirewalker provided vertically well-resolved profiles of temperature, salinity, velocity, and bio-optical properties every ~10 min (Zheng et al. 2022). The DBASIS system was drogued at depth to follow the mesoscale flow. During the segment of the deployment described here, typical drift speeds were 0.18 m/s, leading to a horizontal spacing between profiles of 200 meters or less. Data were averaged into 0.25 m bins. Meteorological data from the surface buoy was averaged to a temporal resolution of 1 minute, equating to a horizontal resolution averaging approximately 10 meters along the drift path.

1.2.2 Satellite and In-Situ Observations

On July 17th around 9:00 UTC, an atmospheric cold pool event advected westward over the observed region and resulted in strong precipitation on the ocean surface, as illustrated in Figure 1-1 (DMI COI, 2007; Huffman et al., 2019). This event can be characterized as a convective rain event because of its relatively short duration and large peak precipitation rate of 100 mm/hr measured by DBASIS. The cumulative precipitation exhibits spatial variability on the

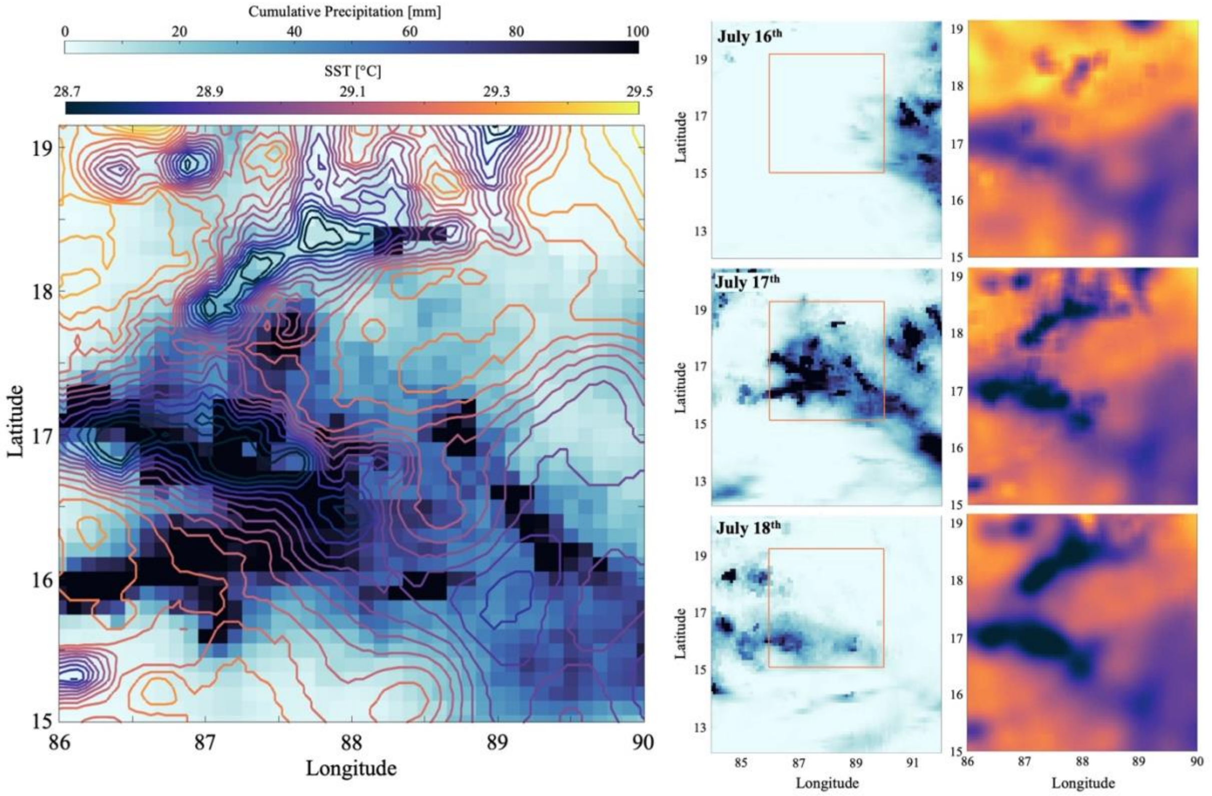

Figure 1-1. Daily accumulated precipitation and SST. The three middle panels show the westward advecting cold pool event with accumulated precipitation data from Global Precipitation Measurement IMERG for July 16th -18th (Huffman et al., 2019). The three right-most panels illustrate the cold filament with satellite SST reanalysis within the region outlined by the orange boxes for July 16th -18th (DMI COI, 2007). The left-most panel depicts the accumulated precipitation superimposed with SST contours at 0.05°C intervals in the region outlined by the orange box on July 17th.

scale of *O*(10-100 km). The lateral variability of SST becomes patchy and intricate on July 17th, with the lateral boundaries of the cold filament becoming more defined, while the surface becomes incrementally colder. Gradients in cumulative precipitation and SST appear to be in alignment around the filament. On July 18th, as the storm system propagates away from our observed region, the sharp lateral temperature gradients at the surface relax, but appear to be stronger and more pronounced than their original surface variability on July 16th.

The shipboard FastCTD and DBASIS captured regions of the filament both prior to and following the rain event. This subset of the survey and density profiles from these instruments are depicted in Figure 1-2. Though somewhat aliased in space and time, these snapshots of events depict the relationship between precipitation, 1-dimensional, and 3-dimensional dynamics motivating our research questions. Figure 1-3 illustrates surface forcing and thermohaline variability of the boundary layer from DBASIS before and after the rain event. As the WW advected through the filament at the start of this time series, the maximum observed surface salinity was 33.8 psu and the corresponding surface temperature was 28.9ºC. These properties were nearly homogeneous throughout the mixed layer (defined in Appendix A), extending down 30 to 40 meters depth. The wind speed remained relatively consistent at approximately 5 m/s. The surface properties became warmer and fresher over the course of four days as the WW drifted into the proximal ambient water. Immediately prior to the rain event, the surface had a salinity signature of 33.3 psu and temperature signature of 29.4ºC, as measured by the buoy at 1.5 meters depth. This was relatively consistent throughout the mixed layer, which had shoaled to 15 meters depth. Vertical shear in horizontal velocity was concentrated at the base of the mixed layer. There was a barrier layer approximately 15 meters thick beneath the warm mixed layer (30 m deep).

Both sensors on the DBASIS buoy and onboard the ship measured the commencement of rain at 9:00 UTC. DBASIS, located approximately 10 km away from the ship during the onset of the precipitation, measured a peak rain rate of 100 mm/hr (Figure 1-3). According to both platforms, the precipitation lasted approximately 3 hours, with the total rainfall observed nearing 100 mm. Satellite observations were consistent with the in-situ measurements (Figure 1-1). During the rain event, the winds fluctuated between 5 and 18 m/s, reaching a maximum during the peak rain rate and gradually decreasing following the rain event. A cold and fresh puddle began to form at the surface, which eventually penetrated to 5 meters depth 3 hours after the

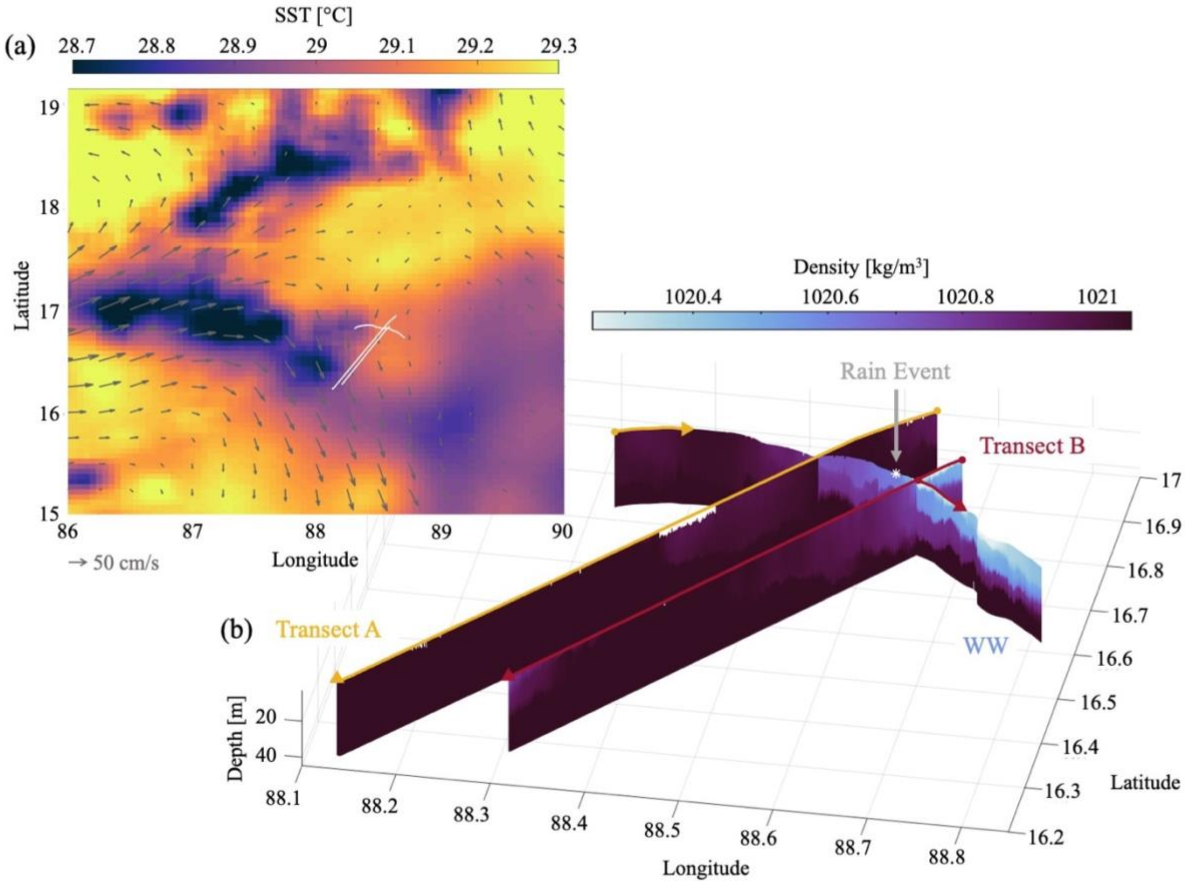

Figure 1-2. Boundary layer properties of the survey subset. The plane view map in (a) shows the SST for July 17th and the Wirewalker and FastCTD tracks for July 15th -18th are traced in white (DMI COI, 2007). The gray arrows represent geostrophic velocity (Dohan, 2021). The in-situ density profiles of the tracks are detailed in (b). Transects A and B represent the FastCTD tracks. Transect B is offset longitudinally to the right by 0.1° for visualization purposes. The yellow and red arrows above the profiles represent the tracks of the WW and FastCTD during the measurements of Transect A and Transect B, respectively. The arrows denote the direction of travel. The white star indicates the position of the WW during the onset of the rain event.

onset of the rain event and 10 meters depth after 15 hours. The strong, yet shallow halocline created by the rain defined the new mixed layer base. DBASIS measured the surface salinity to be 32.4 psu directly following the rain event, and our estimates confirm that 100 mm of rainfall would drop the salinity from 33.3 psu to approximately 32.6 psu within the top 5 meters (not shown). The warmer, ambient water of the mixed layer prior to the rain event became a warm subsurface layer about 15 meters thick and could be considered an additional barrier layer. This warm subsurface layer was observed for about 15 hours. Stratification became complex, with

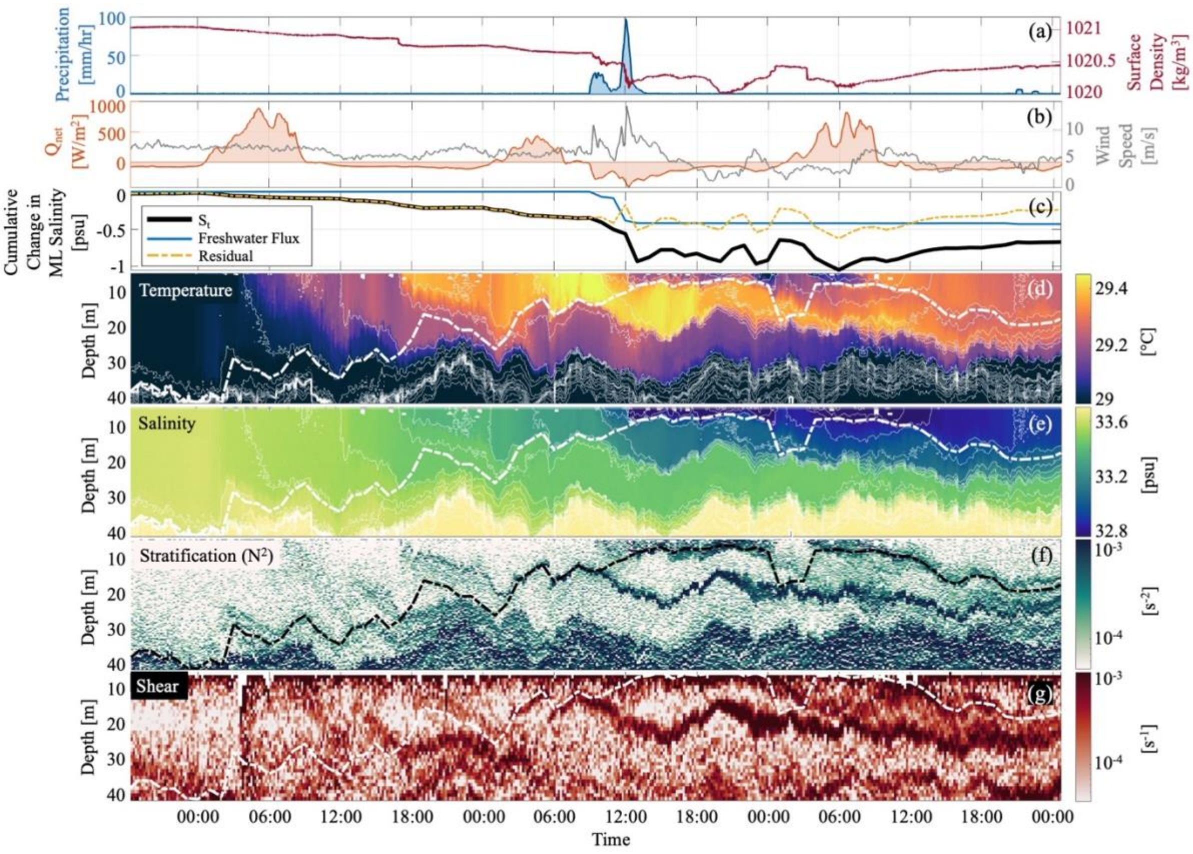

Figure 1-3. Mixed layer variability, surface fluxes, and mixed layer salt budget estimates derived from DBASIS for July 15th -18th, 2019. (a) Precipitation (blue, left y-axis) and surface density at 1.52 meters depth (red, right y-axis). (b) Net surface heat flux, Q_{net} (orange, left y-axis) and wind speed (gray, right y-axis). (c) Cumulative change in the mixed layer salinity and its components as described by the legend and in Appendix A. (d) and (e) Temperature and salinity measured by the Wirewalker, respectively. The white lines represent isopycnals at 0.1 kg/m^3 intervals. (f) Stratification (log-scaled) (g) Vertical velocity shear. The thick, black and white dot-dashed lines in (d)-(g) represent the mixed layer depth.

multiple highly stratified layers beneath the rain puddle— the thick warm subsurface layer and the relatively colder layer above the thermocline (Figure 1-3). Vertical shear within the halocline and at the base of this warm subsurface layer became elevated, reaching values $O(10^{-4}\ s^{-1})$. In the following hours, the surface became cooler and fresher, reaching a minimum salinity value of 32.2 psu and a minimum temperature value of 28.9°C. Stratification and shear remained strong, and winds decreased to a minimum of 2 m/s.

By July 18th around midnight (UTC), elevated winds (> 5 m/s) accompanied an increase in vertical shear to a maxima of *O*(10^{-3} s^{-1}) beneath the rain puddle and at the base of the barrier layer. The shallow halocline eroded and the mixed layer deepened, allowing for the cold freshwater confined at the surface to mix into the warm layer beneath. The warm subsurface layer began to shrink and both temperature and salinity at the surface were elevated to 29.2ºC and 32.9 psu. The surface became cold and fresh again and the mixed layer shoaled. For the remainder of the WW data subset, the surface values gradually increased and the vertical temperature structure within the boundary layer was intricate and complex, with variability on the order of 0.01ºC and exhibiting several inversion layers with various spice signatures approximately 1 meter thick. A one-dimensional mixed layer salinity budget detailed in Appendix A accompanies these observations and will be explored in the discussion.

The observations from DBASIS share some qualitative features with past observations and modeling results from literature (Drushka et al., 2016; Bellenger et al., 2017; Drushka et al., 2019; Thompson et al., 2019; Iyer & Drushka, 2021; Chi et al., 2023); along with the FastCTD data, they bring a fresh perspective on the role of precipitation in submesoscale dynamics. Preceding and following the rain event, the WW intercepted two of the ship transects within 10 km of each other, illustrated in Figure 1-2(b). This allows for us to observe the pre-existing stratification and structure of the filament prior to the impact of the rain in the FastCTD Transect A and to observe a strong, salinity-driven surface front that appears to be enhanced by rain in the FastCTD Transect B, both illustrated in Figure 1-4. Transect A illustrates a vertically homogeneous mixed layer that varies laterally from 30 to 40 meters depth. There is small scale lateral variability *O*(1 km) in temperature and salinity. The densest region of the filament had a salinity signature of 33.8 psu and a temperature signature of 28.8ºC. Transect B has similar

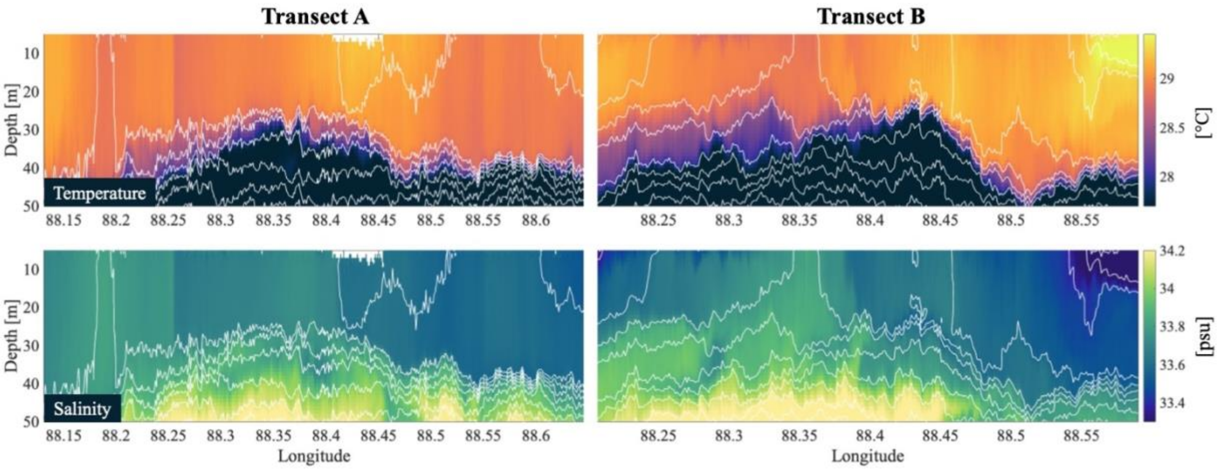

Figure 1-4. Temperature and salinity profiles for Transects A and B collected by the FastCTD system onboard the R/V *Sally Ride*. The top panels are temperature. The bottom panels are salinity. The white lines indicate isopycnal contours at 0.2 kg/m^3 intervals.

properties to Transect A on the western side of the filament but presents a warm and fresh near surface layer with a thin layer of rain above it on the eastern side (Figure 1-5(a)). The near surface layer was set between 5 and 15 meters depth and had a maximum temperature signature of 29.4ºC and a depth average salinity signature of 33.1 psu. Above the near surface layer, the FastCTD captured salinity values as low as 32 psu and temperature averaging 29.2ºC in the rain layer, slightly colder than the near surface warm layer (Figure 1-5(a)). The surface lateral buoyancy gradient with the rain layer was $O(10^{-7}\ \mathrm{s}^{-2})$. This captured region borders the eastern edge of the filament, where rain falls on relatively warm and fresh waters. Satellite measurements indicate that rain also layered the cold and salty filament (Figure 1-1), bringing into question how patchy rain may impact the compensation of lateral thermohaline variability.

Collectively, the satellite and in-situ data demonstrate that the surface lateral variability introduced by precipitation can become pronounced when storm systems exhibit spatial variability or, conversely, when homogeneous precipitation occurs on an upper ocean that varies

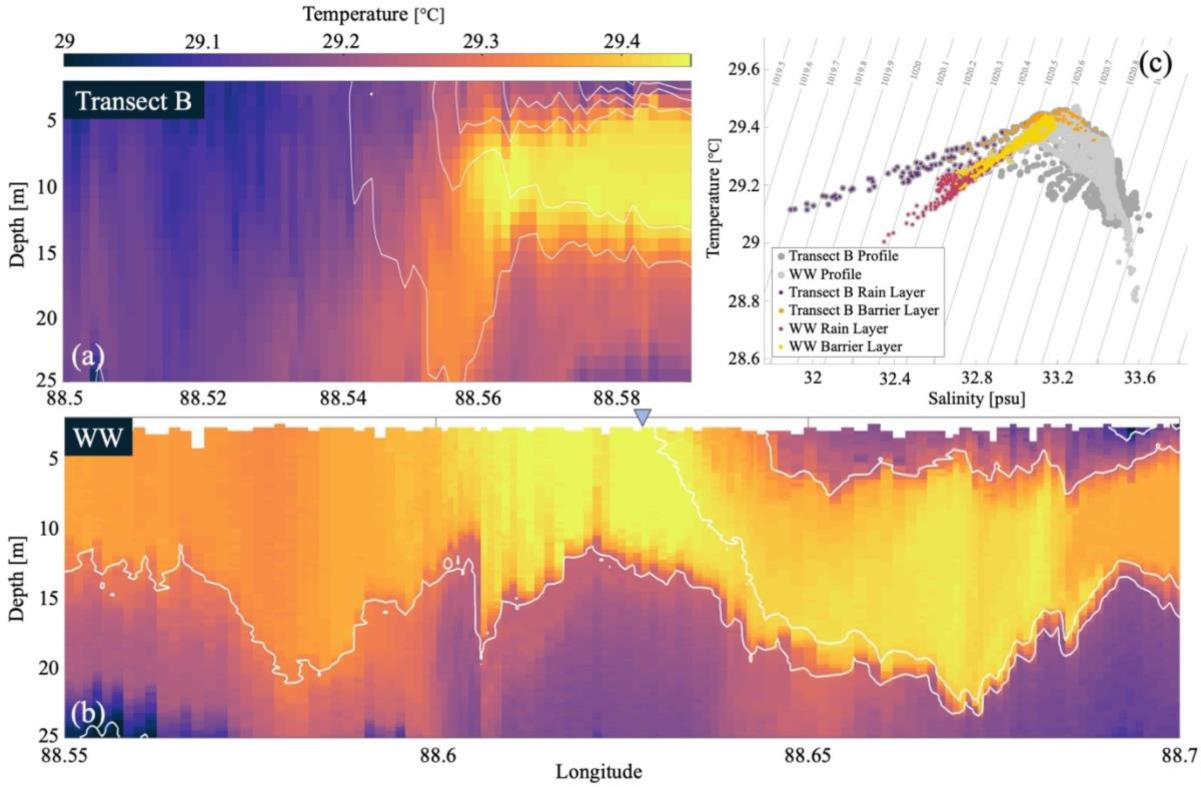

Figure 1-5. Close up on temperature profiles from the FastCTD, Transect B (a) and Wirewalker (b). The white lines indicate isopycnals at intervals of 0.1 kg/m^3. The blue triangle on top of the WW profile indicates the time of the rain event. (c) An accompanying Temperature-Salinity (T-S) diagram illustrates the segmented profiles in T-S space with areas of the rain layers and barrier layers from both instruments highlighted.

in stratification. In a complementary study (McKie et al., 2024), we observe and investigate submesoscale dynamics and instabilities on the eastern edge of this filament in the hours and days that follow, which calls to question whether rain influenced these dynamics. Given the lateral gradients imposed by the rain in Transect B (Figures 1-4 and 1-5) and the satellite data (Figure 1-1), could similar dynamics be enhanced at the edges of these patches? These uniquely captured observations of the evolution of freshwater at the surface and the creation of a submesoscale front set the stage for the following experimental results that could provide more insight into how rain events impact the lateral variability of the surface ocean.

The primary goal of this work is to explore the question of how frontal regions respond to precipitation both initially and over time. We seek to understand this observed phenomenon through idealized modeling and the framework of frontogenetic tendency, defined as the rate of change in the amplitude of the buoyancy gradient (Gula et al., 2014). The analysis will consider the spatial variability of both precipitation and stratification, addressing two questions:

1. How does uniform precipitation on regions with spatially-varying stratification impact frontogenetic tendency?
2. And how does spatially-varying precipitation on regions with uniform stratification impact frontogenetic tendency?

1.3 Modeling Experiment

1.3.1 Idealized Model Set-up

To understand the modification of the vertical structure within the boundary layer due to 1-D surface forcing, we utilized the general ocean turbulence model (GOTM). GOTM is a 1-D water column turbulence model simulating a range of hydrodynamic processes in the upper ocean boundary layer. We employed the K-profile parameterization (KPP) via the baseline configuration of the Community Vertical Mixing Project (CVMix) software package subroutine (Large et al., 1994; Van Roekel et al., 2018; Li et al., 2021). This first-order turbulence scheme compares well to large eddy simulations for a range of surface forcings (Van Roekel et al., 2018). Each simulation was run with Jerlov-IB light extinction coefficients, a timestep of 1 minute, and 0.5 m vertical resolution over the upper 100 m of the water-column with zero bottom roughness at the base of the model domain.

To test whether precipitation on pre-existing stratification, and their spatial variability, impacts the lateral buoyancy gradient at the surface and frontogenetic tendency, we conceived a simple two-box system, in which each box is simulated independently under varying conditions to test different scenarios. The output of each simulation is a time series of temperature and salinity as a function of depth in response to various surface forcing scenarios. These outputs are analyzed in pairs and the surface density signatures in each box are then calculated as a gradient across a nominal 10 km distance as a function of time to understand the implications for lateral variability. This idealized approach intentionally ignores any submesoscale dynamics at play, and instead isolates the potential of different but nearby regions to evolve under varying atmospheric forcing conditions.

For the model initialization, two idealized profiles were created to reflect the observations from Transect A and B: A warm and fresh shallow mixed layer (Shallow ML) and a cold and salty deep mixed layer (Deep ML). To design these profiles, a modified model buoyancy frequency proposed by Lerczak et al. (2001) was implemented and is as followed:

$$N(z) = N_{ML}\frac{1}{2}\left(1+\tanh\left(\frac{z-z_{ML}}{\varepsilon_{ML}}\right)\right)\left(1+e^{\frac{z-z_1}{\delta_{ML}}}\right) \tag{1.1}$$

A table listing the variables used to create these profiles can be found in Appendix B. To create the initial temperature and salinity profiles, surface values resembling the surface properties of Transect A and B initialized the loop at the beginning of the profile, then the stratification was used to iteratively calculate each property at depth. For the shallow ML, which extended to 10 meters depth, the surface temperature value was 29ºC and the surface salinity value was 33.5 psu. For the deep ML, which extended to 50 meters depth, the surface temperature value was 28ºC and the surface salinity value was 34 psu. The resulting stratification was compared to the model stratification for validation.

The surface forcing for the model included idealized time series of precipitation, surface heat fluxes, and wind speed (Appendix C). The magnitudes of these variables were inspired by shipboard and in-situ observations. The precipitation time series featured a Gaussian distribution of rain rate similar to Drushka et al. (2016) and Bellenger et al. (2017). The precipitation commenced an hour after the simulation began and had a duration of two hours. The peak precipitation rates tested were 100 mm/hr, 50 mm/hr, and 0 mm/hr. The evaporation rate was set to zero for the entire simulation. The heat fluxes were idealized for one day and repeated for 5 days. The heat flux due to incoming solar radiation also assumed a Gaussian distribution and had a peak heat flux of 600 W/m^2. The longwave, sensible, and latent heat fluxes remained constant throughout the simulation and were adjusted to allow for the cumulative net heat flux to equal zero over the course of 24 hours. This allows us to focus solely on precipitation as surface forcing. Wind speed was another variable tested, and included constant rates at 2, 5, and 10 m/s. The combination of forcing variables depends on the test case and will be described below.

For impacts on surface lateral variability, three scenarios were considered. Case I addresses the question of how uniform precipitation on regions with spatially-varying stratification impacts frontogenetic tendency, by investigating the laterally-varying implications of simulating the shallow and deep ML profiles with the same surface forcing. The surface forcing included a rain event with a peak rain rate of 100 mm/hr and was tested with each wind speed. A control scenario was designed similar to this case with the same stratification profiles, but without precipitation to understand how the frontogenetic tendency in Case I compares to that of a scenario with no rain.

Case II explores the impact of spatially-varying precipitation on frontogenetic tendency in regions with uniform stratification. This may seem more intuitive than the first case, but the

Table 1-1. Idealized modeling scenario conditions. Peak precipitation rates, P_1 and P_2, have units [mm/hr] and wind speed has units [m/s].

Scenario	**Profile 1**	**Profile 2**	P_1	P_2	**Wind Speed**
Control	Deep ML	Shallow ML	0	0	5
Case I	Deep ML	Shallow ML	100	100	5
Case II	Deep ML	Deep ML	100	0	5

objective here is to estimate the magnitude of the lateral gradients created and observe the behavior of frontogenetic tendency. For Case II, the profiles were simulated with a wind speed of 5 m/s and a peak precipitation rate of 100 mm/hr in one box and 0 mm/hr in the other, representing a region with rain adjacent to a region with no rain. This scenario was also tested with peak precipitation rates of 100 mm/hr and 50 mm/hr (not shown). Table 1-1 summarizes the conditions for each scenario tested and presented in this work.

1.3.2 Frontogenetic Tendency and Vertical Mixing

To quantify the extent at which surface forcing through precipitation impacts the rate of frontogenesis, we followed Capet et al. (2008) and Gula et al. (2014) to express frontogenetic tendency as

$$T = \frac{1}{2}\frac{D\|\nabla_h b\|^2}{Dt} \tag{1.2}$$

where b is buoyancy defined as $b = -g\rho/\rho_o$, where g is gravity, ρ is density, and ρ_o is a reference density. The frontogenetic tendency is composed of four terms:

$$T = T_{adv} + T_w + T_{dv} + T_{dh} \tag{1.3}$$

where T_{adv} is the rate of frontogenesis due to horizontal advection, T_w is the straining deformation by vertical velocity, T_{dv} is the contribution due to vertical mixing, and T_{dh} is the contribution due to horizontal buoyancy diffusion. For the purpose of this study, we will focus on the third term of this equation. Ignoring the advective parts of the material derivative, this term can be expressed as

$$T_{dv} = \nabla_h \left[-\frac{d}{dz}(F_b) \right] \cdot \nabla_h b \tag{1.4}$$

where F_b and is a Fickian turbulent buoyancy flux and is equivalent to $\overline{w'b'}$. From here, we assume that b is vertically uniform within the mixed layer and we evaluate this equation as a bulk mixed layer by vertically integrating from the bottom of the surface mixed layer $(z = -H)$ to the surface $(z = 0)$.

$$\int_{-H}^{0} \frac{1}{2}\frac{d}{dt}[\nabla_h b]^2 dz = \int_{-H}^{0} \nabla_h \left[-\frac{d}{dz}(F_b) \right] \cdot \nabla_h b \, dz \tag{1.5}$$

The base of the mixed layer, H, is defined as the maximum vertical gradient in density at each time step in our model. Evaluating the integral on the right hand side (RHS) gives us

$$\int_{-H}^{0} \frac{1}{2}\frac{d}{dt}[\nabla_h b]^2 dz = [\nabla_h F_b \cdot \nabla_h b]_{z=-H} - [\nabla_h F_b \cdot \nabla_h b]_{z=0} \tag{1.6}$$

where the first term on the RHS represents the buoyancy flux at the base of the mixed layer (entrainment term) and the second term on the RHS represents the buoyancy flux at the surface. The entrainment term is estimated as

$$\nabla_h F_b \cdot \nabla_h b = \left(-K_\psi \frac{\partial \psi}{\partial z} + K_\psi \gamma_\psi \right) \cdot \nabla_h b \tag{1.7}$$

where ψ represents temperature or salinity, K is the turbulent diffusivity, and γ is the non-local transport (Van Roekel et al., 2018). Values of entrainment were evaluated at the depth of vertical buoyancy flux extrema and scalings that reflected the differences in the mixed layer depths between the two simulations were applied. We can simplify Equation 1.6 if we are only concerned with the gradient in one direction, since our two-box model only considers a lateral gradient in the horizontal. So, by applying a gradient in the x-direction only and defining B_o as the buoyancy flux at the surface, we have

$$\int_{-H}^{0} \frac{1}{2}\frac{d}{dt}\left[\frac{db}{dx}\right]^2 dz = \left(\frac{dF_b}{dx}_{z=-H} - \frac{dB_o}{dx}\right)\frac{db}{dx} \tag{1.8}$$

Integrating the left hand side (LHS) and rearrangement yields

$$\frac{d}{dt}\left(\frac{db}{dx}\right)^2 = \frac{1}{H}\left[\frac{dF_b}{dx}_{z=-H} - \frac{dB_o}{dx}\right]\frac{db}{dx} \tag{1.9}$$

Expanding B_o to account for the diurnal cycle (surface heat term) and spatially-varying precipitation (precipitation term) gives us the final form:

$$\frac{d}{dt}\left(\frac{db}{dx}\right)^2 = \frac{1}{H}\left[\frac{dF_b}{dx}_{z=-H} - \frac{d}{dx}\left(g\alpha\frac{Q_{net}}{\rho c_p}\right) - g\beta\left(S\frac{dP}{dx}\right)\right]\frac{db}{dx} \tag{1.10}$$

where α is the thermal expansion coefficient, c_p is the heat capacity for seawater, Q_{net} is the net heat flux, β is the haline contraction coefficient, S is the average salinity of the mixed layer, and P is the precipitation rate. We use this quantity to assess the temporal evolution of the frontogenetic tendency due to vertical mixing in our two-box model simulations. This will also serve as a tool to illustrate how entrainment, surface fluxes, and the shoaling or deepening of the mixed layer relatively contribute to a frontogenetic or frontolytic response.

Equation 1.10 was simplified to its third term and computed for various precipitation rates to determine how different compensation types respond to spatially-varying precipitation and its effect on frontogenetic tendency. This exercise will aid understanding in how precipitation on a pre-existing gradient will have a compensating or reinforcing effect on the surface ocean. We will ignore the entrainment term since compensation is calculated based off an instantaneous response of surface properties to precipitation. Additionally, entrainment is likely to be negligible because precipitation initially strengthens stratification, inhibiting mixing beneath the halocline. The mixed layer depth used in this calculation was 5 meters and a temperature of 19.2ºC was prescribed to the rain. This value was derived from DBASIS surface temperature observations and calculated using conservation of mass. The initial surface values reflected buoyancy gradients of all compensation types. We use Turner angle, Tu, to describe compensation as it has been useful in characterizing horizontal variability (Ruddick, 1983; McDougall et al., 1988; Ferrari & Rudnick, 2000; Rudnick & Martin, 2002; You et al., 2002; Johnson et al., 2016). The compensation types and a description of Turner angle are detailed in Appendix D. The terms 'compensating' and 'reinforcing' are also refined in Appendix D, as their use in this study require distinction from their traditional definitions. The compensation values were selected to be nearly equidistant (within a Turner angle of 1º) from the center of each categorical range such that the initial Turner angles were -68º, -23º, 23º, and 68º. All buoyancy gradients tested have a magnitude of $5 \cdot 10^{-7}$ s^{-2}.

1.3.3 Model Results

1.3.3.1 1-D Impacts of Varying Precipitation and Stratification

We will first detail the 1-dimensional impacts of precipitation on each stratification profile and its response to surface forcing, entrainment, and wind. For the shallow ML simulation with a peak rain rate of 100 mm/hr, the precipitation created a cold and fresh, thin mixed layer within the top 5 meters, as shown in Figure 1-7(b) and (c). The surface temperature immediately after the rain event was 28.7ºC and the surface salinity was 31.2 psu; the stronger impact of freshening on buoyancy led to a decrease in near-surface density. A ~10 meter thick barrier layer was created beneath the rain layer, with a uniform temperature of 29ºC. In the hours following the rain event, the new, thin mixed layer gradually deepened due to wind mixing, approaching the initial mixed layer depth. While saltier water entrains, the mixed layer is also warmed by turbulent heat fluxes from the barrier layer below, and then from solar heating. Five hours after the rainfall ceased (Hour 8), the mixed layer had deepened to its original depth. From this point forward, the mixed layer becomes less buoyant due to both entrainment of cooler and saltier water below and night-time cooling from above. At the end of day one, the cumulative heat from the surface is zero, yet the mixed layer is colder and fresher than its original state. The mixed layer is now a few meters deeper compared to its initial depth and has increased in density relative to its initial state mainly due to the entrainment of cooler and saltier waters.

For the deep ML simulation with a peak rain rate of 100 mm/hr and a constant wind speed of 5 m/s, the precipitation impacted the surface similarly to that of the shallow ML (Figure 1-7(d) and (e)). However, the mixed layer took 4 additional hours (Hour 12) to descend to the original depth prior to precipitation. The surface temperature immediately following the rain was 27.8ºC and surface salinity was 31.7 psu. A slightly warmer barrier layer was also created here, with a relatively uniform temperature of 28ºC. Similar to the shallow ML simulation, the mixed layer was warmed by both the ~40 meter thick barrier layer and diurnal heating in the hours following the rain event, but the entrainment of saltier water was stronger because of the stronger vertical salinity gradient. With the onset of surface cooling, the mixed layer cooled from above, while still being warmed from beneath. By the end of day one, wind and surface cooling had eroded the salinity stratification set by the rain, the mixed layer deepened to its original depth, and the signature of the rain had significantly dispersed within the deeper mixed layer. For the remainder of the simulations for both the shallow and deep MLs, the mixed layers continued to cool from entrainment and the base of the mixed layer continued to deepen. For simulations with no rain, both shallow and deep MLs deepened from their original depths over time and cooled at the base of the mixed layers from entrainment on the time scale of one day or longer (Figure 1-6(b)-(e)).

As demonstrated in previous works, wind speed determines the rate at which the thin and highly stratified surface layer generated by precipitation erodes (Drushka et al., 2016, 2019; Iyer & Drushka, 2021). Our simulations demonstrate that the faster the wind speed, the faster the mixed layer deepens (not shown). For a deep ML with a peak precipitation rate of 100 mm/hr and a constant wind speed of 2 m/s, the mixed layer descended to its original depth approximately 12 hours after the rainfall ceased (Hour 15). The mixed layer also remained shallow within 10 meters until the base eroded. With similar conditions, except at a constant wind speed of 10 m/s, the mixed layer descended exponentially to its original depth 3 hours after the rainfall ceased (Hour 6). For the shallow ML simulations, the mixed layers descended to their original depths 3 hours earlier compared to the deep MLs. This does imply that at a high wind speed, the shallow ML descended to its original depth immediately after the rainfall ceased.

Though these 1-D dynamical results are familiar from literature in a general sense, we still divulge these details to set the stage for the lateral implications of our two-box model. For the following scenarios, each simulation described was run with a constant wind speed of 5 m/s.

1.3.3.2 The Control Simulation

The control simulation allows us to assess the specific impact of precipitation by comparing the control to the other cases. In the control case (Figure 1-6), entrainment led the frontogenetic tendency response, and both deep and shallow MLs cooled from mixing at the base of the mixed layers. The effects of diurnal forcing were felt by each mixed layer profile. In the two-box set up, the imposed lateral gradient became compensated as the cooling in the shallow ML occurred more rapidly relative to the deep, resulting in a frontolytic response. Crucially, the

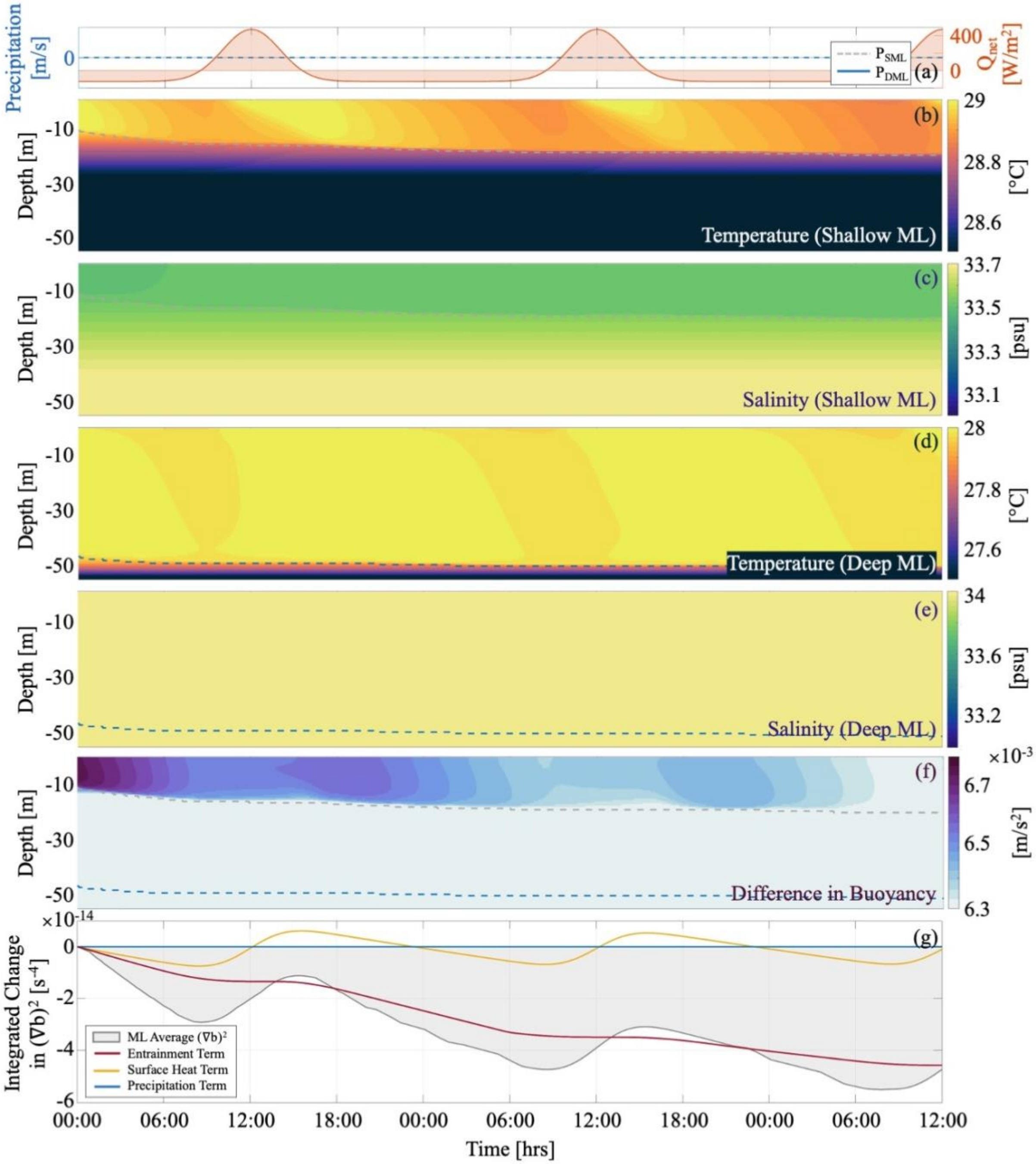

Figure 1-6. Control scenario with simulation profiles. (a) Surface fluxes, P_{SML} and P_{DML} represent the precipitation rate for the shallow and deep MLs, respectively. (b) and (c) Temperature and salinity evolution for the shallow ML. (d) and (e) Temperature and salinity evolution for the deep ML. (f) Difference in buoyancy inferred from the two-box system. (g) Time-integrated frontogenetic tendency with components. The gray and blue dashed lines in (b)-(f) indicate the mixed layer depths corresponding with each rain rate.

lateral gradient is confined to the near surface waters with similar temperature and salinity properties at depth in each box. Hence, vertical entrainment makes the surface layers converge towards each other. Superimposed on this tendency, periods of diurnal heating concentrated buoyancy in the shallow mixed layer at a higher rate relative to the deep, resulting in frontogenetic pulsing (surface heat term, Figure 6(g)). While the frontogenetic response fluctuated, the response over longer timescales was frontolytic due to the entrainment term. The difference in buoyancy near the surface decreased by $4 \cdot 10^{-4}$ m/s^2 over the course of 2 days. This is equivalent to a $O(10^{-8}\ \mathrm{s}^{-2})$ reduction in the lateral buoyancy gradient. The time-integrated frontogenetic tendency decreased by approximately $-5 \cdot 10^{-14}$ s^{-4} within 2 days.

1.3.3.3 Case I

Case I considered the time evolution of the frontogenetic tendency between deep and shallow MLs, both experiencing a peak rain rate of 100 mm/hr, presented in Figure 1-7. Prior to the rain, the deep ML is denser than the shallow ML, as it is both colder and saltier, as can be seen in the initial buoyancy difference between them (Figure 1-7(f)). At the onset of and throughout the rain event, the shoaling of both mixed layers during a period of cooling results in a strong frontolytic response. The precipitation term is zero because the amount of precipitation across the imposed lateral gradient is the same. As the rain begins to stop, entrainment begins to increase. There is differential entrainment between the mixed layers due to a relatively warmer barrier layer in the shallow simulation; the entrainment term becomes leading order shortly after the rain (Figure 1-7(g)). The response is now frontogenetic, as the rain layer in the shallow simulation becomes lighter with the entrainment of warmer water and the rain layer in the deep simulation becomes denser with the entrainment of saltier water. This frontogenetic response continues for hours after the rainfall ceased, with a partial contribution from diurnal heating. The

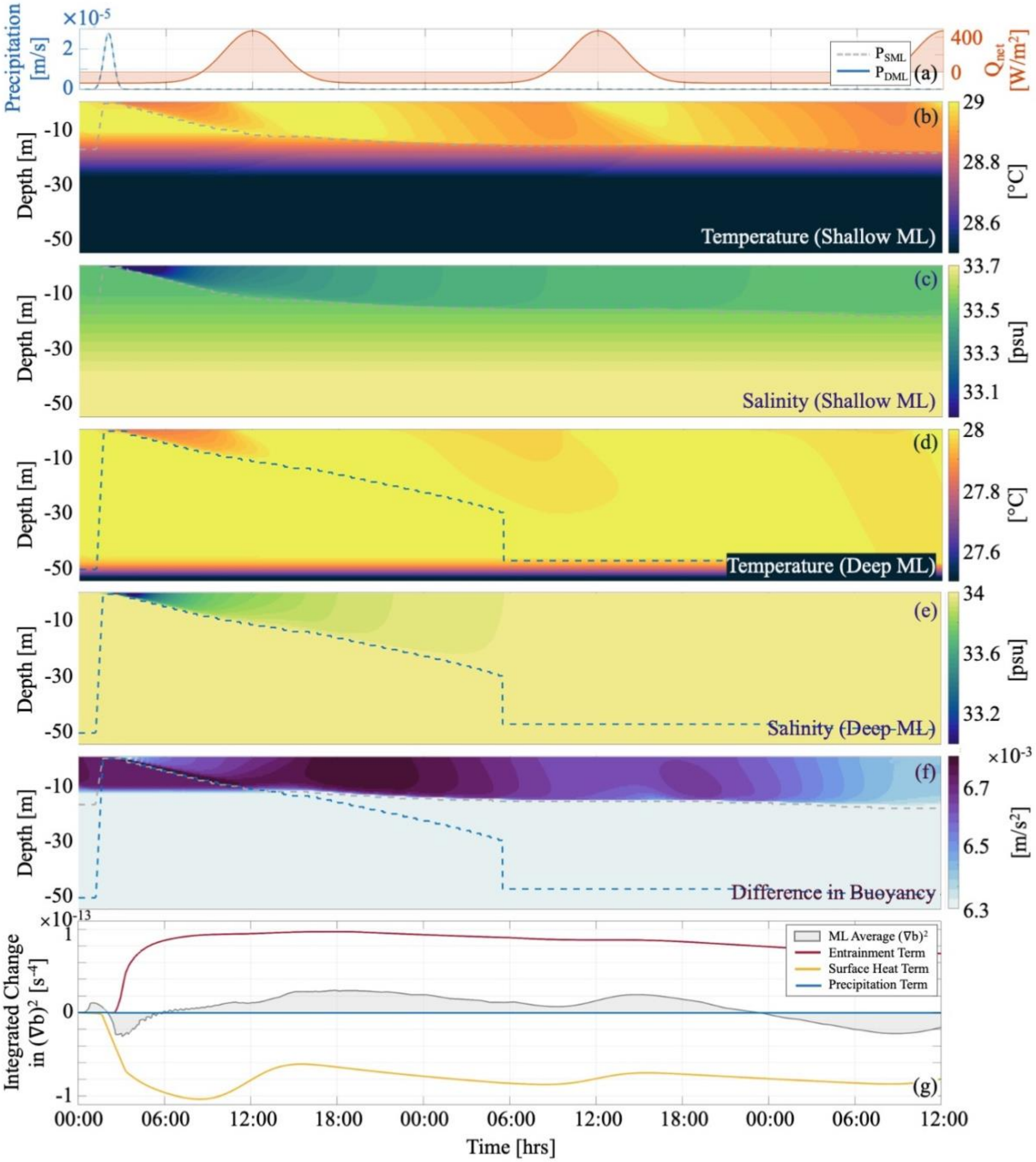

Figure 1-7. Case I scenario with simulation profiles. (a) Surface fluxes, P_{SML} and P_{DML} represent the precipitation rate for the shallow and deep MLs, respectively. (b) and (c) Temperature and salinity evolution for the shallow ML. (d) and (e) Temperature and salinity evolution for the deep ML. (f) Difference in buoyancy inferred from the two-box system. (g) Time-integrated frontogenetic tendency with components. The gray and blue dashed lines in (b)-(f) indicate the mixed layer depths corresponding with each rain rate.

mixed layer continues to warm until surface cooling and cooler waters from entrainment impact the mixed layer, generating a frontolytic response before the 24-hour mark (Figure 1-7(f), (g)). Over the following days, ongoing wind-driven entrainment dominates and cools the shallow ML faster than the deep ML, further compensating and weakening the initially imposed lateral buoyancy gradient.

The net effect of precipitation on an initial front can be seen by comparing this two-box simulation to the control. After 21 hours, the lateral buoyancy gradient for Case I was stronger than its initial gradient and the control was weaker, both by an order of $O(10^{-8}\ \mathrm{s}^{-2})$. Put another way, without rain, and assuming similar temperature and salinity properties in each box below the surface layer, there is a tendency for frontolysis through entrainment that slowly but steadily erases existing lateral gradients, even without 3-D processes involved. With rain, even though the rain is the same on both sides of the front, the net effect of the rain *delays the frontolytic tendency response*. The reason the lateral gradient becomes stronger is related to the effectiveness of the entrainment term. For the box with an initially deep ML, the fresh anomaly is able to be mixed in depth more easily, while for the initially shallow ML, the fresh anomaly stays concentrated for longer in addition to the entrainment of warmer waters. The result is that the initially light, thin ML temporarily becomes more buoyant relative to the deep ML that becomes less buoyant through the entrainment of saltier water. This can be seen in the entrainment term in Figure 1-7(g), which is increasing (frontogenetic) until approximately Hour 18 whereas the entrainment term is strictly decreasing (frontolytic) for the control case (Figure 1-6(g)). After 48 hours, the imposed lateral gradient weakens relative to its original gradient.

To gain an understanding of the time scales of importance, we temporally averaged the frontogenetic tendency for Case I and compared it to the control, as shown in Figure 1-9. On average and neglecting diurnal forcing, Case I was frontogenetic for approximately one day and became frontolytic after, while the control remained frontolytic throughout the whole time series. The effect of diurnal forcing is similar in both cases, creating a pulsing of the lateral buoyancy gradient as heat is trapped in the shallower ML during the daytime. In both the control and Case I, the time-integrated frontogenetic tendency was $O(10^{-14}\ \mathrm{s}^{-4})$, which is considered strong for these spatial scales (Thomas et al., 2013; Gula et al., 2014).

1.3.3.4 Case II

For Case II, we evaluate the frontogenetic tendency when spatially patchy rain falls on a horizontally uniform ocean stratification. The frontogenetic tendency for simulations forced with peak rain rates of 100 and 0 mm/hr was assessed (Figure 1-8), with the zero rain rate in the deep ML acting as a control. The precipitation term dominated the frontogenetic tendency response throughout the rain event (Figure 1-8(g)). There is a strong frontogenetic spike, due to differences in the rain rates. After the rainfall ceased (Hour 3), the entrainment term increased and the response for the remainder of the simulation was frontolytic. The surface heat term is small compared to the precipitation and entrainment terms. The imposed lateral buoyancy gradient during the rain event was $O(10^{-6}\ \mathrm{s}^{-2})$ and was created on the time scale of hours. The time-integrated frontogenetic tendency initially reflects the creation of strong lateral buoyancy gradients associated with patchy rain. After the rain ceases, entrainment dilutes the freshwater anomaly through vertical mixing. This gradually but steadily reduces the buoyancy gradient. The time-integrated frontogenetic tendency reached $O(10^{-12}\ \mathrm{s}^{-4})$ (Figure 1-9). In the scenario with peak precipitation rates 100 mm/hr and 50 mm/hr (not shown), a smaller lateral difference in cumulative precipitation induced a smaller lateral gradient and lower cumulative frontogenetic tendency compared to Case II.

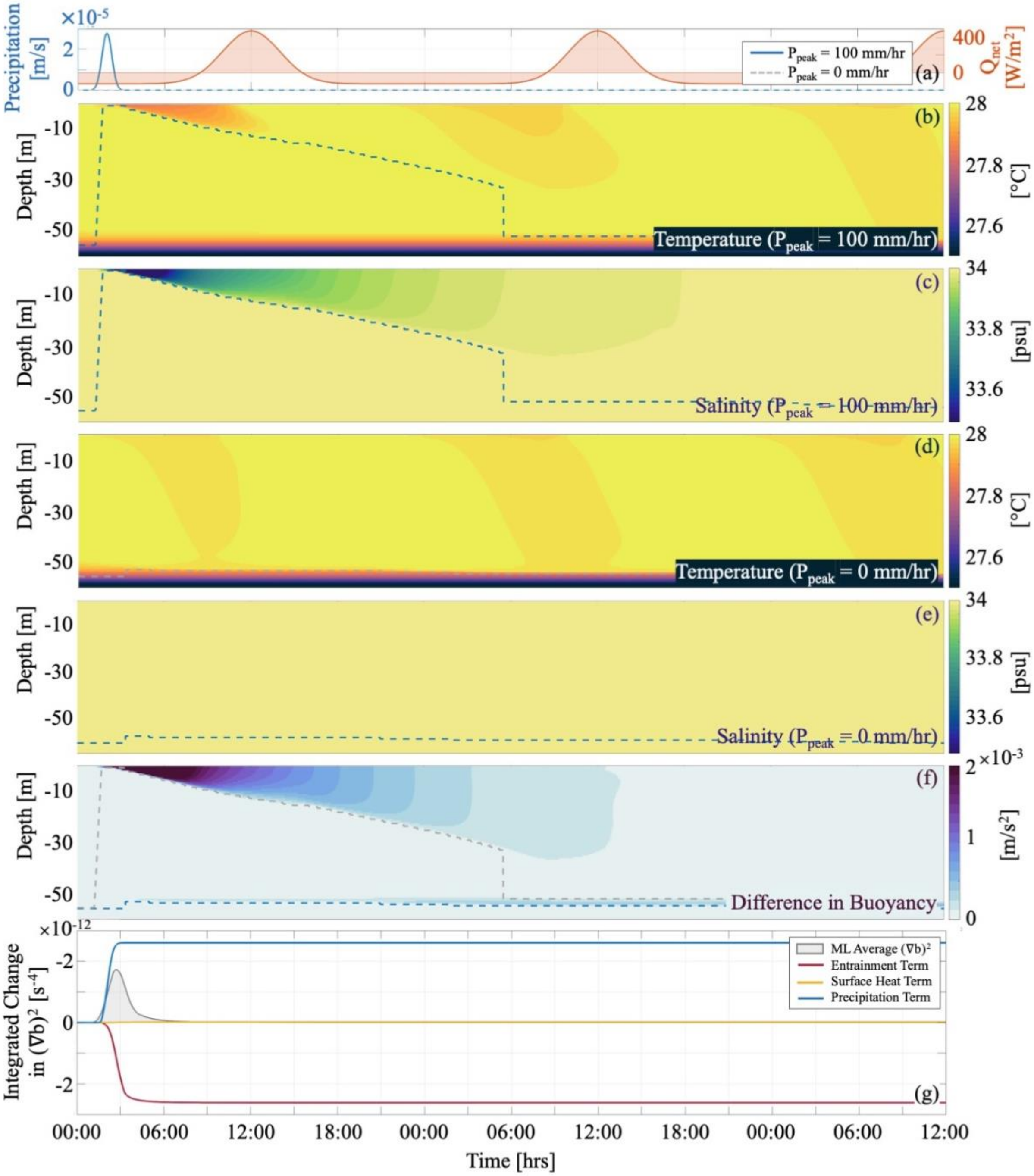

Figure 1-8. Case II scenario with simulation profiles. (a) Surface fluxes. (b) and (c) Temperature and salinity evolution for P_{peak} = 100 mm/hr. (d) and (e) Temperature and salinity evolution for P_{peak} = 0 mm/hr. (f) Difference in buoyancy inferred from the two-box system. (g) Time-integrated frontogenetic tendency with components. The gray and blue dashed lines in (b)-(f) indicate the mixed layer depths corresponding with each rain rate.

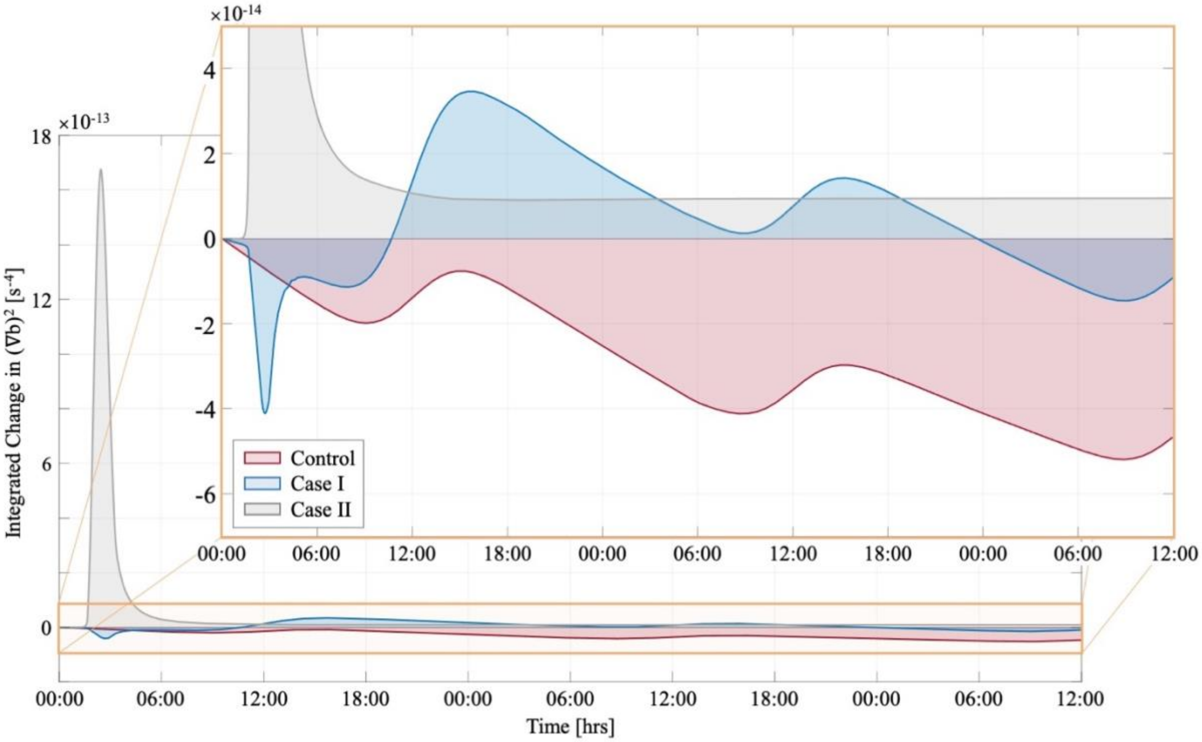

Figure 1-9. Cumulative integral of T_{dv} for the Control, Case I and Case II. The inset figure is magnified by an order of magnitude.

1.3.4 Considering Compensation

The above cases have demonstrated a range of different tendencies for strengthening or weakening lateral buoyancy gradients related to the interplay between precipitation, diurnal heating and entrainment, and sensitive to the initial lateral and vertical temperature and salinity gradients. That interplay leads to evolving lateral differences in both temperature and salinity, and hence the Turner angle, over hours and days. Here we will pause and further explore one component of that evolution, namely the *initial* impact on lateral gradients and Turner angle of different types of spatially varying rain. We return to the time evaluation of lateral gradients and discussion of the implications for submesoscale evolution on different time scales in Section 1.4.2 below.

For varying precipitation across an $O(10^{-7}\ \text{s}^{-2})$ surface lateral buoyancy gradient, the response is frontolytic when there is more rain on the dense side of the front (denoted as ‘frontolytic rain’). More precipitation on the light side of the front results in a frontogenetic response (denoted as ‘frontogenetic rain’). Figure 1-10 illustrates this in the form of tables along with Temperature-Salinity (T-S) diagrams and the resulting Turner angle. The larger the discrepancy in the rain rates between the light and dense sides, the larger the magnitude of the frontogenetic tendency, with the exception of a few cases with heavy rain on the dense side of the front. The frontogenetic tendency does not vary significantly across compensations.

The resulting Turner angles, however, behave differently across the compensations with similar patterns. For a partially compensated, salinity-dominated density gradient (Tu = -68º), frontolytic rain yields a weak compensating effect, with Turner angle approaching -90º, and frontogenetic rain results in a weak reinforcing effect. For both the non-compensated salinity- and temperature-dominated gradients (Tu = -23º and 23º), there is a strong compensating effect with frontolytic rain. The reinforcing response is stronger for the temperature-dominated gradient than for the salinity-dominated gradient with frontogenetic rain. For the compensated, temperature-dominated density gradient, there is a weak compensating effect with frontolytic rain, similar to the compensated salinity-dominated gradient, but the compensation approaches a Turner angle of 90º. Appendix D, in addition to Figure 1-10, provides visualizations of these transitions with a Turner angle schematic and in T-S space.

In T-S space, rain translates properties towards lower salinities and temperatures, shifting values significantly to the left and slightly towards the origin. Shifting only one property point alters the Turner angle, thus changing the compensation. Here, one can visualize how the shifting of properties can either align or orthogonalize mixing lines with isopycnals. Each compensation

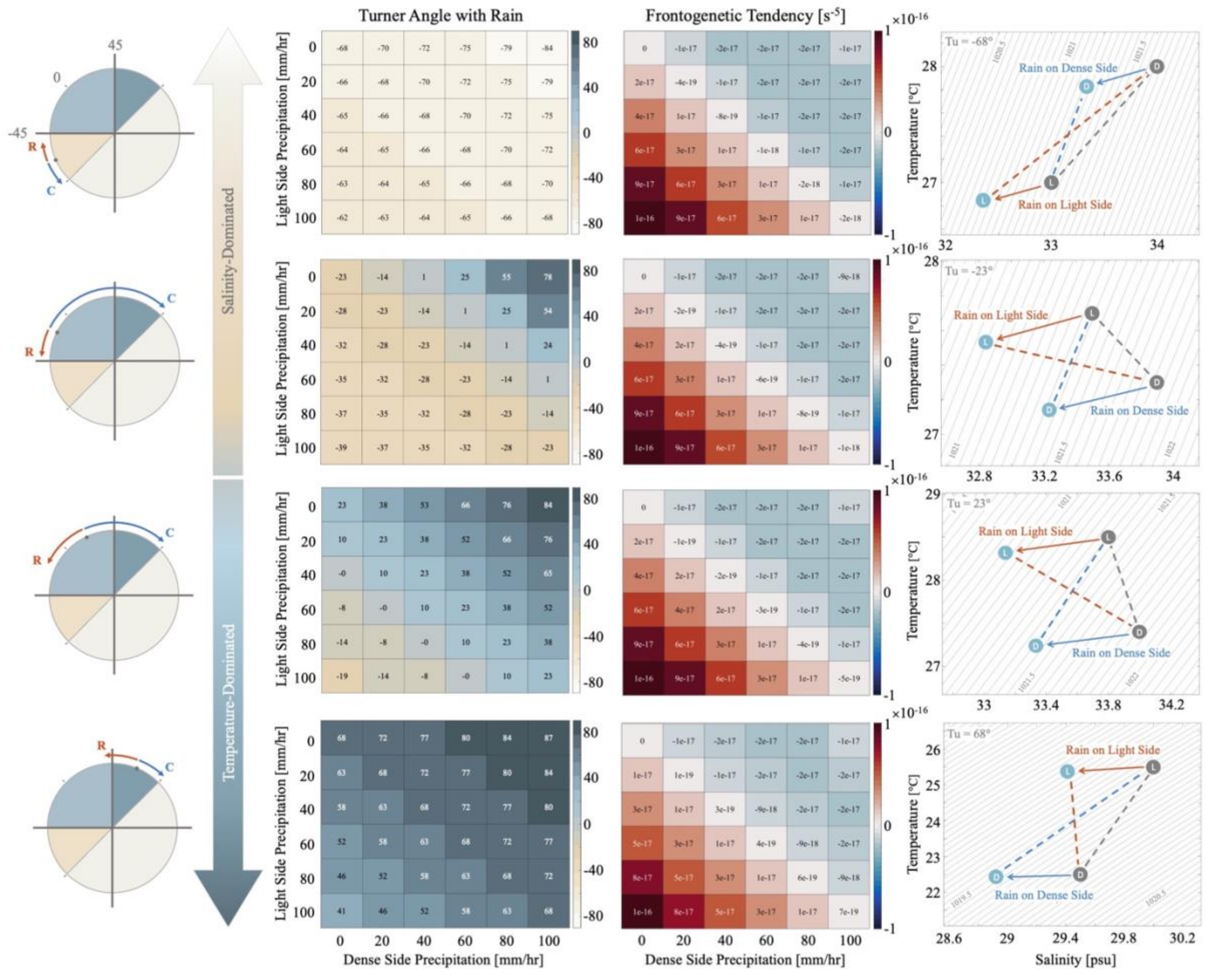

Figure 1-10. Values of T_{dv} [s^{-5}] and Turner angles (Appendix D) for various precipitation patterns and four types of compensations. The initial Turner angle increases for each successive row (-68° to 68°) and the unit circle schematics indicate where the initial Turner angle falls on the schematic (gray dots). The red and blue curved arrows indicate the direction rain forces the angle. The 'R' represents reinforcement and the 'C' represents compensation. The right-most column depicts T-S diagrams for each density gradient. The gray scatter indicates the initial surface conditions and the gray dashed line depicts the gradient in T-S space. The blue scatter indicates a new position in T-S space resulting from a peak precipitation rate of 100 mm/hr. The red and blue arrows and dashed lines on the T-S diagrams correspond to the red and blue curved arrows on the Turner angle schematics and indicate impacts of 'frontogenetic' and 'frontolytic rain', respectively.

type has similar behaviors to differential rain, as frontolytic outcomes align mixing lines with isopycnals, further compensating the density gradient. Adversely, frontogenetic outcomes make the mixing lines orthogonal to the isopycnals and reinforce the density gradient.

1.4 Discussion and Implications

1.4.1 Implications of 1-D Dynamics

This discussion will explore the frontogenetic implications of spatially-varying precipitation on surface lateral variability suggested by our observations and model results. But first, we will compare the 1-dimensional dynamics represented in the observations, simulations, and existing literature. Both the in-situ observations and simulations depicted the creation of a warm barrier layer in response to the rain with a temperature difference of 0.2ºC between the rain layer and barrier layer below. The fresh rainwater penetrated down to approximately 10 m depth within a few hours following the start of the rain event. The salinity budget for the observations estimates that the rain dropped the mixed layer salinity by approximately 0.5 psu by the time the rainwater reached 10 m depth. The simulations portray a similar reduction in mixed layer salinity at 10 m depth. The persistence of the shallow halocline at 10 m depth and subsequent warming of the mixed layer through entrainment in the observations appeared to occur hours after that of the simulations, likely due to the water column's pre-existing stratification and wind speed variability. Stronger stratification in the real ocean would require more energy to penetrate than that of the idealized stratification profiles used in the simulations (Iyer & Drushka, 2021; Chi et al., 2023). These rain layers may even reside at the surface for up to one day with low wind speeds (Drushka et al., 2016, 2019; Thompson et al., 2019; Chi et al., 2023). Observations from the WW show that the rain layer and shallow halocline was sustained for approximately 15 hours as wind speeds dropped to as low as 2 m/s. After, and beginning on July 18th, the winds increased (> 5 m/s), which would trap momentum and increase shear, disrupting the stability of the mixed layer base. Surface temperature and salinity rose while the warmer sub-layer became colder and fresher, suggesting that vertical exchange and entrainment may characterize the majority of the residual processes reflected in the salinity budget (Figure 1-3(c)). These entrainment processes are reflected in the model simulations but are simplified and gradual relative to observations. The complex temperature variability and resulting stratification from the precipitation found in the observations is also not represented in the simulations likely due to the model's idealized initial conditions and limitations. This may also point to the importance of advection and 3-dimensional dynamics that lead to these types of vertical structures.

The variability of surface forcing through wind and the diurnal cycle complicates the response of the mixed layer relative to the idealized conditions utilized in the simulations. Wind speeds vary significantly, especially during and after rain events, and average values of wind speed poorly represent nonlinear effects on the vertical structure of the boundary layer (Drushka et al., 2019). The variability illustrated in our observations have shown that winds can either sustain strong stratification if weak or disrupt these vertical boundaries if increased to a certain threshold, similar to past observations (Drushka et al., 2016, 2019; Thompson et al., 2019; Iyer & Drushka, 2021; Shackelford et al., 2022). If variable, the winds could lead to an oscillatory response in the stratification as the freshwater descends. Our observations also demonstrate that a rain layer may persist even with initially high wind speeds, as the wind speed was greater than 10 m/s throughout the peak of the rain event. Thompson et al. (2019) and Shackelford et al. (2022) suggested that this is rare. The diurnal cycle in the simulations was designed to have a net-zero heat flux so that the influence of precipitation and entrainment could be isolated. In reality, the magnitude of the net heat flux and the time of day at which it rains may have a notable impact on the mixed layer response and frontogenetic tendency. This was explored in Spiro Jaeger & Mahadevan (2018), with surface cooling leading to a compensation of salinity-driven fronts and a frontolytic response. While an important consideration, neglecting the impact of diurnal forcing is appropriate for these simulations as our findings and the findings of Thompson et al. (2019) demonstrate that the buoyancy forcing due to precipitation can be 1-2 orders of magnitude larger than the buoyancy forcing due to the diurnal cycle.

1.4.2 A Patchy Reality

In considering the impacts of precipitation on surface lateral variability, the model simulation yields insights into the dynamical circumstances of our observations. With the observations, there is a level of uncertainty surrounding the relative contribution of advection and precipitation to the observed lateral variability at the surface. The surface lateral buoyancy gradient in Transect A before the rain between the cold and salty filament and the relatively warmer and fresher waters before the rain was $3.3 \cdot 10^{-8}$ s^{-2} (Figure 1-4). Gradients were calculated by computing the difference between the lightest and densest points in surface buoyancy and dividing by the distance between them. Sampled within an hour of the end of the rain event, the surface lateral buoyancy gradient between the densest part of the filament and with the thin rain layer in Transect B is $2.6 \cdot 10^{-7}$ s^{-2} (Figure 1-2(b), Figure 1-4). The front is crossed again by the ship 18 hours later (McKie et al., 2024), and the surface waters reflect the signature of the barrier layer in Transect B with small-scale lateral and vertical structure beneath (not shown), similar to the WW observations after the rain is mixed down. Here, the surface lateral buoyancy gradient is $1.4 \cdot 10^{-7}$ s^{-2}. We are ignoring possible effects on the surface lateral gradient from other dynamics (mesoscale strain, wave forcing, etc.) and assuming the effects from vertical mixing dominate the frontogenetic tendency. The lateral buoyancy gradient in Transect B is higher relative to the lateral gradient before the rain, despite the temperature of the rain being colder and compensating. This is a frontogenetic response and is indicative of the Case II simulation. This suggests a spatially-varying precipitation pattern across the edge of the filament with precipitation mainly on the light side of the front. Equivalent signatures in thermohaline surface properties on the dense side of the front and within the filament in Transects A and B (before and after the rain event) strengthen this argument. What follows precipitation could be indicative of Case I and II simulations, with a frontolytic response caused by the mixing down of rainwater, yet it is gradual and dampened by entrainment from the warm barrier layer subsurface.

The insights from the observations and simulations highlight one example of a complicated reality. Often, if not perpetually, patchy rain impacts a patchy ocean, with variability in pre-existing stratification and compensation within lateral gradients. Shackelford et al. (2022) suggested that rain layers sharpen regional SST gradients through their cold anomalies. While this is true of our observations as well, it is difficult to label precipitation as purely frontogenetic because the frontogenetic tendency response varies temporally as the intricate vertical structure of the upper ocean influences the rain layer through entrainment and rain can conditionally compensate gradients. Additionally, the immediate impacts of surface forcing through wind and the diurnal cycle further complicate the response. These results demonstrate that the implications of rain deserve consideration when modeling the submesoscale.

Though the frontogenetic outcomes vary with varying rain and stratification, there are patterns that emerge. Precipitation shoals mixed layers, and if this effect is laterally homogeneous across a region it may temporarily reduce or enhance lateral buoyancy gradients, depending on lateral differences in mixed layer depth and underlying temperature and stratification profiles. If the precipitation is laterally inhomogeneous, the responses of the mixed layers to surface forcing and entrainment are likely to diverge, leading to larger responses in frontogenetic tendency. The compensation analysis (Figure 1-10) demonstrates that rain can have a compensating or reinforcing effect, depending on where it rains the most. Though the frontogenetic tendency does not change with respect to compensation, the resulting fronts are transformed into different compensations with enough rain. Because the signature of rain is cold and fresh, it seems to force fronts initially towards a Turner angle of -45° (salinity-dominated) when frontogenetic and towards a completely compensated state when frontolytic, regardless of the original compensation. Fronts that are driven towards compensation may encourage along-isopycnal subduction of water at the front, increasing temperature and/or salinity variance in the vertical and horizontal (Spiro Jaeger & Mahadevan, 2018). This may partially explain the thermohaline variance observed in the WW data in the days following the rain (Figure 1-3(d) and (e)). After the initial response, ML evolution and compensation is driven largely by the interplay between diurnal cycling and entrainment. The subsequent change in lateral gradients depends on the vertical gradients entrainment is mixing into; if the lateral gradient is primarily or entirely within the surface boundary layer, with laterally more homogeneous water below, then entrainment is frontolytic.

Satellite and in-situ observations demonstrate these effects at different length scales. The satellite observations in Figure 1-1 suggest that on larger scales, the precipitation is somewhat aligned with the dense, cold and salty filament. This would theoretically have a compensating effect on the filament and its surrounding waters at the mesoscale (*O*(100 km)). On the smaller scales of our in-situ observations (Figures 1-2, 1-4, and 1-5), the rain impacted the warm and fresh side of the front, thus reinforcing the front by strengthening the salinity gradient at smaller scales (*O*(10 km)). These patterns are transient, as the fate of surface properties are then determined by the evolution of surface forcing and entrainment.

Evaluating the significance of the frontogenetic tendency response due to rain is dependent on the time scales of interest. A rain event may be frontolytic initially but may have a sustaining effect on lateral buoyancy in response to surface forcing or entrainment (Case I) on the time scale of days. Conversely, Case II demonstrates that rain can be frontogenetic on the time scale of hours but has a negligible impact on the time scale of days. The impact on the development of subsequent submesoscale instabilities depends on the time scale of those instabilities. Processes such as symmetric instability can occur within hours, and such processes could respond to the development of lateral gradients immediately following a rain event (Haine & Marshall, 1998; Fox-Kemper et al., 2008; Dale et al., 2008; Taylor & Ferrari, 2011; Dauhajre & McWilliams, 2018; Johnson et al., 2020a, 2020b; Gula et al., 2022). Other processes such as mixed layer instability or frontogenetic secondary circulations are thought to develop on the time scale of an inertial period or longer (Boccaletti et al., 2007). At the latitude of the measurements and simulations presented here, freshwater anomalies tend to disperse over a day or two, comparable to the inertial period; thus, the slower instabilities may not have time to develop in response to rain events. However, at higher latitudes where the inertial period is much shorter, we may expect the full range of frontal instabilities to follow patchy precipitation.

1.4.3 Model Limitations

It is important to acknowledge that the two-box system is designed to simply understand how frontogenetic tendency is impacted through the vertical mixing of precipitation given various conditions. The experimental set up does not take into account other dynamics that may play an integral role in the evolution of a front. Explicitly, the simulations do not consider dynamical effects from the mesoscale, submesoscale, inertial, tidal or wave forcing. This also includes the frontogenetic or frontolytic effects associated with wind-driven gravity currents in rain layers (Wijesekera et al., 1999; Shcherbina et al., 2019; Laxague & Zappa, 2020; Moulin et al., 2021). These dynamics could alter the intensity of a front through straining or relaxing the lateral variability at the surface or erode the stratification subsurface, leading to a change in mixed layer heat and salt content, thus a change in surface properties. Though simplified, we hope the significance of these results motivate further study of these spatially-varying interactions between the atmosphere and ocean. It will be necessary to explore this topic with 3-D modeling to understand the relative contribution of the 1-D processes to frontogenetic tendency presented here to that of 2- and 3-D processes. Additionally, the idealized initial profiles for the two-box model reflect our observations, thus the results are limited to these particular mixed layer properties. There are countless combinations for initial profiles, and by expanding parameter space in considering surface compensation, we attempt to succinctly address other thermohaline variability in the surface mixed layer. It is possible that the results may change with the more variation in thermohaline properties, stratification, and mixed layer depths.

Conditions of the rain may also alter the results of this experiment. The idealized simulations were designed to represent a convective rain event, but we expect the frontogenetic tendency response to behave differently with stratiform rain. The ocean surface response to convective rain is much different compared to stratiform rain, because stratiform rain tends to have lower rain rates, longer durations, and a faster downward propagation of the rain layer (Iyer & Drushka, 2021). From our experimental results, we hypothesize that stratiform rain would prolong the frontogenetic tendency response in the case of spatially-varying rain rates, lengthening the time-scale that rain impacts the surface ocean. With spatially-varying stratification, the tendency response due to precipitation and entrainment may compete as vertical mixing could occur while the rain is ongoing. For both cases, the magnitude of the frontogenetic tendency response due to stratiform rain would be lower compared to convective rain. A potential bias of the simulations was the temperature of the rain, which is prescribed in the model as a result of the net heat flux. There have been modeling studies in which the parameterizations used in GOTM have either accurately characterized or overestimated the reduction in SST from precipitation (Pei et al., 2018; Shackelford et al., 2022). In our simulations, the rain reflected surface cooling and was colder than the surface temperature at similar values to our observations. There are also very rare cases in which the temperature of the rain is warmer than that of the surface (Gosnell et al., 1995; Byers et al., 1949). This uncommon scenario would change the resulting compensation of fronts.

1.4.4 Feedback Loops and Climate Change Impacts

There has been observational evidence that large scale (*O*(100 km)) fronts have influenced patterns of precipitation, with rain residing and enhanced on the warm edges of fronts (Minobe et al., 2008; Toy & Johnson, 2014). At smaller spatiotemporal scales, mechanisms for mesoscale or submesoscale impacts on atmospheric forcing and dynamics have been suggested. Precipitation can create a network of lateral temperature gradients and convergence and divergence patterns that have the ability to generate atmospheric convection (Shackelford et al., 2024). Downward momentum mixing and pressure adjustment are processes in which SST gradients modify wind convergences. This can result in changes to cloud cover and convective rainfall events (Hayes et al., 1989; Lindzen & Nigam, 1987; Minobe et al., 2008; Frenger et al., 2013; Meroni et al., 2018; Desbiolles et al., 2021; Strobach et al., 2022; Shackelford et al., 2024). Under the conditions in which precipitation generates a frontogenetic response in the surface ocean, these created or sustained lateral gradients may alter wind patterns as described. A positive feedback loop could occur with precipitation on the cold side of the front, which would enhance and sustain lateral temperature variability, increasing the probability of precipitation. This possibility is evident in the satellite observations for the cold filament from 86E to 88E (Figure 1-1). If on the warm side, the rain may temporarily reduce the SST gradient and delay the possibility of atmospheric convection until the surface warms through entrainment. The impact of these feedback loops on submesoscale dynamics further depends on compensation, and more specifically on variations in sea surface salinity. A positive feedback loop associated with a diffusive front could reinforce the front and enhance submesoscale dynamics. Alternatively, the same conditions on a salt-finger front would further compensate the front and suppress submesoscale dynamics.

The implications of this study under the context of a changing climate would suggest that the behavior and activity of the submesoscale may be altered. Because the Bay is becoming more susceptible to increased rainfall, this may mean that storms are becoming larger and stronger (Goswami et al., 2006; Kumar et al., 2011; Mishra et al., 2019; Goswami et al., 2021). This would impact the amount and spatial extent of precipitation influencing the surface of the basin. With more rain, the results of this experiment suggest that submesoscale activity could be impacted.

1.5 Conclusion

Precipitation in the Bay of Bengal can be influential in the interactions between the atmosphere and the sea through a variety of mechanisms. With the sharp, shallow halocline rain generates at the surface, SST can be influenced by inhibited mixing, the creation of barrier layers, and mixed layer sensitivity to diurnal forcing and entrainment. The observations presented here exhibited these dynamics and encouraged an investigation into how spatially-varying precipitation and pre-existing stratification impacts the submesoscale. The results of a 1-D model designed as part of a simplified two-box system revealed that the frontogenetic tendency response due to precipitation depends on the differential extent of the rain and the vertical structure of the boundary layer. Frontogenetic rain reinforces the compensation of a front towards a Turner angle of -45º and frontolytic rain has a compensating effect on the surface lateral variability. The initial frontogenetic tendency response of rain is decoupled from how it evolves, as differential entrainment through wind-driven mixing, varying mixed layer sensitivity, and diurnal forcing determines the tendency response hours after precipitation. Pre-existing stratification and its lateral variability determine the extent of this entrainment. In some cases, warm barrier layers generated by rain may have a frontogenetic effect, leading to the preservation of lateral gradients. The time-scales of the frontogenetic tendency response due to rain can be on the order of hours to days, so it may be influential to a broad range submesoscale dynamics in high latitude regions and the development of small-scale instabilities in low latitude regions. The submesoscale is proposed to be a critical factor in the improvement of regional models, though there are challenges regarding sufficient spatial resolution. This study suggests that the effect of precipitation on submesoscale features should also be considered as models improve, since it may enhance or suppress submesoscale activity. An important factor to consider given a changing climate, where rainfall in the Bay of Bengal is expected to increase.

1.6 Chapter Acknowledgements

Chapter 1, in full, has been submitted for publication of the material as it may appear in Journal of Geophysical Research: Oceans 2024. McKie, Taylor; Johnson, Leah; Schlosser, Tamara; MacKinnon, Jennifer; Lucas, Andrew, Wiley Online Library, 2024. The dissertation author was the primary investigator and author of this paper. This work was supported by Office of Naval Research Grants N00014-17-1-2511 and ONR N00014-17-1-2391. This material is also based upon work supported by the National Science Foundation Graduate Research Fellowship Program under Grant No. DGE-2038238. Any opinions, findings, and conclusions or recommendations expressed in this material are those of the author(s) and do not necessarily reflect the views of the National Science Foundation. The authors would like to express gratitude towards the science party and crew of the Summer 2019 ASIRI MISO-BoB Cruise onboard R/V Sally Ride as well as all technical staff with the Multiscale Ocean Dynamics Laboratory at Scripps Institution of Oceanography and Woods Hole Oceanographic Institution (WHOI) for their work and contributions in collecting and managing the in-situ data. We would especially like to thank Tom Farrar and the Upper Ocean Processes Group at WHOI for their contributions and efforts towards DBASIS.

Chapter 2 INVERSIONS AND INSTABILITIES

2.1 Introduction

The spatiotemporal variability of sea surface temperature (SST) in the Bay of Bengal (BoB) influences the atmospheric convection that drives the southwest monsoon (Vinayachandran et al., 2002; Vecchi & Harrison, 2002; Schott et al., 2009; Sengupta et al., 2016). The intense atmospheric convection over the Bay of Bengal is sustained by warm sea surface temperature (SST), which remains higher than 28°C throughout the summer monsoon season (Shenoi et al., 2002; Vinayachandran et al., 2013). However, the relative contribution of different physical oceanographic processes to the overall heat content and the spatiotemporal variability of SST in this region is still an open question.

The modification of the ocean boundary layer by freshwater input from precipitation and riverine discharge creates a rich and complex lateral and vertical structure in the BoB. This variability influences the basin's SST through the creation of fresh shallow mixed layers and their sensitivity to diurnal heating (Sengupta et al., 2006; Mahadevan et al., 2016). Sixty-percent of the freshwater input into the BoB originates from the Ganges-Brahmaputra-Meghna and Irrawaddy rivers, with input peaking during the summer and fall in the Northern BoB (Sengupta et al., 2006; Papa et al., 2010; Mahadevan et al., 2016; Sengupta et al., 2016). As the freshwater advects into the BoB and is altered through lateral and vertical mixing and atmospheric forcing, it influences the depth of the mixed layer, heat and momentum fluxes, surface velocity fields, and entrainment rates (Sengupta et al., 2006; Mahadevan et al., 2016). The composition of the BoB also includes relatively salty and dense waters derived from upwelling along the east coast of India driven by the southwesterly monsoon winds (Shetye et al., 1991). These upwelled waters are stirred into the mid-Bay and can contribute to the lateral and vertical structure of the BoB ocean boundary layer during the monsoon season.

In general, salinity sets the stratification in the upper 30-40 m of the BoB, with low salinity waters forming shallow mixed layers at the surface. This structure increases the sensitivity of the mixed layer, enabling a rapid response to surface heat fluxes, which directly impacts SST. These thin, shallow mixed layers are bounded by a sharp halocline, extending to approximately 10-30 meters depth, that can inhibit the exchange of heat and momentum with the layers below (Schott et al., 2009; Sengupta et al., 2016; Mahadevan et al., 2016). Barrier layers may lie between the halocline and the highly stratified isothermal layer. In the monsoon season, thick and strong barrier layers are widespread in the Northern BoB, mainly due to the advection of freshwater from the rivers at the surface and the deepening of the isothermal layer (Thadathil et al., 2002; Thadathil et al., 2007; de Boyer Montégut et al., 2007; George et al., 2019; Sherin et al., 2023). The presence of a barrier layer can influence the heat budget of the mixed layer by preventing cooler thermocline waters from interacting with the shallow mixed layer through vertical mixing and entrainment and by providing heat to the mixed layer, particularly in the case of temperature inversions. Barrier layers may also store heat, especially in the winter, that is eventually released to the surface during the passage of tropical storms. These mechanisms that allow for warmer mixed layers are known to aid cyclone intensification and to impact the intraseasonal oscillations of the monsoon (Yu & McPhaden, 2011; Balaguru et al., 2012; Lucas et al., 2016; Thadathil et al., 2016; Sengupta et al., 2016; George et al., 2019; Shroyer et al., 2021).

With salinity setting the stratification in the northern Bay of Bengal, colder water may overlie warmer water generating temperature inversions. Inversions may form within barrier layers creating thin filaments of stored heat subsurface that have implications for the overall thermodynamics of the boundary layer, as they may reduce surface cooling throughout the active phase of the monsoon (Shroyer et al., 2021; Sherin et al., 2023). Most studies have focused on the formation of temperature inversions through one-dimensional processes, while advection has been found to be an intermittent process (Thadathil et al., 2002; Sengupta et al., 2016; Thadathil et al., 2016; Ramachandran & Tandon, 2020). More recently, observations and models have demonstrated that strong temperature inversions can develop at the edges of submesoscale fronts and filaments (Adams et al., 2019; Shroyer et al., 2020; Ramachandran & Tandon, 2020). These inversions and the associated vertical thermohaline variability within barrier layers may be indicative of shear-driven, turbulent mixing (Shroyer et al., 2021). These findings motivate an investigation of the role of small-scale, three-dimensional processes in the formation of barrier layers and temperature inversions.

The submesoscale can be described by the scale at which relative vorticity of a flow balances the planetary vorticity, in other words, dynamics at which the Rossby number is $O(1)$. Submesoscale dynamics are frequently at play near sharp fronts and filaments (Thomas et al., 2008). In such environments, a variety of instabilities are possible (Taylor & Thompson, 2023). These submesoscale instabilities and associated circulation and mixing may impact the heat content of both the barrier and shallow mixed layer. The BoB in particular has a very energetic mesoscale with a heightened eddy kinetic energy relative to other regions, thus has an elevated frontogenesis potential (Jaeger et al., 2020). Additionally, the contrast between the various water masses introduced to the Bay, which span a broad range of salinities, makes for extremely sharp lateral variability. Both of these factors allow for the Bay to have a very active submesoscale field. The strength and diverse signatures of these features lead to complex, lateral patterns of vertical stratification through the stirring and interleaving of small-scale filaments, enhanced vertical exchanges, and entrainment through and within mixed layers, barrier layers, and the thermocline (Lucas et al., 2016; MacKinnon et al., 2016; Mahadevan et al., 2016; Sarkar et al., 2016; Ramachandran et al., 2018).

Ultimately, the 3-dimensional dynamics at these small scales can have major implications for the overall thermodynamics of the boundary layer and associated SST. While advection may be important in setting the temperature of the mixed layer at times during the monsoon, surface heat flux and vertical processes govern the mixed layer heat budget (Sherin et al., 2023). Regional coupled ocean-atmosphere models, which typically exhibit bias in SST, largely depend on one-dimensional processes to set mixed layer properties (Chowdary et al., 2016). This bias may signify that the submesoscale is a missing piece in accurately characterizing the heat content of the mixed layer, and thus the interactions between the atmosphere and BoB. These models have predicted surface temperatures that are colder than that of observations due to an underestimation of the strength of salinity stratification, an overestimation of the extent of mixing and mixed layer depth, and a mis-characterization of the lateral variability in mixed layer depths (Benshila et al., 2014; Chowdary et al., 2016; Lucas et al., 2016; MacKinnon et al., 2016; Sengupta et al., 2016). The difficulty in parameterizing submesoscale dynamics and the impact of these small-scale features in coupled ocean-atmosphere models arises from the scarcity of high-resolution sampling to inform these models (MacKinnon et al., 2016). The high-resolution observations collected during a recent expedition to the Bay of Bengal provide an opportunity to improve our understanding of these submesoscale dynamics and their impact on the ocean boundary layer of the BoB.

Here we present observations of the BoB gathered during a intensive field study during the 2019 southwest monsoon season (Shroyer et al., 2021). These observations show processes occurring at the submesoscale facilitating the creation of barrier layers, formation of temperature inversions, and the storage of heat below the surface. The paper is organized as follows: The research initiative and instrumentation are described in Section 2.2. The hydrographic survey and observations are presented in Section 2.3. Section 2.4 details a stability analysis, including calculations for geostrophy, frontogenesis, potential vorticity, and instabilities. Section 2.5 discusses the significance of temperature variability, the implications of the results for vertical exchange, and how the observations compare to modeling results. We provide conclusions with Section 2.6.

2.2 Instrumentation

The field observations presented here were collected as part of the Office of Naval Research's Monsoon Intraseasonal Oscillations in the Bay of Bengal (MISO-BoB) Departmental Research Initiative. This multi-year project aimed to improve the prediction of the monsoon in the Northern Indian Ocean by characterizing the heat content and stratification of the oceanic boundary layer at multiple scales (Shroyer et al., 2021). The data utilized in this analysis is a subset of a survey that took place from July 6th to August 4th, 2019, onboard the R/V *Sally Ride*. One of the objectives of this particular cruise was to examine the evolution of near surface lateral variability and stratification at both the meso- and submesoscale and characterize the structure of the mixed layer depth.

The complete survey included multiple ship tracks and instrument deployments within a region of mesoscale confluence between the latitudes of 15ºN and 18ºN and longitudes 87ºE and

90ºE. The data analyzed in this work are derived from the FastCTD profiling system, the shipboard meteorological acquisition (MET) and the shipboard acoustic Doppler current profiling (ADCP) systems. The FastCTD is a profiling instrument equipped with temperature, conductivity, and pressure sensors that can profile either while towed at speeds of several knots, or while the ship remains stationary (Shroyer et al., 2021; Pinkel et al., 2023). For this survey, it was rapidly profiled to about 200 meters depth while the ship maintained a speed of about 3 knots, with a 2-minute duration for each cast. The horizontal spacing between drops at the surface for each profile was approximately 200 meters, and the vertical resolution was approximately 1 meter, allowing for the spatial resolution necessary to observe submesoscale features.

The velocity profiles analyzed in conjunction with the FastCTD profiles were obtained from a 300kHz ADCP installed on the ship. The ADCP data was binned to have a resolution of about 2 minutes from approximately 10 m to 100m depths, with 2-meter vertical sampling.

2.3 Hydrographic Survey and Observations

To understand the broader, regional context of the basin in mid-July, Figure 2-1 shows SST from satellite reconstruction and the geostrophic velocity field (DMI COI, 2007; Dohan, 2021). During this time, a cold, salty and relatively dense filament was drawn offshore from the coast by mesoscale circulation. Gradients between the filament and warmer and fresher waters offshore created relatively sharp fronts on both sides of the filament. Here we will focus on the strong lateral density gradient on the eastern edge of the filament, hereafter referred to as the

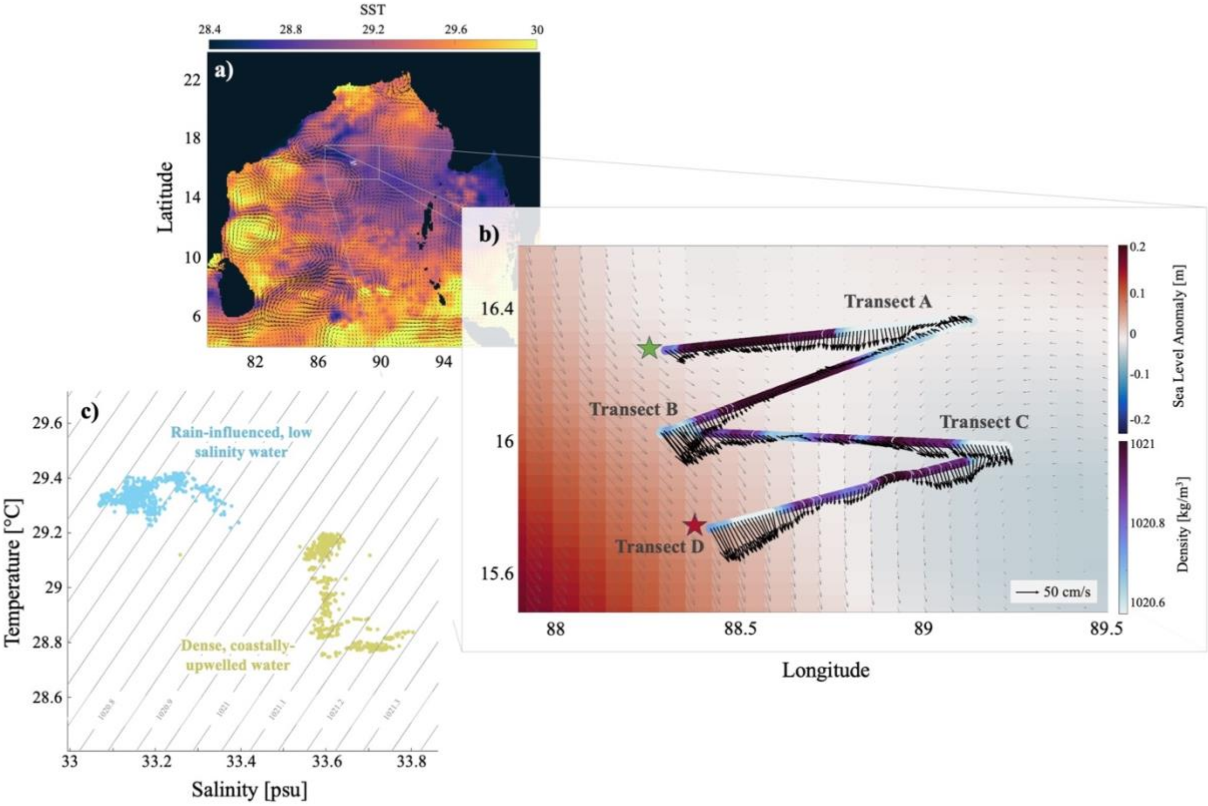

Figure 2-1. (a) Satellite SST reconstruction (DMI COI, 2007) of the Bay of Bengal on July 18, 2019 with geostrophic currents (Dohan, 2021). The inset figure (b) depicts near-surface density (derived from FastCTD data) of the 4 transects crossing the filament overlaid on sea level anomaly data. The thick black arrows indicate the depth-averaged currents in the boundary layer (10 - 40 m) from the shipboard ADCP and the thin gray arrows indicate the geostrophic surface velocity field derived from the sea level anomaly. The green and red stars indicate the start and end times of this dataset from midnight July 18th (UTC) to 4:00 AM July 20th (UTC). The bottom-left panel (c) depicts a T-S diagram of the top 5 meters of Transect A.

front. The fresher, ambient water to the east of the front may have also been freshened by precipitation from a convective rain event occurring the morning of July 17th. Figure 2-1 includes a T-S diagram from the upper 5 meters of Transect A, showing two distinct water masses. Upper ocean velocity along the transects shows some features consistent with the altimetry-based currents, such as strong south-eastward flow on the west side of the transects, westward becoming southward flow on the east side of the transects, and weaker flow in the convergence zone in between. The measured velocities also show variability at smaller scales (≈ 10 km), which will be discussed further below.

This paper will focus on four transects of the survey in which various regions of the front along the filament edge exhibited both restratification (slumping) and steepening. The four transects were observed within an inertial period (43 hours). As illustrated in Figure 2-1, the survey was designed to span a region of confluence between two mesoscale eddies and advance in the direction of the mesoscale flow as a function of time, spanning approximately 50 km in the along-front direction. The angle of the along-front direction was determined by estimating the lateral angle between a line connecting the maximum surface density gradient from each of the four transects and east. The calculated across-front direction was 45° rotated north of east, with the along-front direction perpendicular to that. The ship crossed the strongest lateral surface density gradient on the eastern side of the pattern, where the frontal region was observed twice (Transect A and Transect B) in less than one-half of an inertial period and within 10 km separation, with the first transect beginning on July 18th around 5:30 AM local time (midnight UTC 7/18) and the second transect ending around 3:30 AM on July 19th (10 PM UTC 7/18). The front was reached again on 7:30 AM on July 19th (2:00 AM UTC) (Transect C) and around 9AM on July 20th (4:00 AM UTC) (Transect D). In the first pair of crossings, the front appeared to be undergoing restratification and had a vertical angle of 0.05° from the horizontal. In the second set of crossings, the front appeared to be much steeper, with an angle of 8° from the horizontal. We henceforth describe transects A/B and C/D separately.

2.3.1 Restratifying Front

The interior of the restratifying regions of the front from Transects A and B are depicted in Figure 2-2. The filament was observed to at least 40 m depth. The density gradient across the front was primarily salinity-driven, with near-surface salinity values varying from 33.8 to 33.2 psu and temperatures varying from 28.6ºC to 29.4ºC. These values are roughly consistent with previously reported values for salinity-driven submesoscale fronts in the Bay (Ssengupta et al., 2016). The maximum surface lateral buoyancy gradients for both transects are order $O(10^{-7}\ s^{-2})$, calculated from FastCTD profiles separated by approximately 200 m in the along-track direction.

These two sections exhibited complex lateral and vertical variability in both temperature and salinity. The dense side of the front displayed temperature variability on scales smaller than 10 km. This lateral variability may have been the result of stirring and straining by mesoscale eddies, non-uniform surface forcing and entrainment, or ageostrophic baroclinic instabilities (Ferrari & Rudnick, 2000; Hosegood et al., 2006; Boccaletti et al., 2007; Gula et al., 2014, Shcherbina et al., 2015; Spiro Jaeger & Mahadevan, 2018). The coastal filament was bounded by a sloping region of high stratification extending from the surface to the top of the thermocline over a lateral distance 30 km. We calculated the mixed layer depth (MLD) and isothermal layer depth (ILD) following Kara et al., (2000); the difference between them defines the bounds of the barrier layer (black and red dotted lines in Figure 2-2). The ILD was based on a temperature difference of 0.8ºC from SST and the MLD was based on the density equivalent of that value (Kara et al., 2000; Thangaprakash et al., 2016; George et al., 2019). The ILD was shallower on the dense side of the front but overall varied between 25 and 40 meters depth in both transects (Thadathil et al., 2007). The MLD was nearly identical to the ILD on the dense side of the front, but shoaled to 10-15 meters depth at the frontal axis due to the increasing importance of salinity stratification on the fresher side of the front. The MLD was much shallower on the fresher side of the front. These conditions created a barrier layer on the light side of the front with a thickness varying between 10 and 30 meters.

Figure 2-2. Thermohaline variability, surface forcing, and velocity of the restratifying regions (Transects A and B), Continued. From top to bottom, the panels represent surface forcing, temperature, salinity, density, across-front velocity, and along-front velocity. The gray bar in the surface forcing panel indicates nighttime. The white lines indicate isopycnals at 0.08 kg/m^3 intervals. The black dashed line indicates the mixed layer depth (MLD). The red dashed line indicates the isothermal layer depth (ILD). The yellow dashed line on the density section indicates the approximate angle of the front to the horizontal.

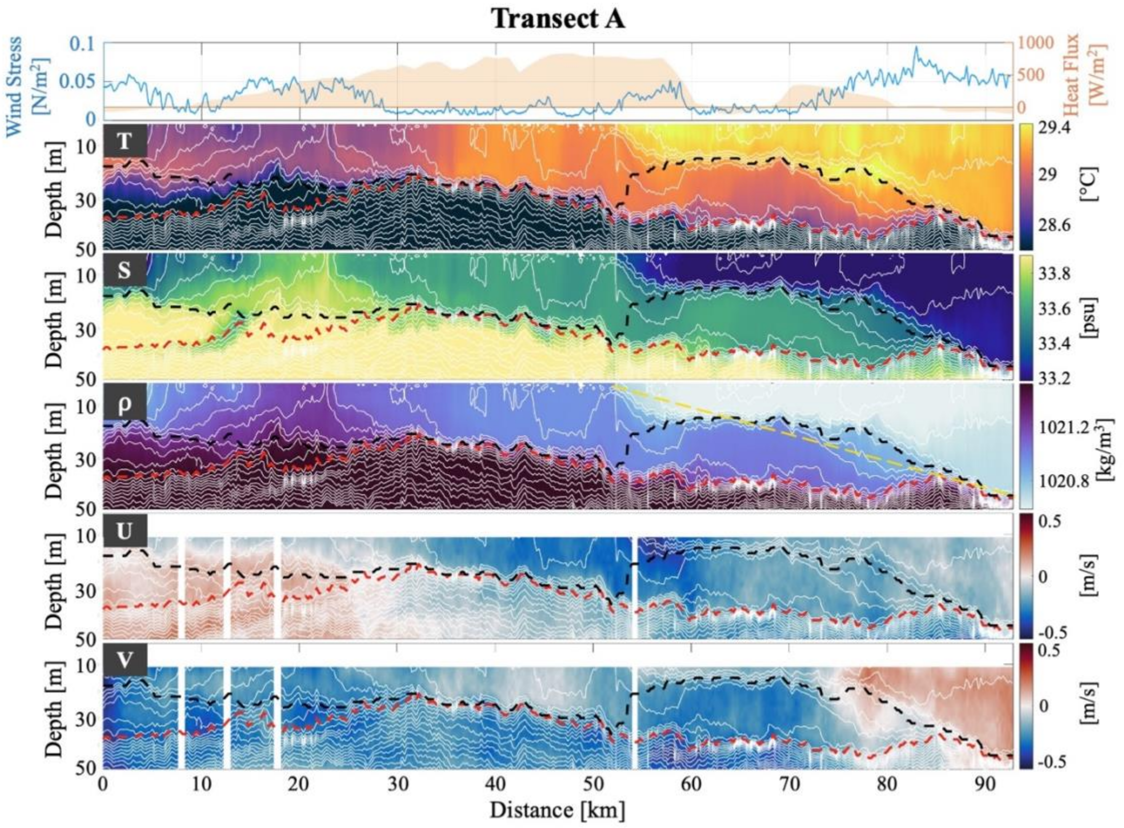
Transect A
Wind Stress [N/m²]
0.1
0.05
0
Heat Flux [W/m²]
1000
500
0
T
S
ρ
U
V
Depth [m]
10
30
50
29.4
29
28.6
[°C]
33.8
33.6
33.4
33.2
[psu]
1021.2
1020.8
[kg/m³]
0.5
0
-0.5
[m/s]
0
10
20
30
40
50
60
70
80
90
Distance [km]

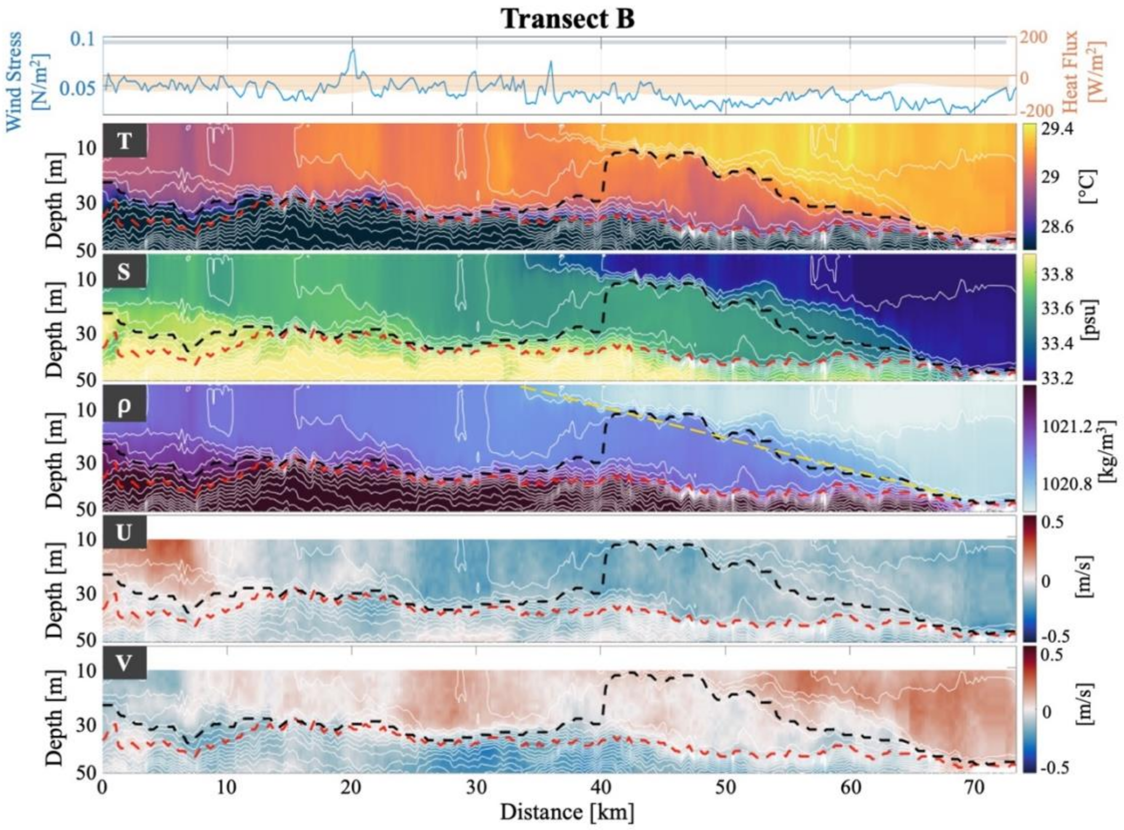
Transect B
Wind Stress [N/m²]
0.1
0.05
Heat Flux [W/m²]
200
0
-200
T
S
ρ
U
V
Depth [m]
10
30
50
29.4
29
28.6
[°C]
33.8
33.6
33.4
33.2
[psu]
1021.2
1020.8
[kg/m³]
0.5
0
-0.5
[m/s]
0
10
20
30
40
50
60
70
Distance [km]

The observed velocity gradients correlate with both the observed gradually sloping stratification and the observed sharp lateral fronts. For Transect A, there was a surface southwestward flow on the dense side of the front. Within the shallow mixed layer, the flow direction was westward while in the barrier layer beneath, the flow was southward, creating strong vertical shear along the halocline. There was relatively strong lateral shear and cross-frontal convergence $\left(\frac{du}{dx}/f \approx 1\right)$ near the surface at the center of the front, with the across-front velocity increasing to approximately 0.5 m/s. To estimate this convergence, horizontal gradients in across-front velocity were calculated over a distance of 1 km.

Near the frontal axis and in the deep mixed layer of Transect B, the flow was southwestward. The flow within the barrier layer was also southwestward, and the shallow mixed layer above it flowed westward. This created vertical shear along the shallow halocline. Beneath the ILD throughout the transect, there was a southeastward flow, which also created vertical shear along the boundary of this layer. Similar to the previous transect, there was relatively strong lateral variability in the along- and across-front velocities at the axis, creating a convergence zone with a magnitude of $\frac{du}{dx}/f \approx 1$.

The stratification varied significantly throughout these transects, as shown in Figure 2-3. The stratification within the barrier layer was at least one order of magnitude lower than that of the highly stratified regions bounding the shallow mixed layer and below the isothermal layer depth. The barrier layer also had the most complex stratification structure, with coherent streaks of stratification stretching laterally and vertically. The deep mixed layer adjacent to the layer was the least stratified and had stratification at least 1 to 2 orders of magnitude lower than that of the barrier layer.

Figure 2-3. Potential vorticity fluxes due to diabatic (J_D) and frictional forcing (J_F), stratification, vertical temperature gradient, and Richardson Number for the restratifying regions (Transects A and B), Continued. The gray bar in the potential vorticity (PV) flux panel indicates nighttime. The white lines indicate isopycnals at 0.08 kg/m^3 intervals. The cyan dashed line indicates the mixed layer depth (MLD). The red dashed line indicates the isothermal layer depth (ILD).

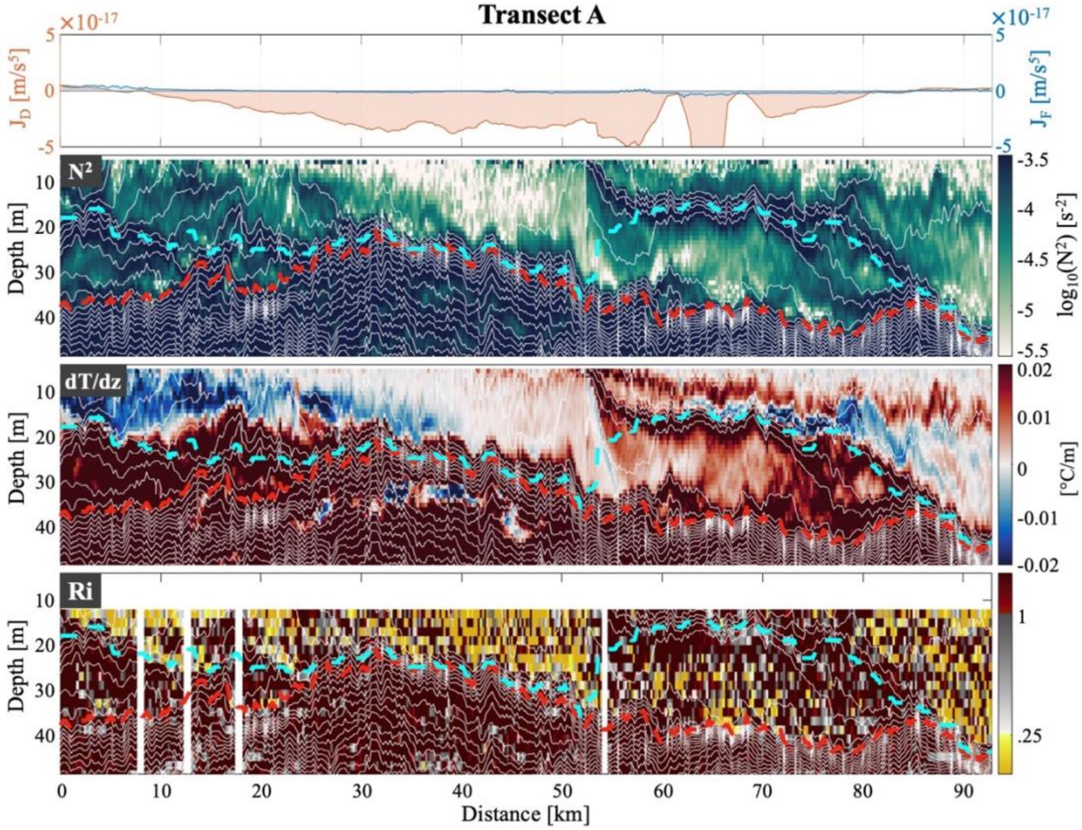
Transect A
×10⁻¹⁷
J_D [m/s⁵]
5
0
-5
×10⁻¹⁷
J_F [m/s⁵]
5
0
-5
N²
Depth [m]
10
20
30
40
log₁₀(N²) [s⁻²]
-3.5
-4
-4.5
-5
-5.5
dT/dz
[°C/m]
0.02
0.01
0
-0.01
-0.02
Ri
1
.25
0
10
20
30
40
50
60
70
80
90
Distance [km]

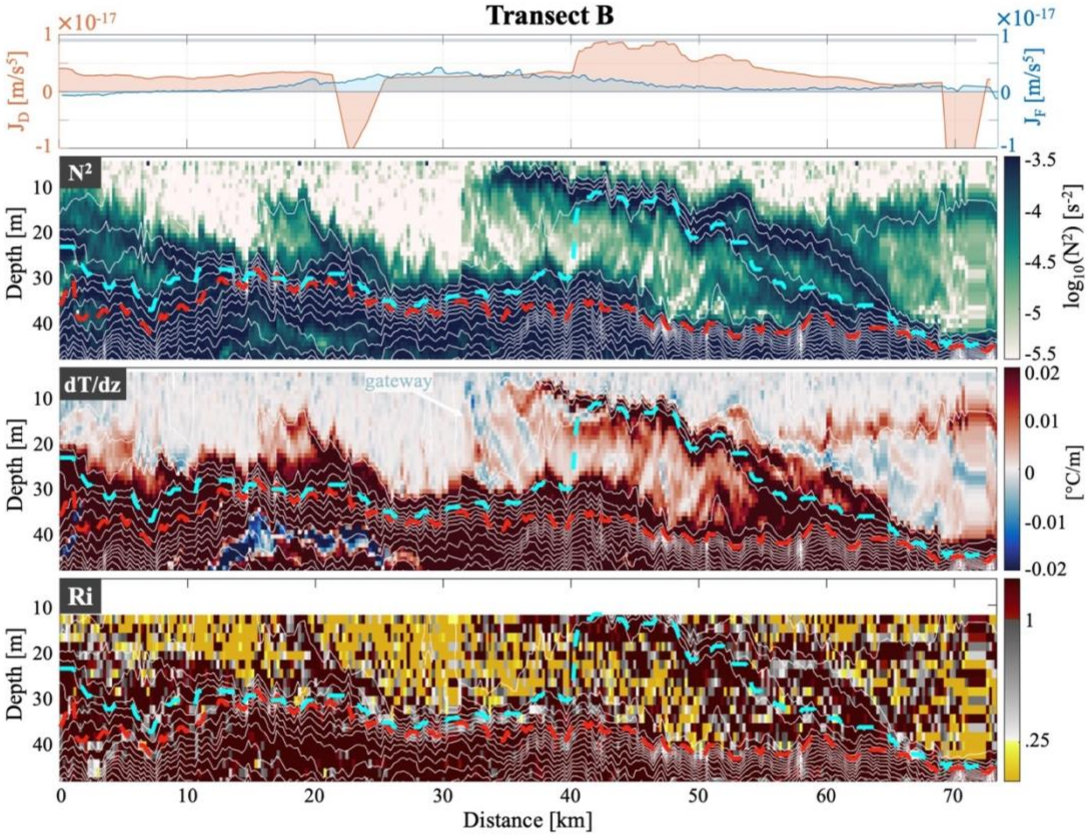
Transect B
×10⁻¹⁷
J_D [m/s⁵]
1
0
-1
×10⁻¹⁷
J_F [m/s⁵]
1
0
-1
N²
Depth [m]
10
20
30
40
log₁₀(N²) [s⁻²]
-3.5
-4
-4.5
-5
-5.5
dT/dz
gateway
[°C/m]
0.02
0.01
0
-0.01
-0.02
Ri
1
.25
0
10
20
30
40
50
60
70
Distance [km]

Temperature inversions were found adjacent to the barrier layer (Transect A at x = 52 km; Transect B at x = 33 km) when the vertical derivative of temperature is plotted as shown in Figure 2-3. Because these temperature inversions were slanted laterally from the less stratified deep mixed layer into the slightly more stratified barrier layer, we use the term “gateway” to describe this transitional region. The gateway also coincided with the maximum lateral buoyancy gradient at the surface, and it had a vertical structure that extended down to the ILD. The thin and slanted temperature inversions stirring into the barrier layer were confined by semi-coherent layers of stratification and were reminiscent of spice layers found in past observations (Jaeger et al., 2020). Some inversions in both transects also appeared to cross isopycnals. The inversions had lateral scales of 1-5 km, vertical scales of 5-30 meters, and the vertical temperature gradient reached a maximum of 0.01ºC/m.

These two transects presented an opportunity to observe the front during the day and at night. For Transect A, the atmosphere was primarily warming the surface ocean for hours prior to and during the crossing of the frontal axis (top panels for each transect in Figure 2-2). In contrast, the ocean was cooling throughout the entirety of Transect B. Between the first and second front crossings, there was a relatively consistent period of cooling with approximately 100 W/m^2) extracted from the ocean to the atmosphere based on the shipboard estimates of bulk ocean-atmosphere fluxes. The near-surface stratification observed at night generally appeared to be an order of magnitude less stratified compared to that of the day, reflecting what may be expected from convection and restratification from diurnal heating.

The winds during these transects blew moderately from the south and southwest direction. There was little spatial variability in these wind patterns at a regional scale (not shown). The average wind speed (stress) for Transect A was 4.8 m/s (0.027 N/m^2) and the average wind speed (stress) for Transect B was 6.0 m/s (0.043 N/m^2). Ekman transport would be to the east and southeast which creates the possibility for the dense filament to be pushed over the lighter waters.

2.3.2 A Steepening Front

Although the surface properties did not change significantly in Transects C and D, the front became considerably steeper (Figure 2-4). The front remained salinity-controlled with surface salinity values ranging from 33.6 psu to 33.1 psu and surface temperature values ranging from 28.9ºC to 29.5ºC. The surface lateral buoyancy gradient, however, was significantly larger ($O(10^{-6}\ s^{-2})$) compared to the previous two transects. There was small-scale temperature variability at the surface, mainly on the light side of the front and varying on the scale of 0.1ºC/km. This lateral variability presented as a vertically plummeting mass of warm water in Transect C (x = 88 km) and Transect D (x = 80 km). The warmest end of this descending plume can be found at 40 m depth in Transect C and 45 m depth in Transect D; there were four hours between those measurements. The MLD extended down to the ILD surrounding the front. Beneath the filament and moving right towards the frontal axis, the MLD and ILD gently sloped from 40 to 60 meters depth. On the fresh side of the front, the bounds of each layer increased to approximately 50 meters depth. There was more lateral salinity variability near the front with some vertical variability within the filament, but the temperature variability was much more complex. Because the MLD and ILD were nearly identical in this region, the barrier layer had completely vanished.

In Transect C, there was a strong southeastward jet with vertical shear within the filament (centered at x = 76 km). The light, fresh side of the front was flowing southwestward, creating a

Figure 2-4. Thermohaline variability, surface forcing, and velocity of the steepening regions (Transects C and D), Continued. From top to bottom, the panels represent surface forcing, temperature, salinity, density, across-front velocity, and along-front velocity. The gray bars in the surface forcing panels indicate nighttime. The white lines indicate isopycnals at 0.08 kg/m^3 intervals. The black dashed line indicates the mixed layer depth (MLD). The red dashed line indicates the isothermal layer depth (ILD). The yellow dashed line on the density section indicates the approximate angle of the front to the horizontal.

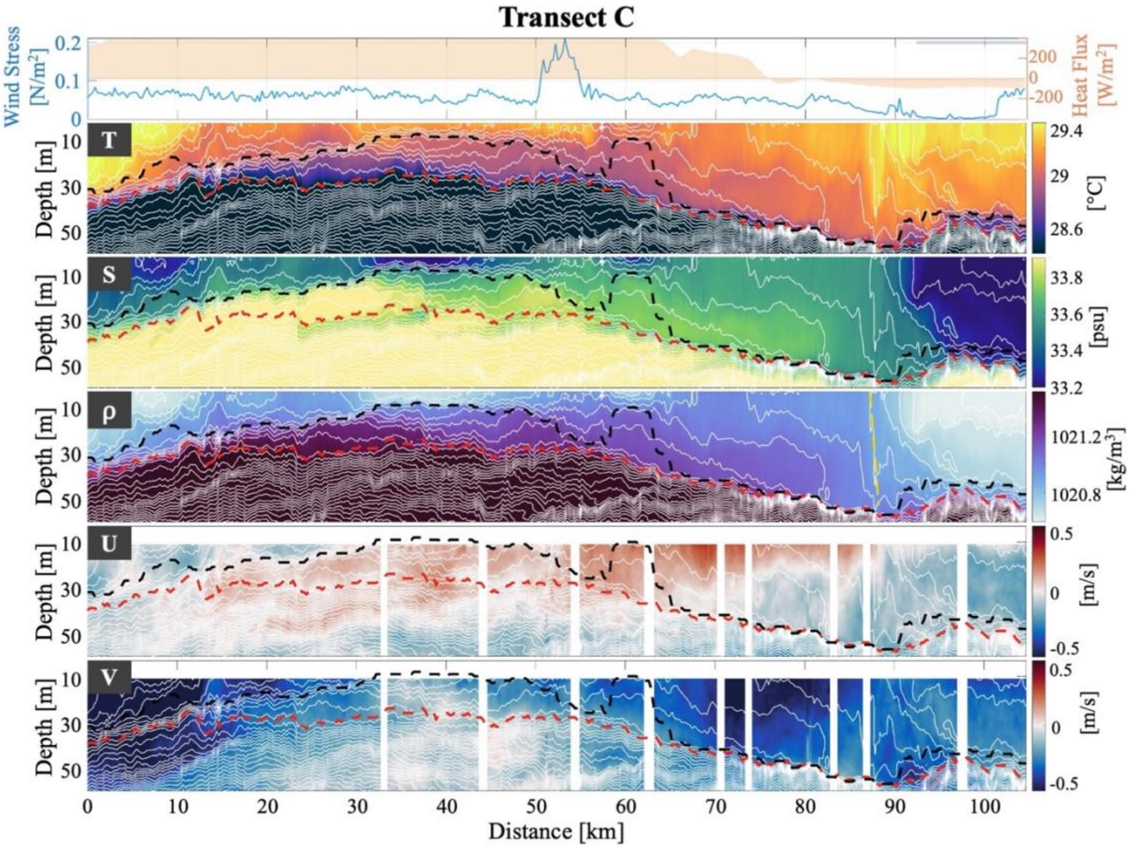
Transect C

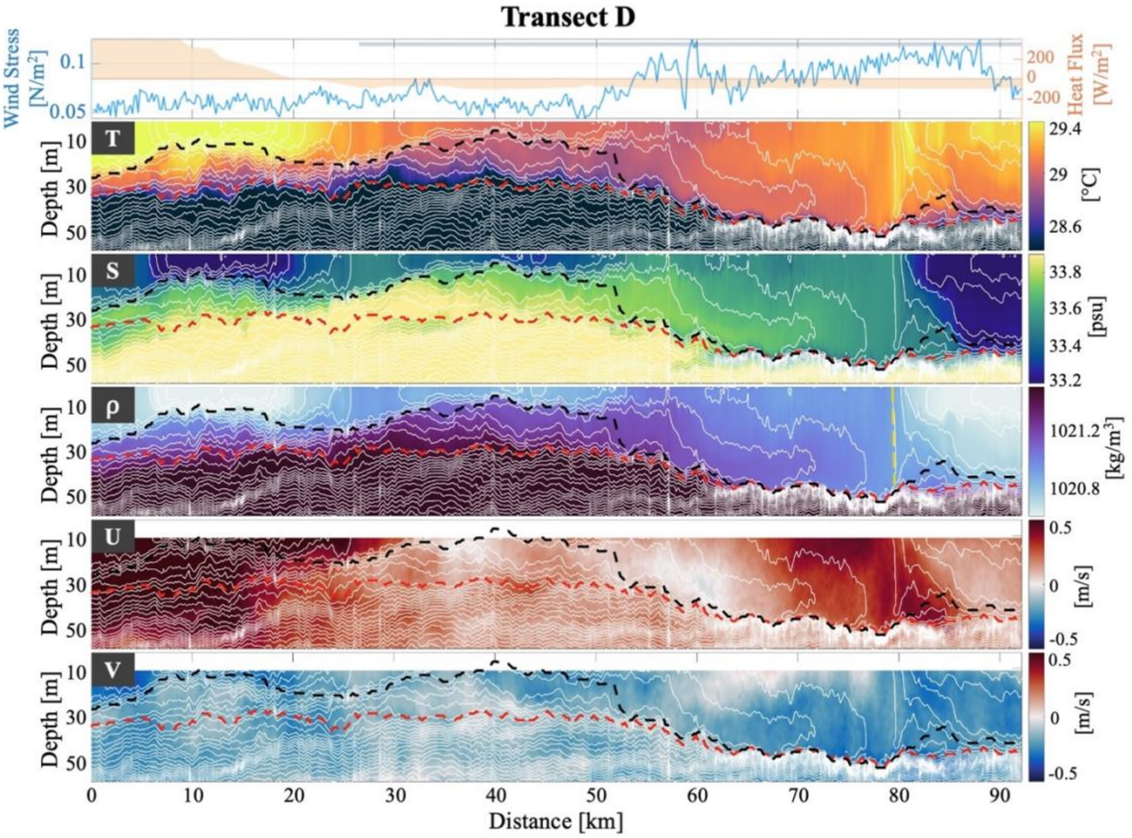
Transect D

cross-frontal convergence with a magnitude of $\frac{du}{dx}/f \approx 1$ at the axis of the front. In Transect D, the jet shifted more eastward and moved towards the axis of the front. There was strong lateral and vertical shear within the filament and at the frontal axis and it was approximately double the magnitude compared to Transects A and B. The convergence magnitudes of Transects C and D was double that of Transects A and B.

Temperature inversions were also observed in these transects as shown in Figure 2-5, however, they were no longer organized and coherent structures stretching from the axis of the front into the barrier layer. In contrast, they had a more complex shape and were located from 5 to 10 km away from the frontal axis (Transect C: x = 70, 90 km; Transect D: x = 60, 80 km). The aspect ratio of the inversions was larger than those found in the restratifying front, with both lateral scales nearing 10 km and vertical scales up to *O*(10 m). Despite these differences, the magnitude of the gradients of the temperature inversions here were similar to that of those near the restratifying front. The stratification in these regions was also highly complex and intricate with values ranging two orders of magnitude. A weakly stratified column developed at the frontal axis in Transect C and was surrounded by highly stratified regions on either side of the front. In Transect D, the weakly stratified column at the front became more uniform and had a width of 3-4 km while extending down to 40 meters depth. Weak stratification trailed from the column underneath the filament and along the MLD for approximately 25 km.

During the crossing of the front in both of these transects, cooling with a magnitude of approximately 100 W/m^2 was observed. The winds were stronger relative to Transects A and B, with the Transect C having an average wind speed (stress) of 6.5 m/s (0.050 N/m^2) and Transect D having an average wind speed (stress) of 7.9 m/s (0.074 N/m^2). These winds were also mainly from the south and southwest, thus the Ekman transport would be to the east and southeast,

Figure 2-5. Potential vorticity fluxes due to diabatic (J_D) and frictional forcing (J_F), stratification, vertical temperature gradient, and Richardson Number for the steepening regions (Transects C and D), Continued. The gray bars in the PV flux panels indicate nighttime. The white lines indicate isopycnals at 0.08 kg/m^3 intervals. The cyan dashed line indicates the mixed layer depth (MLD). The red dashed line indicates the isothermal layer depth (ILD).

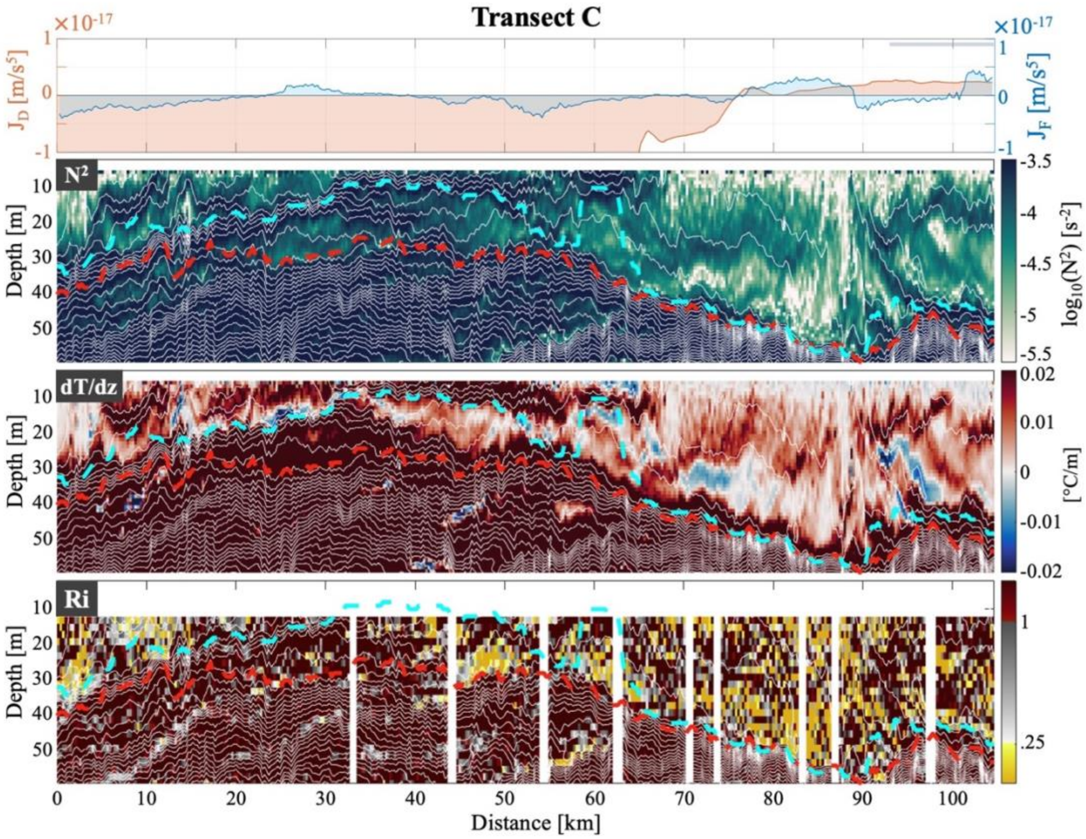
Transect C

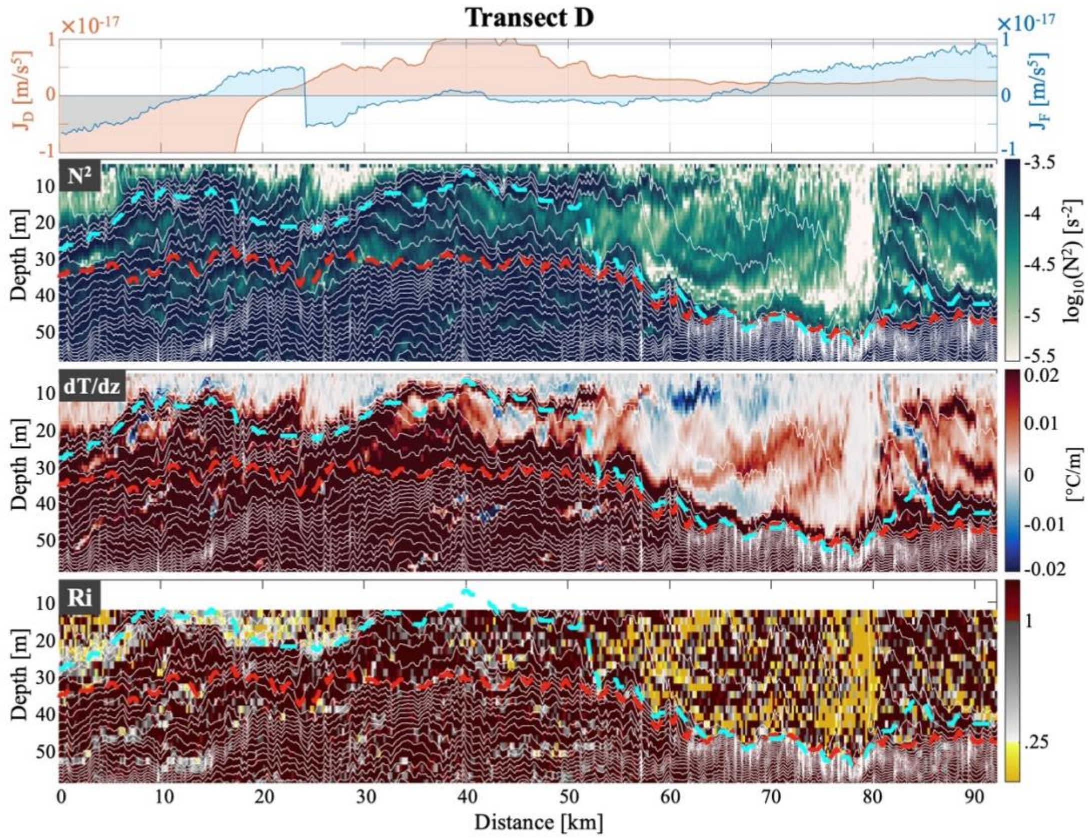
Transect D

encouraging the movement of dense water over light.

These observations demonstrate the complexities associated with intermittent barrier layer and steepening fronts in salinity-stratified regimes. What dynamical processes created and controlled these features? The next section will explore evidence and identify to what extent these features exhibited geostrophic balance, shear instabilities, and secondary circulations.

2.4 Stability Analysis

Our observations show a dense filament that advected into the ocean interior from the coast. A host of instabilities can befall filaments and the fronts found on either edge, which lead to a combination of filament subduction and smaller-scale turbulence. Such submesoscale instabilities are frequently studied theoretically or numerically in isolation. In reality, many instabilities often coincide, “piled atop each other in lovely confusion” (*Waves Across the Pacific*, 1967). Here we go through the potential for different types of instabilities, then discuss ways the observations may exhibit them concurrently.

2.4.1 Geostrophic Balance

We begin by assessing the degree to which the observed front was in geostrophic balance. First, we applied filtering techniques to remove small-scale variability, such as internal waves. A low-pass Butterworth filter was used for the velocity and density fields of each transect. The filter had an 8 km cut-off spatial frequency. Using the smoothed density profile, we calculated the vertical shear expected from geostrophy and compared it to the measured vertical shear derived from the filtered along-front velocity profile, illustrated in Figure 2-6. Previous analyses using this method to test for geostrophy had the capability to use multiple frontal profiles to then use linear regression to quantify the correlation between the observed and

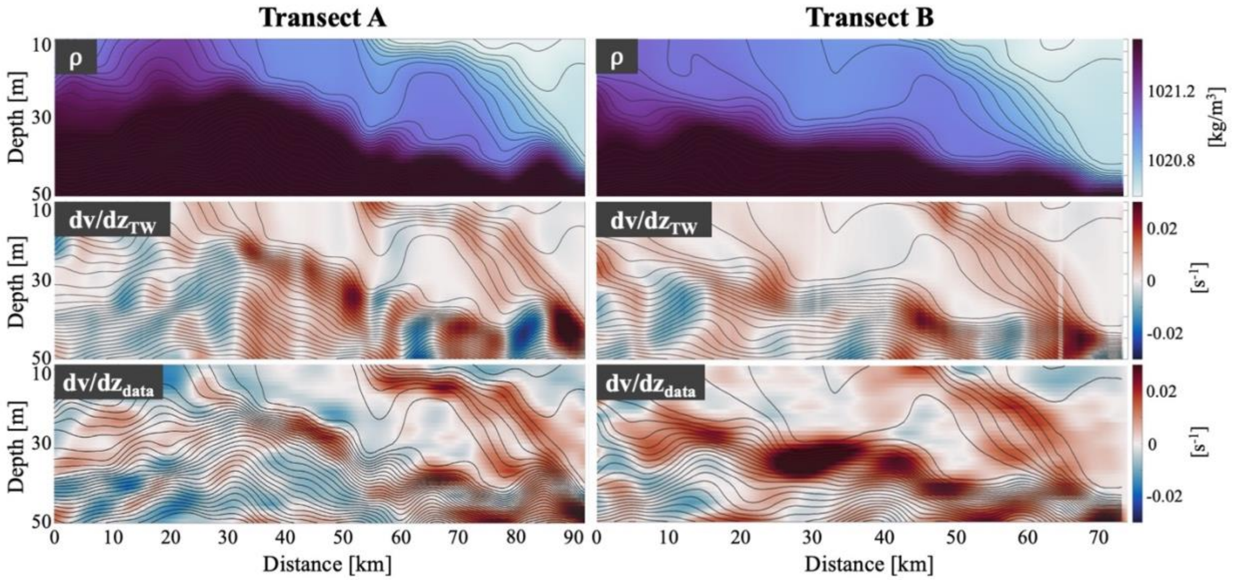

Figure 2-6. Testing for geostrophy on Transects A and B through a comparison of theoretical and measured vertical shear. The top panels illustrate smoothed density profiles used to calculate the vertical shear using geostrophy (TW) in the middle panels. The black lines indicate isopycnals. The bottom panels illustrate measured vertical shear from the shipboard ADCP. The measured vertical shear has been smoothed to compare to the theoretical shear.

expected shear profiles (Ramachandran et al., 2018; Rudnick & Luyten, 1996). Because we were limited in our observations of the front during restratification to two transects, we visually inspected our shear results to conclude that the observed front reasonably suggests thermal wind balance (Figure 2-6). The two transects illustrating the restratifying regions demonstrated elevated shear along the sloping and highly stratified shallow mixed layer in both the observed and modeled shear profiles. In the steepening regions, this analysis suggested that the front is less likely in thermal wind balance (not shown). The non-dimensional quantity $\frac{M^4}{N^2 f^2}$ can also be used to assess the degree to which the geostrophic balance might be expected to hold. For the restratifying region $\frac{M^4}{N^2 f^2}$ is $O(1)$, consistent with geostrophy. For the steepening region, $\frac{M^4}{N^2 f^2}$ is $O(10)$ near the front, indicating a significant departure from geostrophic balance.

2.4.2 Strain-Induced Frontogenesis

When a horizontal deformation flow, typically originating from mesoscale currents and eddies, applies lateral strain to a horizontal buoyancy gradient, strain-induced frontogenesis can occur (Bretherton et al., 1972; Spall, 1995). During frontogenesis, the across-front buoyancy gradient is intensified exponentially, relative vorticity becomes very large, and the Rossby and Richardson numbers become $O(1)$. Frontogenesis results in ageostrophic secondary circulation (ASC), which allows for potentially strong vertical velocities through overturning with upwelling and surface divergence on the light side of the front and downwelling and surface convergence on the dense side. This submesoscale process efficiently transfers variance and energy density to smaller scales (Thomas et al., 2008; McWilliams, 2016).

For systems that are close to a state of geostrophic balance, with small Rossby numbers, the cross-front secondary circulation can be inferred using the Omega equation applied to the measured sloping frontal stratification and cross-front convergence rates (Hoskins et al., 1978). Following the procedure in Rudnick et al. (2022), objective maps were calculated using the four transects across this dense filament. From those, the quasigeostrophic (QG) Omega equation was solved for inferred cross-front and vertical velocity, shown as the white vectors in Figure 2-9(a) for Transect B. The inferred circulation was moving dense filament water downwards and eastwards, through the gateway, into the wedge below the fresher surface water. This inferred secondary circulation was in the sense to subduct the dense filament. The calculated vertical velocities were approximately 5 m/day. It is important to note that because this Quasi-Geostrophic calculation assumes a small Rossby number, while the observed Rossby numbers are $O(1)$, the calculated vertical velocity rates are likely under-estimates, perhaps significantly so.

2.4.3 Richardson Number

Next we calculate several quantities that indicate propensity for smaller-scale instabilities within these sections, starting with the Richardson number. Using the velocity profiles, the Richardson number (Ri) for both transects was estimated to characterize the susceptibility of the water columns to destabilization by vertical shear instability. The equation for Ri is as follows

$$Ri = \frac{N^2}{\left(\frac{du}{dz}\right)^2} \tag{2.1}$$

where N^2 is the observed stratification and $\frac{du}{dz}$ is the observed vertical shear. Shear was calculated by differentiating horizontal velocity at its binned resolution of 2 meters. To compute the stratification, density was interpolated to the vertical resolution of the velocity data. An Ri value of 0.25 or less indicates a propensity for vertical instability (Caulfield & Peltier, 2000; Lucas et al., 2016). As depicted in Transect A of Figure 2-3, Ri tended to be less than 0.25 within the deep mixed layer and intermittent barrier layer, corresponding with the weaker stratification found there. The barrier layer observed at night in Transect B exhibited Ri values less than or equal to 0.25 more commonly than the barrier layer observed during the day. The destabilized regions within the barrier layer observed during the day in Transect A were accompanied by patches of Ri of O(1-10), signifying stable regions within the barrier layer. In the region where the front steepens (Transects C and D), there was complex variability in Ri with many stable regions vertically and laterally adjacent to unstable regions, shown in Figure 2-5. As the weakly stratified column formed, Ri became consistently less than 0.25 at the frontal axis and the surrounding regions can be described as majorly O(1). The tail of weak stratification beneath the filament and at the base of the mixed layer also had a signature of Ri less than 0.25.

2.4.4 Potential Vorticity

The stability of a fluid can also be characterized by its potential vorticity (PV) signature, which quantitatively assesses the vorticity and stratification of water parcels. PV is considered to be a tracer, conserved within isopycnal surfaces and is ideally altered only through diabatic and frictional processes (Vallis, 2017; Taylor & Thompson, 2023). For this study, we analyzed the Ertel potential vorticity of the transects defined by

$$q = \left(f + \frac{dv}{dx}\right)N^2 - \frac{dv}{dz}M^2 \tag{2.2}$$

decomposed into three components, with the first component describing the product of the Coriolis term and vertical stratification (stretching term), the second component describing relative vertical vorticity and vertical stratification (vorticity term), and the third component describing the horizontal component of vorticity and lateral buoyancy gradients (tilting term) (Thomas, 2005, 2008). A flow is considered stable if fq is positive, and unstable if fq is negative or near-zero. In order to apply this model to our observations, the “one-ship method” was used to approximate vertical vorticity by calculating the across-front gradient of the along-front velocities (Ramachandran et al., 2018; Shcherbina et al., 2013). Additionally, Ertel PV was calculated using the same smoothed sections of velocity and density used to test for thermal wind balance.

For the restratifying front (Transects A and B), the intermittent barrier layer and deep mixed layer were characterized as having low or “near-zero” PV ($O(10^{-9}\ \mathrm{s}^{-3})$), as shown in Figure 2-7. This low PV arm extended from the deep mixed layer and through the gateway into the barrier layer for over 50 km in both transects. Vertical shear and low stratification were responsible for the low PV evident in Figure 2-8 for Transect B. Highly stratified regions, such as the region bounding the base of the mixed layer, had positive PV with magnitudes $O(10^{-8}\ \mathrm{s}^{-3})$ or greater. At the gateway, where the front was sharpest, negative patches of PV were observed

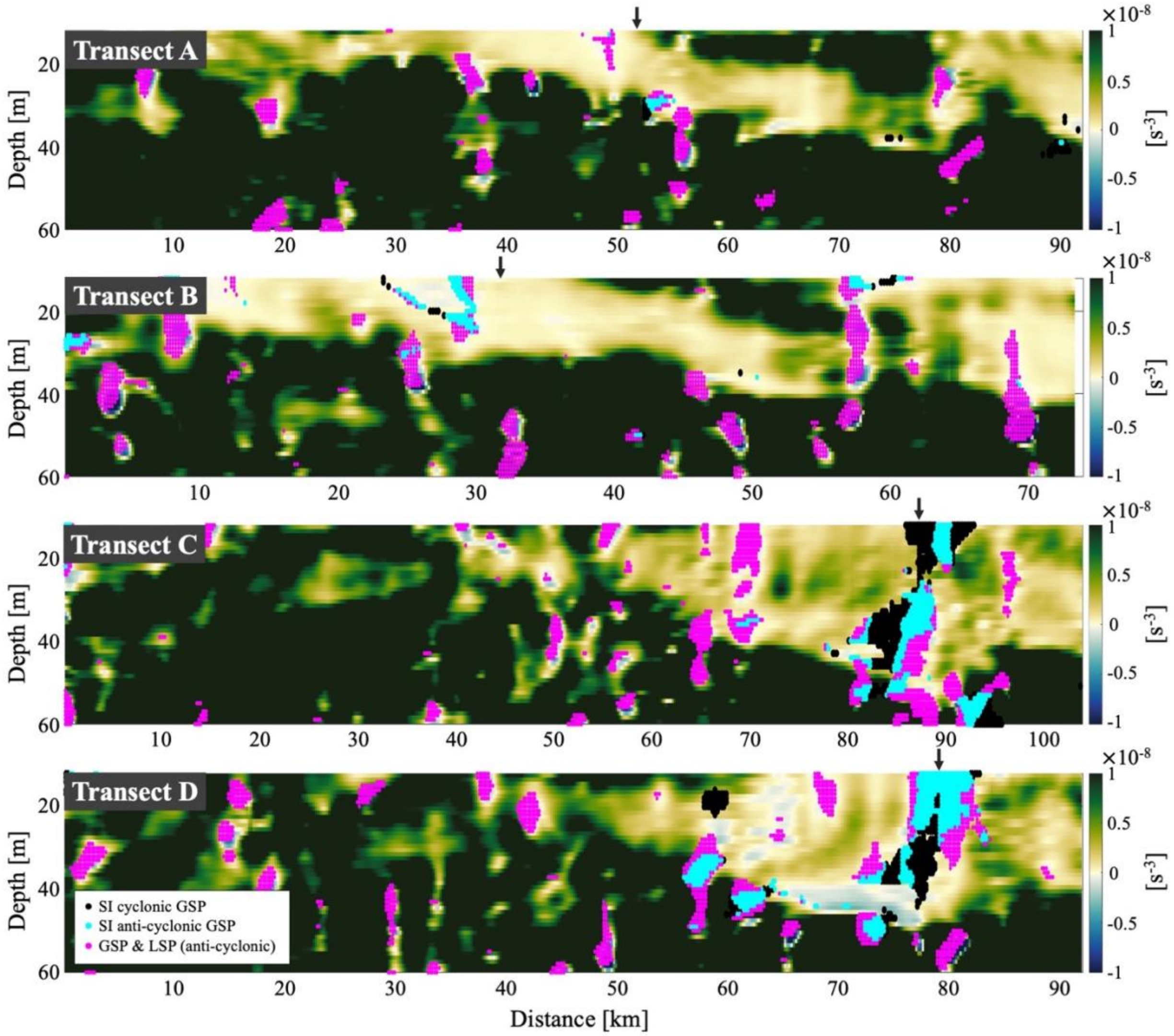

Figure 2-7. Potential vorticity for Transects A, B, C, and D. The black dots indicate regions where the criteria for SI produced through cyclonic geostrophic shear production is met. Cyan dots represent SI produced through anticyclonic geostrophic shear production. Pink dots represent a combination of symmetric and inertial instability produced through anticyclonic geostrophic and lateral shear production. The small black arrows indicate the frontal axis of each region.

($O(10^{-10}\ s^{-3})$), with the vorticity term responsible for its magnitudes. These negative PV patches are highlighted by pink, blue, and black indicators in Figure 2-7 for the instabilities described in the next section. The gateway marked a transition from negative to positive PV and the temperature inversions found on the light side of the gateway, are composed of and encompassed in low, but positive PV.

Theory suggests that Ertel PV cannot be transported through isopycnal surfaces and can only be altered where either the surface outcrops or mixing occurs (Haynes & McIntyre, 1987; Marshall & Nurser, 1992). If there is a cross-front agoestrophic circulation happening at the front, then PV would be expected to be transported along isopycnal surfaces and subduct, and would be conserved apart from diabatic effects. However, if a flow deformation field is present, which is likely in a frontal region, the buoyancy gradients and absolute vorticity can change (Thomas, 2005). Simulations have demonstrated that during subduction, parcels of low PV can transition from a baroclinically low state to a vortically low state through decreases in both relative vorticity and lateral buoyancy while maintaining the total PV (Thomas, 2008). Baroclinically low PV can be described as regions with nonzero absolute vorticity and stratification. In contrast, vortically low PV can occur in regions where there is nonzero stratification, zero absolute vorticity, and no lateral buoyancy gradient (McWilliams, 1985; Thomas, 2008). In these regions, submesoscale coherent vortices (SCVs) can form through the generation of anti-cyclonic vorticity resulting from vortex squashing as the total PV is maintained (Spall, 1995; Thomas, 2008). SCVs can be characterized by coherent regions of weak stratification, anticyclonic vorticity, low PV within its core, an interior maximum in the velocity field, and a small lateral width comparable to the Rossby radius of deformation (McWilliams, 1985; Thomas, 2008).

Our observations exhibited evidence of these dynamics, as the gateway in Transects A and B marked a transition between baroclinically low PV to vortically low PV, with the magnitude of the lateral buoyancy gradients and absolute vorticity tending towards zero in both profiles. Figure 2-8 points to these regions in Transect B where the tilting term of PV was large relative to the other components and contributing to negative PV ($O(10^{-10})$) at the gateway, and

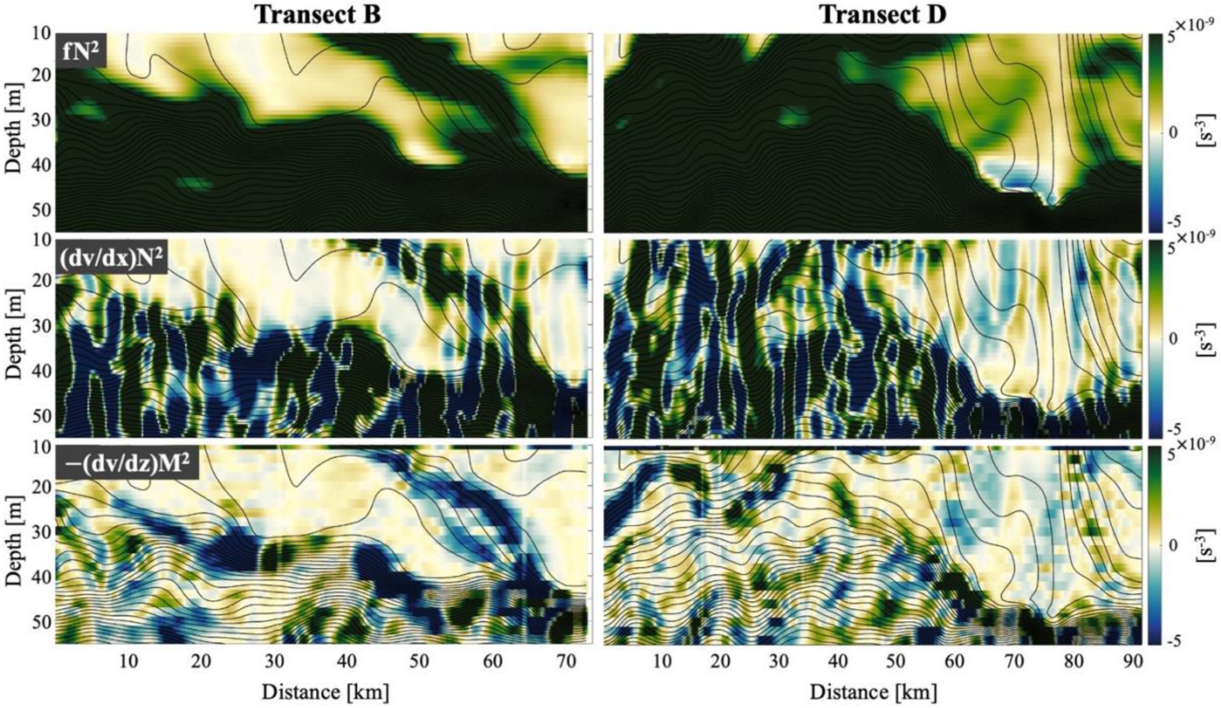

Figure 2-8. Potential vorticity components (Equation 2.2) for Transects B and D. The black lines indicate isopycnals.

the vorticity term of PV was large and negative on the eastern side of the gateway. The filtered submesoscale velocities for Transect A revealed a bolus in this region, which may be characterized as a SCV. This feature is highlighted in the first panel of Figure 2-7 near x = 53 km and z = 30 m by the cyan SI anti-cyclonic GSP indicators. The SCV appears to be proximal to the temperature inversion, illustrating its formation as a 3-dimensional process.

The steepening regions of Transects C and D also indicated low or negative PV ($O(10^{-9}\ s^{-3})$) (Figure 2-7). The filament and the frontal axis exhibited low stratification throughout the mixed layer and the surrounding highly stratified regions had PV $O(10^{-8}\ s^{-3})$. In Transect C, anticyclonic vorticity near the surface at the front contributed to a region of negative PV at the surface. Later in Transect D, lateral buoyancy gradients and vertical shear contributed to a large region of negative PV throughout the mixed layer and spanning approximately 5 km at the frontal axis, as illustrated in Figure 2-8. The weakly-stratified tail at the base of the mixed layer extending for 25 km is also characterized by negative PV driven by a region of unstable stratification.

2.4.5 Symmetric and Inertial Instability

In the previous section, we discuss stability in the context of potential vorticity and characterize the types of PV observed in our sections. Various instabilities can develop when PV is negative, and since we identified regions of negative PV near the surface and gateway, we explored the possibility of the occurrence of symmetric and inertial instability during our survey. Symmetric instability (SI) is a shear instability that can extract kinetic energy from geostrophic currents, transferring the energy to smaller scales and develops when the component of PV attributed to horizontal vorticity and buoyancy gradients are greater than the component attributed to vertical vorticity and stratification (Thomas et al., 2013). Inertial or centrifugal instability can arise when the vorticity term of PV is negative (Thomas et al., 2013; Ramachandran et al., 2018). To define and differentiate between the criteria for each instability to occur, we use the balanced Richardson number and information regarding the vertical vorticity of each region (Thomas et al., 2013). The balanced Richardson number is expressed as

$$Ri_B = \frac{f^2 N^2}{|\nabla_h b|^2} \tag{2.3}$$

And to be able to account for inertial and centrifugal instability, we express the balanced Richardson number as an angle

$$\phi_{Ri_B} = \tan^{-1}\left(\frac{|\nabla_h b|^2}{f^2 N^2}\right) \tag{2.4}$$

and utilize a similar parameter describing the vorticity

$$\phi_c = \tan^{-1}\left(\frac{\zeta_g}{f}\right) \tag{2.5}$$

Using these parameters, we tested for three categories of symmetric and inertial instability. The first category describes regions of cyclonic vorticity that meet the condition for SI and extracts energy from geostrophic shear production, which can be described when $\phi_c < -45°$ and $-90° < \phi_{Ri_B} < \phi_c$. Geostrophic shear production is driven by the third term (tilting term) in Equation 2.2. The second category describes regions of anti-cyclonic vorticity in which both geostrophic and lateral shear production contribute to the dynamics and when $\phi_c > -45°$ and $-90° < \phi_{Ri_B} < -45$. Lateral shear production is driven by the sum of the first two terms in Equation 2.2 (stretching and vorticity terms). In this category, if the geostrophic shear production outweighs the lateral shear production, then the criteria is met for SI. For the final category, if vertical stratification is greater than vertical shear in a region with anti-cyclonic vorticity, or when $-45° < \phi_{Ri_B} < \phi_c$, then geostrophic and lateral shear production contribute to the energetics and a combination of inertial/centrifugal and symmetric instability results.

Figure 2-7 marks where the criteria for each type of instability was met. For Transect A of the restratifying front, SI that is produced through anti-cyclonic geostrophic and lateral shear production on the dense side of the gateway was suggested. For Transect B, all three types of SI were indicated near and at the gateway on the dense side. Aligned vertically with the gateway were parcels that meet the conditions for SI produced through both anti-cyclonic geostrophic shear production and the combination of anti-cyclonic geostrophic and lateral shear production. Extending laterally from this region and towards the center of the filament, conditions were met for SI produced from cyclonic geostrophic shear production. For the region where the front was steepening (Transects C and D), the criteria indicated that the axis of the front at the surface may have been undergoing SI through anti-cyclonic geostrophic shear production. SI through cyclonic geostrophic shear production surrounded this region on both the dense and light sides of the front. At depth, all types of SI were indicated where PV is extremely small or negative. This unstable region stretched nearly 10 km and extended down to the mixed layer depth. As the front evolved hours later in Transect D, all three types of SI were expected at the frontal axis extending approximately 10 km and throughout the weakly-stratified mixed layer.

To gain a deeper understanding of the mechanisms that allowed for the criteria of SI to be met in these regions near the gateway of the restratifying front, we examined the density and shear variability around 12 meters depth and sought to understand how PV transitions from negative to positive. An example of this analysis can be found for Transect B in panel (b) of Figure 2-9. In Transect A, PV transitioned from negative to positive due to the variability in the lateral buoyancy gradient, namely through an increase in buoyancy (Figure 2-7, x = 48-50 km). This was where criteria were met for SI via geostrophic and lateral shear production. In this region, the stretching and vorticity terms of PV cancelled each other out, while the tilting term increased due to negative vertical shear within a dense anomaly, thus leading to negative PV ($O(10^{-10}\ \mathrm{s}^{-3})$). The lateral buoyancy gradient, locally controlled by salinity with a 40% temperature influence, determined the overall variability of PV in this region. Moving toward the gateway, the lateral buoyancy gradient began to increase and the stretching term controlled the variability of the lateral shear production term, yet, the geostrophic shear production term continued to determine the overall PV variability. When the total PV equaled 0, the stretching term was responsible for the remainder of the lateral shear production, which then balanced the geostrophic shear production. This suggests that the influence of frontal strength on the potential vorticity balance and dynamical stability was equally significant as the Coriolis forcing and stratification. At the gateway and towards the lighter side of the front, the total PV increased exponentially up to at least 2 orders of magnitude higher than the unstable regions ($O(10^{-8}\ \mathrm{s}^{-3})$)

with the stability determined by the stretching term. Because Transect B was observed during a period of cooling, the surface ocean and mixed layers can be described generally as unstable due to atmospheric PV extraction. Negative PV was found for more than 5 km, extending from the gateway to the dense side of the front (Figure 2-7 and Figure 2-9(c), x = 24-30 km). Similar to Transect A, PV approached 0 due to a balance in the remainder of the lateral shear production controlled by Coriolis and stratification and the geostrophic shear production controlled by lateral buoyancy gradients. Unlike Transect A, however, the lateral buoyancy gradient was controlled by temperature variability. This variability is visible as this region presents itself within the front as a temperature anomaly (Figure 2-9(a)). As the front became lighter away from the gateway, PV increased to $O(10^{-8}\ s^{-3})$ due to variability in lateral shear production.

In order to explore the robustness of these results, we conducted a sensitivity analysis to determine whether the ship track orientation relative to the true frontal axis could influence the vorticity calculated from the one-ship method, thus biasing the criteria for SI. To test this, the estimated along-front angle was adjusted to have a margin of error of 45° clockwise and counterclockwise. Vorticity was calculated from the new rotated velocity fields and used to test for SI. We then calculated the probability of the occurrence of SI for each along-front angle within the regions of concern. We found that for SI produced through cyclonic or anticyclonic geostrophic shear production, the likelihood of the criteria being met as presented is high if the margin of error for the angle of the frontal axis is 20° clockwise or counterclockwise. For SI produced through anti-cyclonic geostrophic and lateral shear production, the likelihood of the criteria being met as presented is high if the margin of error for the angle of the frontal axis is 45° clockwise or counterclockwise. These results indicate that the evidence of SI shown in Figure 2-7 demonstrates a considerable robustness.

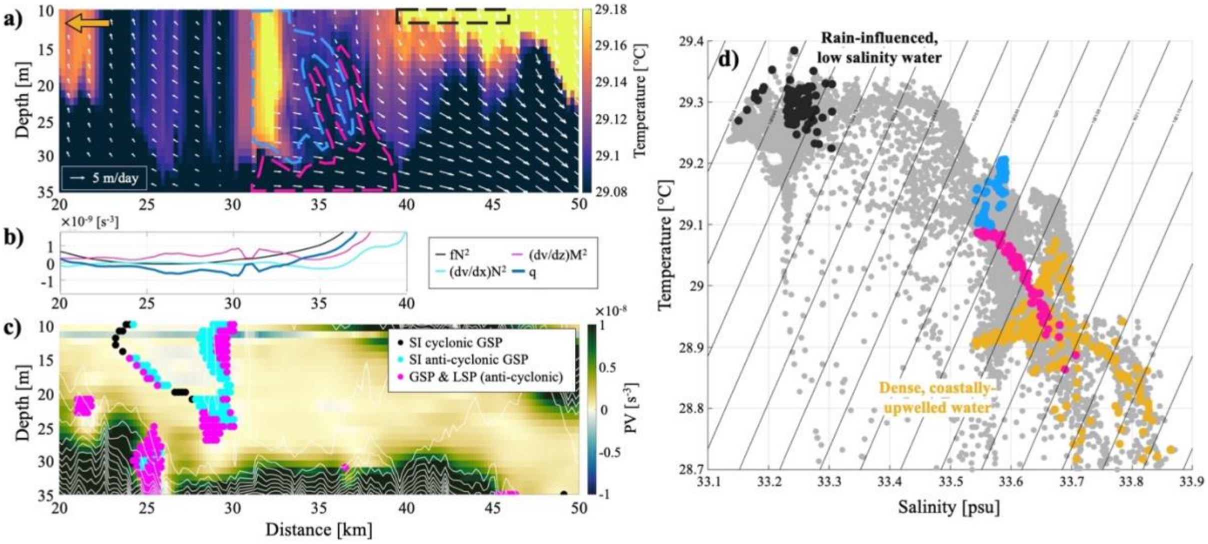

Figure 2-9. Detailed depiction of the gateway in Transect B. The top left panel (a) is the temperature profile. The white arrows indicate vertical velocities derived from the Omega equation; note that the scale arrow gives a reference speed only for the *vertical* component of this ageostrophic circulation. The dashed pink and blue lines are regions that correspond to the pink and blue data points in the T-S diagram (d). The left middle panel (b) plots the components of PV near the surface (depth-averaged 10-15 m). The bottom-left panel (c) shows potential vorticity with indicators for SI similar to Figure 2-7. The white lines indicate isopycnals at intervals of 0.04 kg/m^3. The right panel (d) illustrates Transect B in T-S space, with the gray dots indicating the full span of the transect. The black data points are a subset of the frontal region representing the ambient low salinity water, also indicated by the black dashed line in (a). The gold data points are a subset of the center of the coastally-upwelled filament (not shown but indicated by the gold arrow in (a) between 0-10 km).

2.4.6 Potential Vorticity Injection and Extraction

PV in the ocean boundary layer can be altered by atmospheric forces, which may encourage or inhibit the submesoscale dynamics at play. PV can be reduced from a surface layer through PV extraction when a destabilizing buoyancy flux is applied from the atmosphere. This convective activity can occur when wind blows in the direction of a frontal jet, such that dense water is advected over light, or when there is cooling (Taylor & Ferrari, 2010). PV can be injected into the surface ocean when a restratifying force is applied from the atmosphere, such as solar heating, precipitation, or up-front Ekman transport. Theoretically, PV is modified through atmospheric forcing or turbulence until it subducts into the interior of the ocean where it behaves like a conservative tracer (Thomas, 2005; Taylor & Ferrari, 2010). Following the PV flux scaling arguments presented in Thomas (2005), we explore the influence the atmosphere may have on the magnitudes of PV observed and the submesoscale dynamics. The PV flux due to surface buoyancy forcing, J_D is expressed as

$$J_D = f^2 \frac{B}{H} = \frac{1}{H} f \left(g\alpha \frac{Q_{net}}{\rho c_p} - g\beta S(E-P) \right) \tag{2.6}$$

where B is the buoyancy flux due to surface forcing, H is the MLD, g is gravity, α is the thermal expansion coefficient, β is the haline contraction coefficient, Q_{net} is the diurnal heat flux, ρ is the sea surface density, c_p is the specific heat of seawater, S is the sea surface salinity, E is the evaporation rate, and P is the precipitation rate. The PV flux due to wind or frictional forcing, J_F, is expressed as

$$J_F = 2.5|\nabla_h b| f^2 \sqrt{\frac{\tau}{\rho}} \tag{2.7}$$

τ is the wind stress.

Prior to and during the front crossing in Transect A, the atmosphere maintained a restratifying effect on the ocean boundary layer through diabatic heating, and theoretically injected PV into the ocean surface ($J_D < 0$). Throughout the survey of Transect B, the ocean boundary layer experienced convection due to atmospheric cooling ($J_D > 0$). The transects were distinct in that Transect A broadly presented higher values of stratification and integrated PV in the ocean boundary layer relative to Transect B. When the steepening region of the front (Transects C and D) was observed, it was subjected to cooling, which would extract PV ($J_D > 0$) from the surface and allow for convection within the interior. J_D was generally $O(10^{-17}$ m/s$^{-5})$ during periods of diabatic heating and $O(10^{-18}$ m/s$^{-5})$ during periods of cooling, while the J_F

maintained values that were *O*(10^{-18} m/s^{-5}) as shown in Figures 2-3 and 2-5. Because the winds originated from the south and southeast, the Ekman buoyancy flux would encourage the movement of the dense filament over the lighter waters, which would have a convective effect and extract PV from the ocean surface.

2.5 Discussion

These observations showcase the complexities that can occur in salinity-controlled frontal regions. These submesoscale processes have implications for the heat content and stratification of the ocean boundary layer in the Bay of Bengal. Above we have described the complexity of observed processes in the data, then calculated the propensity for various instabilities to be at play. Here we discuss connections between the calculations indicating instabilities and the more complicated reality. Both the observed behavior and the propensity for different instabilities and secondary circulations, vary considerably across the four sections shown here.

On the broadest level, the frontal features shown here are all within a region of mesoscale confluence. As such, QG theory suggests that such a confluence should lead to an ageostrophic secondary circulation with downwelling/subduction of the dense filament. In the first two transects, the observed velocities share some of the large-scale confluence with the altimetry estimates (Figure 2-1). Inferred ageostrophic circulation suggested a downwelling of fluid through the gateway below the main front on the order of 5 meters a day (Figure 2-9). Given that Rossby numbers are *O*(1) here, the actual rate may have been stronger. Analysis of temperature and salinity profiles confirmed that there was a broad movement of filament water subducting into the wedge below the fresher near-surface water in Transects A and B. As that water subducted into the narrowing wedge, there is a trade-off of PV components, with increased squashing and a compensating development of relative vorticity (Figure 2-6). On the whole, the water mass preserves its total low PV, extending from the surface down into the wedge. The evolving relative vorticity appeared to create the sort of submesoscale coherent vortex that has been observed in previous observational and numerical process studies (McWilliams, 1985; Spall, 1995; Bower et al., 1997; Serra et al., 2005; Thomas, 2008; Sarkar et al., 2016; Gula et al., 2019). On the light side of the front, upwelling associated with the secondary circulation may have produced relatively higher PV near the surface (Figure 2-8, upper left).

On smaller scales, dramatic stripes were visible most clearly as tilted temperature inversions in all transects (Figures 2-3, 2-5). Some facets of these tilted stripes were consistent with what one would expect for SI. For example, T-S analysis of the tilted features within the gateway in Transect B shows tongues of downwelling water interspersed with tongues of upwelling water from the base of the surface boundary layer (Figure 2-9). For low values of the Rossby number, the tilted convection of SI moves *along* isopycnals, and hence is not easily visible in density (Bachman & Taylor, 2014). However, when there are significant spice gradients along isopycnals (as temperature here is largely passive), temperature can be a tracer of along-isopycnal movement. Furthermore, for non-small Rossby numbers, SI convection may cross isopycnals, with angles within some range of the frontal angle itself (Bachman & Taylor, 2014). Here in Transect B, the temperature inversion stripes tilted in the same sense as the main front, with an angle in between the main front on top of the wedge to their east, and the more vertical isopycnals in the mixed layer to their west. Also consistent with theory, the vertical wavenumber of the features shown was nearly the full boundary layer, while the horizontal wavelength was roughly consistent with $k/m \sim M^2/N^2$ (Bachman & Taylor, 2014). All four transects also showed sloping temperature inversions on the light side of the front, near the eastern end of each section. These tended to have a shallower slope, paralleling the slope of tilted isopycnals in this region.

There were some suggestions that the areas of observed sloping temperature inversions were adjacent to areas of negative PV, where the instability analysis indicated that SI should occur (Figure 2-7), though the correlation was not perfectly clear. For example, for the sloping features in Transect B at the start of the gateway, PV was not negative right at that location, but it was negative slightly further to the west. If we interpret these subsequent sections as partly evolution in time as the filament moves around this large-scale eddy, we can also consider the situation near the gateway ‘earlier’, in Transect A. There, PV is low, in part due to decreased stratification from night-time convection. Given that it takes SI a finite time (hours) to develop, the stripes observed in Transect B could be evidence of SI that was initiated between the times of Transects A and B (11 hours between gateway crossings). Or, it may be that this was a situation where viewing the evolution of the front as consisting of an isolated instability is insufficient. Instead, perhaps the combination of strong frontogenesis inducing convergence and negative PV broadens the criteria for an instability of this sort to develop. In other words, the ASC and SI tendencies could be working in concert here to initiate filament subduction and produce the detailed sloping substructure of down/upwelling observed. New numerical modeling of such a situation will be useful to disentangle these dynamics.

In the second pair of transects, a developing submesoscale eddy (Figure 2-1) led to strong convergence and vorticity on even smaller scales. That submesoscale eddy could have arisen from a barotropic lateral shear instability (Gula et al., 2014; Munk et al., 2000) of the large mesoscale eddy currents; detailed analysis of that is beyond the scope of this work. We note that the convergence at the front became two times larger over the course of the survey. At the front, warm water can be seen plunging at a rate of 5 meters in 4 hours between sections C and D. This waterfall of heat may have been a direct result of this submesoscale convergence on these short timescales (Barkan et al., 2019).

The PV patterns in these second two transects also changed more generally. While both regions suggest the potential for (SI), Figure 2-8 demonstrates the contrast in spatial extent to which horizontal vorticity and lateral buoyancy gradients drive PV negative. For Transect D, the tilting term of Equation 2.2 was large and extended expansively across the front and into the mixed layer compared to Transect B, where the term was smaller and only dictated PV near the surface.

Though we have considered a range of instabilities and mechanisms, there are likely additional dynamical influences at play here which we do not have the observational temporal and spatial resolution to assess. For example, previous work has shown near-surface near-inertial oscillations to be prevalent in this region (Johnston et al., 2016; Adams et al., 2019). Some of the changing direction of observed currents along these four transects (Figure 2-1) may reflect rotating near-inertial currents, superimposed on mesoscale and sub-mesoscale motions. With the selected transects representing only 2.2 days of data and an inertial period of 1.8 days, it is difficult to detangle; hence we have not attempted to 'remove' the inertial signal. For most of the calculations discussed here, the most relevant features of velocity are the vorticity and convergence, which were dominated by gradients on much smaller scales than the scales given by a slow inertial rotation. However, inertial motions may play an important role in the tilting term of PV through strong inertial vertical shear acting on submesoscale lateral density gradients. Even if that shear reverses on an inertial timescale, instabilities like SI can develop in much shorter time periods (Thomas et al., 2016).

Furthermore, we did not consider the curvature of the large-scale eddy currents that advect this filament, which may be important. Including cyclogeostrophic terms in PV can be *O*(1) (Buckingham et al., 2021; MacKinnon et al., 2021). Additionally, parallel analyses on this dataset have shown that spatially-varying precipitation in this region enhanced the lateral buoyancy gradient— patchy rain is also frontogenetic.

Some facets of these results are similar to both previous observational work and idealized modelling studies. Ramachandran and Tandon (2020) simulated temperature inversions that can be characterized by low stratification, low PV ($O(10^{-10}$-10^{-9} $s^{-3}))$, anticyclonic vorticity, lateral scales of *O*(1-10 km), vertical scales of *O*(10 m), and inversion magnitudes that reflect surface temperature variability, all attributes found in our observations. However, the vertical extent of the temperature inversions reflected the thickness of the pycnostads, whereas some inversions in our observations cross isopycnals (Figure 2-3). Other observations of temperature inversions show coherent structures that cross isopycnals, similar to our observations, but the lateral scales tend to be *O*(10-100 km), indicative of other formation processes (Adams et al., 2019; Shroyer et al., 2020; Jaeger et al., 2020).

The simulations of Sarkar et al. (2016) also exhibited dynamics similar to what we observe, with weakly stratified, anticyclonic regions of low PV near the outcrop of a front and the formation of submesoscale coherent vortices. Temperature inversions were found to be generated through quasi-adiabatic subduction; the anticyclonic vorticity that develops is attributed to the tilting of vertical temperature gradients and vortex squashing, as evident in our observations. The submesoscale bolus we observe beneath the outcrop of the front in Transect A is characteristic of SCVs that develop with weakly stratified waters through surface convergence and the conservation of PV.

Surface cooling may have served as a catalyst for SI as convection disrupts patterns of stratification while simultaneously increasing shear. We observed heightened evidence of SI in Transect B during cooling, as the region where the criteria is met is broader and extends deeper than that of Transect A (Figures 2-3 and 2-7). Past observations have suggested that the barrier layer is shielded from atmospheric forcing, however, these profiles offer new insights of how barrier layers associated with 3-dimensional processes may be indirectly affected by atmospheric forcing (Thadathil et al., 2002; Sengupta et al., 2016). The gateway facilitates a link between a region that is directly impacted by atmospheric forcing and a region sequestered away from it. Perhaps not coincidentally, the barrier layer was less stratified overall during a period of cooling and convection compared to that of the barrier layer during a period of heating.

In addition to the two-dimensional analysis above, features shown in this data may reflect lateral stirring of fully three-dimensional eddies and other instabilities. For example, some features here are reminiscent of the "submesoscale sheared eddy twist" introduced in Jaeger et al. (2020), where an eddy formed at the lateral boundary of the front twists a horizontal spice gradient, generating multiple coherent spice layers. On a broader scale, the thickness of the intermittent barrier layer may allow for more effective lateral stirring throughout this region. The Rossby radius of deformation in the barrier layer was approximately 2-4 km depending on the average stratification, whereas it was 1 km or less in the adjacent shallow and deep mixed layers. This is evident by the SCV formed and identified in Transect A, which was approximately 3 km wide. Collectively, the processes at which the barrier layer stirs and advects water masses within it has important implications for the stratification beneath salinity-controlled fronts and the overall heat content of the boundary layer.

2.6 Conclusion

Our observations illustrate the evolution of a salinity-controlled dense filament adjacent to fresher water in the Bay of Bengal. On one side of the filament, the front was observed to undergo lateral restratification over hours to days. The restratification process created an intermittent barrier layer bounded by a discrete ‘gateway’, facilitated by what appear to be both SI and ASC acting in concert. The concept of the gateway illustrates a connection between the deep and shallow mixed layers at fronts with barrier layers, and the submesoscale dynamics and instabilities that are associated with it exemplify how heat and salt are vertically and laterally exchanged. Slightly later, the front was observed to steepen dramatically, as a result of submesoscale convergences. Those convergences led to plunging vertical velocities and downward heat transport.

The Bay’s spiciness allows for surface heat within small-scale variability to be injected into the interior through submesoscale instabilities, thus creating temperature inversions and contributing to a warmer subsurface. These results continue to demonstrate the need for models to resolve O(1 km) thermohaline variability in order to accurately represent 3-dimensional processes in the Bay of Bengal. The frontal dynamics observed here not only modulate the heat content sub-surface and within barrier layers, but allow for the heat in small-scale variability to be sequestered from the surface, limiting the atmosphere’s access to this heat. It is likely that these features and processes are ubiquitous throughout the Bay because of its strong lateral surface variability due to significant freshwater influence.

2.7 Chapter Acknowledgements

Chapter 2, in full, is a reprint of the material as it appears in Journal of Geophysical Research: Oceans 2024. McKie, Taylor; Lucas, Andrew; MacKinnon, Jennifer, Wiley Online Library, 2024. The dissertation author was the primary investigator and author of this paper. This work was supported by Office of Naval Research Grants N00014-17-1-2511 and ONR N00014-17-1-2391. This material is also based upon work supported by the National Science Foundation Graduate Research Fellowship Program under Grant No. DGE-2038238. The authors would like to express gratitude towards the science party and crew of the Summer 2019 MISO-BoB Cruise onboard R/V *Sally Ride* as well as all technical staff with the Multiscale Ocean Dynamics Laboratory at Scripps Institution of Oceanography and Woods Hole Oceanographic Institution for their work and contributions in collecting and managing the in-situ data. We would also like to thank Dan Rudnick for his help in carrying out the Omega equation calculations. Finally, we would like to thank two anonymous reviewers for ideas and suggestions that helped improve the paper.

Chapter 3 A SHIFTING MESOSCALE IN THE GULF OF MEXICO

3.1 Introduction

The Loop Current (LC) contributes significantly to the circulation of the Gulf of Mexico (GoM), and its behavior may be subject to change with a warming climate. Factors that impact the dynamics of the LC are known to exhibit trends attributed to climate change, but it is not yet certain how the LC and the dynamics that spur from it may be altered. Much of research on the LC still focuses on understanding the mechanisms that lead to its nonlinear behavior. The LC flows from the Yucatan Channel to the Florida Strait and periodically grows, increasing its surface area, intruding into the Gulf as far north as 28N and forming anticyclonic eddies as it turns eastward (Pichevin & Nof, 1997; Nof & Pichevin, 2001; Sheinbaum et al., 2002; Leben, 2005; Rousset & Beal, 2010; Donohue et al., 2016a; Hamilton et al., 2016; Lugo-Fernández et al., 2016; Yang et al., 2020). These anticyclonic eddies, called Loop Current eddies (LCE), detach from the LC, most times with aid from cyclonic eddies called Loop Current frontal eddies (LCFE) squeezing the LC on its eastern and western sides (Hurlburt & Thompson, 1980; Hurlburt, 1986; Zavala-Hidalgo et al., 2002; Chérubin et al., 2006; Donohue et al., 2016a; Jouanno et al., 2016; Hiron et al., 2020). Once separated, LCEs have diameters *O*(100 km) and advect westward at about 2-5 km/day, transporting heat and nutrients throughout the basin as they decay until their dissipation on the western shelf. The LC then retracts just south of 24N, impending a repeat of this process that occurs every 3-17 months (Sturges& Leben, 2000; Hamilton et al., 2002; Leben, 2005; Donohue et al., 2016a; Hall & Leben, 2016; Lugo-Fernández et al., 2016; Gough et al., 2019; Justić et al., 2022; Meunier et al., 2024).

The mechanisms that lead to these dynamics have puzzled scientists for decades, and while a dominant mechanism has not been identified, theories have been developed and processes linked to LC behavior have been evident (Sheinbaum et al., 2016). The LC interacts with the topography of the Campeche Cape and the Mississippi Fan, constraining the flow and creating ideal conditions for instability (Hurlburt, 1986; Chérubin et al., 2006; Oey, 2008; Le Hénaff et al., 2012; Huang et al., 2013; Donohue et al., 2016b; Hamilton et al., 2016). Because the flow of the LC is northward, the current experiences the beta effect, which may affect the size and generation frequency of LCEs (Hurlburt & Thompson, 1980; Pichevin & Nof, 1997; Nof & Pichevin, 2001; Nof, 2005; Oey et al., 2005; Hénaff et al., 2012). A proposed theory suggests that the LC attempts to conserve momentum by shedding eddies as it enters and exits the basin (Pichevin & Nof, 1997; Nof & Pichevin, 2001; Nof, 2005). Conservation of potential vorticity is another mechanism that facilitates the shedding of eddies as the core of the LC introduces negative potential vorticity to the basin as it increases in surface area and is modified by the beta effect (Charney & Stern, 1962; Chérubin et al., 2006; Hénaff et al., 2012; Lugo-Fernández et al., 2016). This creates a strong potential vorticity gradient across the LC at the surface and at depth, indicative of barotropic and baroclinic instability (Charney & Stern, 1962; Chérubin et al., 2006). The increase in negative potential vorticity is accompanied by an increase in available potential energy, that then fuels kinetic energy driven by barotropic and baroclinic instabilities throughout the entire water column (Charney & Stern, 1962; Hurlburt & Thompson, 1980; Marshall et al., 2002; Chérubin et al., 2006; Donohue et al., 2016a; Hiron et al., 2020; Lugo-Fernández, 2023). The growth of both LCEs and LCFEs are fed from these processes (Hurlburt & Thompson, 1982; Hurlburt, 1986; Marshall et al., 2002; Chérubin et al., 2006; Jouanno et al., 2016; Hiron et al., 2020; Moreles et al., 2021). While these dynamics may have more of a direct impact on the eddy shedding process, patterns associated with these dynamics have also been observed. Prior to shedding events, the Yucatan Channel experiences meridionally-propagating vorticity perturbations, a reduction in volume transport, and wind-forced variations (Chang & Oey, 2012, 2013; Hamilton et al., 2016; Sheinbaum et al., 2016). Some of these effects are also said to determine the shedding period of LCEs (Lugo-Fernández et al., 2016). The dynamics that influence or accompany the behavior of the LC may be impacted as climate change alters the strength of currents, warms basin waters and raises sea level.

One factor known to have a possible impact on the dynamics of the LC is the deceleration of the Atlantic Meridional Overturning Circulation (AMOC). With the AMOC slowing down, it is projected that the volume transport through the Yucatan Channel that feeds the LC will be reduced by at least 20% (Liu et al., 2012; Moreles et al., 2021; Wang et al., 2023). The changes in this flow could influence the available potential energy of the LC that facilitates the shedding of eddies (Moreles et al., 2021). Secondarily, sea level in the Gulf of Mexico has been detected to rise faster relative to the global mean, with rates as high as 8.4 mm/yr and an acceleration beginning in 2010 (Donoghue, 2011; Boon, 2012; Sallenger et al., 2012; Ezer et al., 2013; Dangendorf et al., 2017, 2023; Thirion et al., 2024). These increasing trends are accompanied by rises in sea surface temperature (SST), as it is estimated that the Gulf of Mexico has warmed by nearly 0.2ºC/decade, which is twice the warming rate of the global ocean (Li et al., 2022; Wang et al., 2023). Increases in SST may also feed into rises in sea level through sterodynamic effects and the thermal expansion of seawater (Dangendorf et al., 2023). The LC may expedite these growing trends as the eddies that shed from it transport mass and warm waters from the Caribbean Sea to the basin (Thirion et al., 2024).

Some have considered the effects of climate variability and climate change on the physical activity of the basin. It has been suggested that eddy activity in the basin could be impacted by climate modes, such as the Southern Oscillation Index (ENSO or SOI) and the

North Atlantic Oscillation (NAO) (Zhu & Liang, 2022). In regards to climate change, there are contradicting views on the extent of eddy activity, as past observations have demonstrated small but significant decreasing trends in characteristics associated with eddy energetics, such as absolute vorticity and swirling strength (Li et al., 2022). Meanwhile, models have suggested that the frequency of eddy shedding would increase, enhancing activity in the western basin (Alexander et al., 2020; Moreles et al., 2021). The location of eddy separation may also be shifting. The analysis in Meunier et al. (2024) indicates that smaller LCEs tend to detach at higher latitudes and further to the west. Thirion et al. (2024) found that not only have LCEs been larger, but they have been released at relatively lower latitudes in the most recent decade. They were also inclined to be more energetic, have higher amplitudes and exhibit longer lifespans. A linear relationship has been demonstrated between the absolute dynamic topography and the diameter of LCEs, the larger the amplitude, the larger the eddy diameter (Meunier et al., 2024). With increases in sea level anomaly, could it be that a rise in sea level impacts the size of LCEs as noted in most recent observations? A longer record and more realizations in observations are necessary to establish more confidence in these trends, however, statistical significance with these observations and model projections may signify a developing pattern.

Though we lack a complete understanding of LC dynamics and what governs the behavior, rising global temperatures may reveal key mechanisms if we observe evolving attributes. Here we observe and analyze satellite-derived products to explore the influence of climate variability on the dynamics and energetics of the GoM, then connect our findings to theories associated with the LC. This work is organized as follows: Section 3.2 will detail the satellite-derived products utilized in this work and calculations performed. Results will be presented in Section 3.3. Section 3.4 discusses the results and Section 3.5 will summarize our findings.

3.2 Methods and Data

3.2.1 Satellite Derived Products and Reanalysis

Finite Size Lyapunov Exponents (FSLE) can be useful in characterizing transport processes, identifying Lagrangian coherent structures, and quantifying the extent of stirring from the mesoscale and submesoscale (d'Ovidio et al., 2004). FSLEs are computed from the maximum eigenvalue of the Cauchy-Green strain tensor of the geostrophic velocity field obtained from satellite altimetry. FSLEs quantify the rate of separation between two neighboring particles over a finite distance (d'Ovidio et al., 2004; National Centre for Space Studies, 2018). This can be written as

$$\lambda\left(\mathbf{x}, t, \delta_o, \delta_f\right) = \frac{1}{\tau}\log\frac{\delta_f}{\delta_o} \tag{3.1}$$

where λ is the Lyapunov exponent, τ is the time it takes for two particles with a separation distance of d_o to reach a separation distance of d_f (d'Ovidio et al., 2004). Large magnitudes of FSLEs indicate regions of intense stretching by mesoscale velocities (d'Ovidio et al., 2004; National Centre for Space Studies, 2018). For this study, we utilize delayed-time backward-advection FSLEs derived from geostrophic velocities computed from absolute dynamic topography, which approximates attracting Lagrangian coherent structures and is submesoscale-resolving (d'Ovidio et al., 2004; National Centre for Space Studies, 2018; E. U. Copernicus Marine Service Information, 2022). For all λ, $\lambda < 0$, with decreasing values indicating stronger regions of strain. The spatial resolution of the grid is 0.04° × 0.04°, d_o is 0.02°, and d_f is 0.06°. Daily maps of the FSLE product from January 1994 to December 2021 were averaged annually to remove seasonal variability and to characterize annual mesoscale activity (National Centre for Space Studies, 2018). Linear regression was performed on 28 years of annually averaged FSLE data to test the hypothesis that climate change may impact mesoscale stirring, and consequently, submesoscale activity. Significance was determined by the non-parametric Mann-Kendall Test at a 95% confidence level (Mann, 1945; Kendall, 1948). Because this test can have negative bias for relatively shorter datasets, a two-tailed t-test with a 95% confidence level was used to confirm significant results.

Monthly sea level anomalies (SLA) provided by Copernicus Marine Service (CMEMS) were used to characterize mesoscale processes within the GoM (E.U. Copernicus Marine Service Information, 2022). This product merges the along-track measurements of multiple satellite altimeter missions and is processed by the Data Unification Altimeter Combination System (DUACS). The data has been corrected for high frequency variability from atmospheric forcing, long wavelength errors, tidal variability, and the TOPEX-A instrumental drift. The multi-year, altimeter-derived anomalies utilized in this study are suitable for long term trend analysis and are with reference to the mean sea surface height from 1993-2012 (E. U. Copernicus Marine Service Information, 2022). The monthly SLA were time-averaged from daily maps, have a grid resolution of $0.25^{\circ} \times 0.25^{\circ}$, and we select the time period from January 1994 to December 2020 to complement the available surface property data. Because the trend due to glacial isostatic adjustment (GIA) in the GoM is low (< 0.8 mm/yr), we do not correct the SLA data for it (Peltier, 2004).

To estimate surface density for this analysis, monthly sea surface temperature and salinity reanalysis data (GLORYS12v1) were also obtained from CMEMS (E. U. Copernicus Marine Service Information, 2023). The multi-year products have a spatial resolution of $0.083^{\circ} \times 0.083^{\circ}$

and a time period from January 1994 to December 2020 was selected for analysis (E. U. Copernicus Marine Service Information, 2023).

3.2.2 Climate Index Data

Climate indices will be used to explore the relationship between the potential energy of the GoM and interannual climate variability associated with the North Atlantic Oscillation (NAO), the Pacific Decadal Oscillation (PDO), the Southern Oscillation (SOI), and ocean surface temperatures. All index data have been obtained from the National Centers for Environmental Information (NCEI) under the National Oceanic and Atmospheric Administration (NOAA). NAO is based on the difference in sea level pressure between the subtropical high and subpolar low. A strong positive (negative) phase is associated with relatively higher (lower) temperatures and precipitation over the eastern United States (National Centers for Environmental Information, 2024b). PDO is based on ocean temperature anomalies in the northeast and tropical Pacific Ocean. A positive (negative) phase in PDO is associated with cool (warm) ocean surface temperatures in the North Pacific and relatively lower (higher) sea level pressures (National Centers for Environmental Information, 2024c). Variations in PDO can have an effect on the precipitation levels along the Gulf Coast and southern United States (Kurtzman & Scanlon, 2007; Gershunov & Barnett, 1998). SOI, more commonly known as ‘El Nino’ and ‘La Nina’, is based on sea level pressure differences between the western and eastern tropical Pacific Ocean. A positive (negative) phase in SOI is associated with anomalously colder (warmer) ocean temperatures in the eastern tropical Pacific (National Centers for Environmental Information, 2024d). The index record for ocean surface temperature is based on the extended reconstructed sea surface temperature dataset (ERSST) and the anomalies are computed with respect to the average of the 20th century (National Centers for Environmental Information, 2024a). All indices have a monthly temporal resolution.

3.2.3 Characterizing Loop Current Eddies

This study includes a record of LCE separation dates originating from the EddyWatch Program of Horizon Marine, Inc. (Storie et al., 2023; EddyWatch Program, 2024). Of this record, separation dates of LC eddies that completely detached from the LC are included in our analysis. We excluded eddies that reattached to the LC or demonstrated no clear detachment in the SLA data, as we are interested in highlighting the retraction periods that follow shedding events. The surface area (SA) of the shed eddies were determined near the separation date by EddyScan, an eddy identification algorithm that uses SLA to detect user defined boundaries of eddies (Faghmous et al., 2012). Based on a histogram distribution, these eddies were classified into small (SA < 70,000 km^2), medium (70,000 km^2 < SA < 100,000 km^2) and large (SA ≥ 100,000 km^2) sizes.

3.2.4 Empirical Orthogonal Functions

To gain insight into the spatial-temporal variability of SLA in the basin, we compute empirical orthogonal functions and their respective principal components using a Climate Data Toolbox (Greene et al., 2019). This decomposition can be expressed as

$$A(\mathbf{x}, t) = \sum_{n=1}^{N} F_n(\mathbf{x}) a_n(t) \tag{3.2}$$

where A is detrended SLA varying in space and time, $F_n(\mathbf{x})$ are the spatial modes of the empirical orthogonal function and $a_n(t)$ are the time-varying principal components derived from a system of eigenvectors and eigenvalues. The covariance matrix, $R,$ is obtained by

$$R = A * A^T \tag{3.3}$$

which is then decomposed into eigenvectors and eigenvalues. The percent of the variance for each mode can be calculated by dividing the eigenvalues of the covariance matrix by the sum of the diagonal of the covariance matrix from SLA.

3.2.5 Available Surface Potential Energy

Because this analysis is limited to altimetry to understand the energetics of the Gulf of Mexico, we use available surface potential energy (ASPE) to describe the variability in LC potential energy. ASPE is defined as

$$\chi_s = \frac{1}{2} g \rho_o (\eta - \bar{\eta})^2 \tag{3.4}$$

where g is gravity, ρ_o is the surface density, η is the sea surface height, and $\bar{\eta}$ is the local mean reference sea surface height (Huang et al., 2021). Though ASPE does not fully characterize the potential energy of the full water column, it may represent the potential energy associated with the barotropic mode. Anomalies in sea surface height are related to the slope of the thermocline, thus the existence of ASPE is indicative of the existence of available potential energy (Huang et al., 2021). To calculate the local mean reference sea surface height, a 2nd order Butterworth low pass filter with a cut off of ~300 km was used to smooth the mesoscale field. This corresponds to a 9-point average on an SLA grid with a spatial resolution of 0.25º × 0.25º and would provide an appropriately sized reference field for the potential energy of the LC and LCEs.

3.2.6 Total Kinetic Energy

Total kinetic energy (TKE) was computed to explore correlations with ASPE and to characterize the energetics in the western half of the Gulf of Mexico. TKE was derived from geostrophic velocities computed from monthly averaged SLA data. TKE is estimated as follows:

$$TKE = \frac{1}{2}(u^2 + v^2) \tag{3.5}$$

where $u = -\frac{g}{f}\frac{\partial \eta}{\partial y}$ and is the zonal geostrophic velocity component, $v = \frac{g}{f}\frac{\partial \eta}{\partial x}$ and is the meridional geostrophic velocity component, and f is the Coriolis parameter.

3.3 Results

3.3.1 Time Series Regression on FSLEs

Our regression analysis of FSLEs in the GoM presents two notable significant trends in coherent patches: An increasing trend near the western edge of the LC in its extended state and a decreasing trend along the continental shelves and slopes in the northern and western GoM (Figure 3-1(b)). Negative (positive) regression slopes indicate that the value of backward-advection FSLEs are becoming more negative (positive), thus stronger (weaker). Both trends approach a magnitude of 0.001 day^{-1}/yr. To put this value in perspective, if average values of FSLEs increased at this rate over the course of a decade, the average parcels of water would take an additional day to reach the same separation distance. While these trends may be descriptive of patterns in the average strength of mesoscale strain, much care must be taken in their interpretation as these patterns could also signify shifting behaviors in mesoscale stirring patterns. The following analyses attempt to investigate possible explanations for these significant trends.

3.3.2 Investigating the Loop Current Region

The LC presents as a positive SLA with anticyclonic vorticity and is typically outlined by the 17 cm height contour (Leben, 2005; Hamilton et al., 2016). It exhibits two main modes of variability: the extended phase and the retracted phase (Figure 3-1(c) and (d)). Each mode can be associated with general patterns in SLA in the LC region and geostrophic velocities in the Yucatan Channel. During the retracted phase (Figure 3-1(d)), the northward flowing meridional

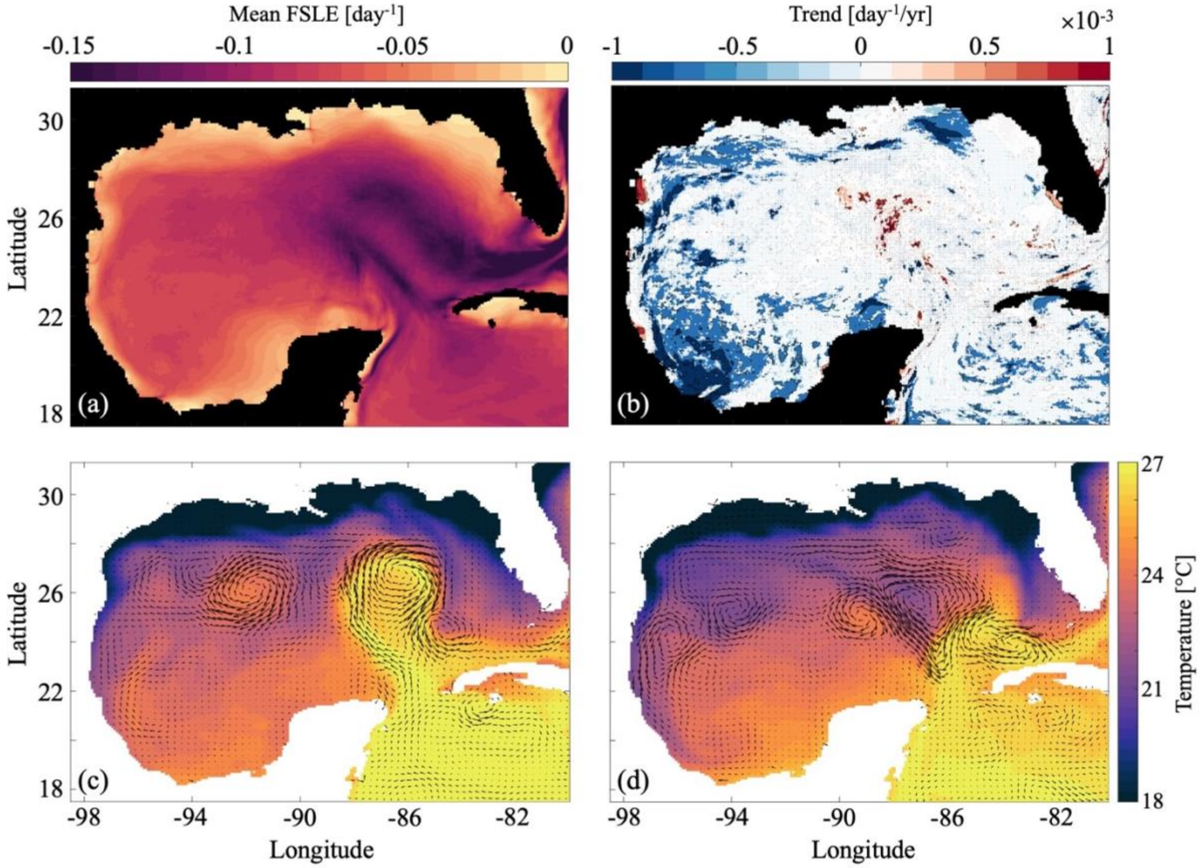

Figure 3-1. Gulf of Mexico hydrography and regression analysis. (a) Basin average FSLE from 1994-2021. (b) Time series regression analysis on FSLEs. Negative trends (blue) suggest increasing strength of FSLEs. Positive trends (red) suggest decreasing strength of FSLEs. White stiplings indicate non-significant trends on a 95% confidence level determined by the Mann-Kendall Test. (c) Monthly averaged SST and geostrophic velocities for January 1998, representing the Loop current in its extended phase. (d) Monthly averaged SST and geostrophic velocities for February 1997, representing the Loop Current in its retracted phase.

velocity through the Yucatan Channel is strongest and resides mainly on the eastern side of the channel. During the extended phase (Figure 3-1(c)), the northward flowing meridional velocity shifts to the western half of the Yucatan Channel and weakens prior to the shedding of a LCE (Abascal et al., 2003; Athié et al., 2015; Hamilton et al., 2016; Lugo-Fernández et al., 2016; Higuera-Parra et al., 2023, Laxenaire et al., 2023; Manta et al., 2023).

We examined SLA and the meridional velocity throughout the region of the LC and the Yucatan Channel over the 27-year period and identified two key regions that highlight these familiar processes. Figure 3-2(b) and (c) displays Hövmoller diagrams of zonal SLA at 24N through the LC and meridional geostrophic velocity across 22N, respectively. On average, SLA became increasingly positive over time, and within the region of the LC (84W to 88W), the amplitudes became larger over time. The shedding of some LCEs can also be detected at this latitude as the 17 cm height contour encompassing a positive SLA drifts westward at approximately 2-5 km/day, as described in literature (Elliott, 1982; Vukovich & Crissman, 1986; Leben, 2005; Ohlmann & Niiler, 2005). The existence or parts of LCFEs can be identified by negative anomalies outlined in yellow, representing the -28 cm height contour (Hiron et al., 2020). Some of these features occur after the shedding of a LCE, are stationary, and have durations ranging from a couple of months to nearly a year. These features tend be strongest and have relatively longer durations after the shedding of a large LCE. This coincides with the LC during the retraction phase, as strong northward-flowing meridional geostrophic velocity is detected at 22N and centered on 85W (eastern side of the Yucatan Channel). As the strong northward meridional velocities subside and shift westward, the strong cyclonic negative SLA vanishes.

Earlier in the time series, this pattern of strong and long signals of negative SLA accompanied by strong and consistent meridional velocity on the eastern side of the Yucatan Channel is infrequent, and when it occurs, the durations are short. From 2010 on, this pattern becomes more frequent and the durations of each event last longer. A wavelet analysis (not shown) also indicates that there is an increased frequency of these events in the latter years of this time series and that the durations span from 9-11 months. As the frequency of these events increase over time, the frequency of eddy shedding decreases.

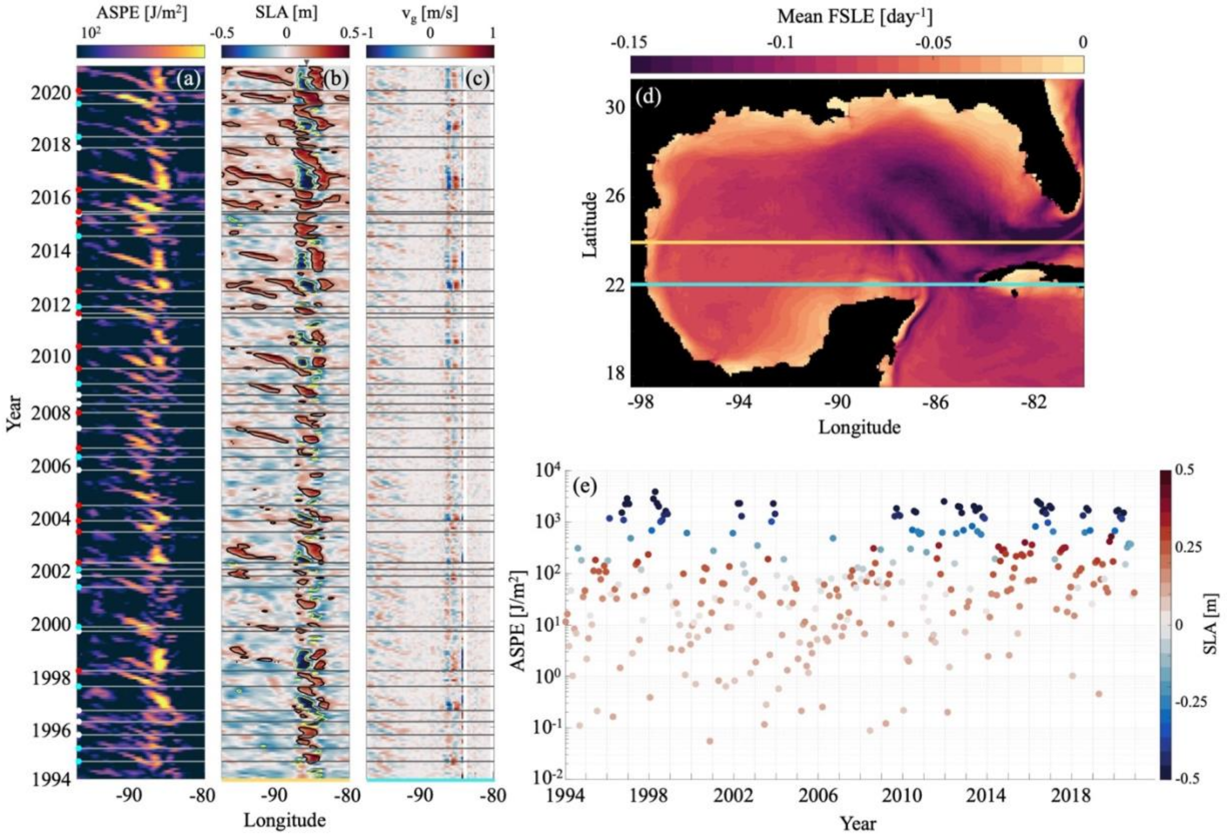

Figure 3-2. Hövmoller diagrams of monthly averaged altimetry-derived products. (a) Meridionally-integrated available surface potential energy (log-scaled) (b) Sea level anomaly (SLA) at 24N. The black contour indicates the 17 cm height contour and the yellow contour indicates the -28 cm height contour. (c) Meridional velocity at 22N. The gray horizontal lines across (a), (b), and (c) indicate the time of Loop Current Eddy shedding events. The white dots on the left of (a) indicate small eddies. The cyan dots indicate medium sized eddies. Red dots indicate large eddies. (d) Basin average FSLE from 1994-2021 with a yellow and blue line to indicate the locations of (b) and (c), respectively. (e) SLA at 24N and 86W as a function of ASPE and year. The gray triangle above (b) indicates 86W.

Empirical orthogonal functions were used to observe the dominant modes of spatial variability in SLA between two date ranges: 1994-2009 and 2010-2021. The first mode describes the LC during the extended phase, with a positive SLA in the LC region (Figure 3-3(c) and (d)). The second mode is representative of the LC during the retracted phase with a negative SLA in place of the extended LC. Figure 3-3(e) and (f) compares the second mode between the two date ranges. Compared to the cyclonic feature detected from 1994-2009, the cyclonic feature detected

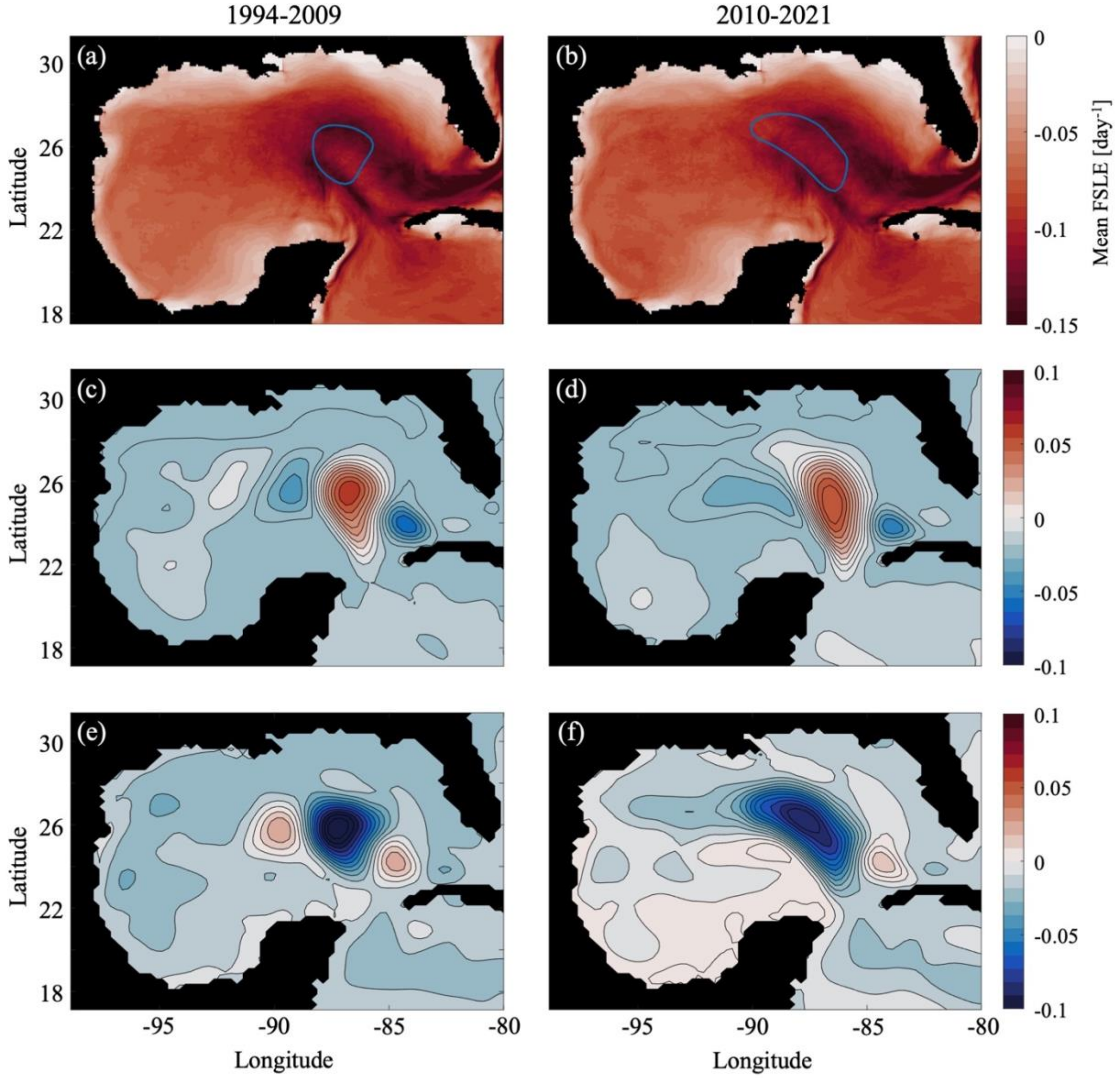

Figure 3-3. Average FSLEs and empirical orthogonal functions for the date ranges 1994-2009 and 2010-2021. (a) and (b) are time-averaged FSLEs between the two date ranges. The blue contour indicates the 2nd mode EOF at -0.05. (c) and (d) are 1st mode EOFs for the two date ranges and represent the Loop Current extended phase. (e) and (f) are the 2nd mode EOFs for the two date ranges and represent the Loop Current retracted phase.

from 2010-2021 is broader and extends towards 28N and -90W. The mode associated with 1994-2009 accounts for 12.6% of the variability within the 16-year time period and the mode associated with 2010-2021 accounts for 15.2% of the variability within the 11-year time period, demonstrating an increased frequency of this mode. Comparing the temporal average FSLE within these two periods (Figure 3-3(a) and (b)), there appears to be a “break” in the LC for the 2010-2021 time period. This break occurs where the cyclonic feature extends northwestward and perhaps not coincidentally, where the increasing trend for FSLEs was detected. These analyses suggest that the increasing trend in FSLEs near the LC may be attributed to longer retraction periods and a disruption in the average flow pattern caused by large, northwestward-extended cyclonic eddies.

3.3.3 Investigating the Shelves

Though the decreasing FSLE trend on the shelves indicates an increase in the strength of mesoscale stirring and strain, it is still consistent with modeling literature that projects the eddy kinetic energy of the Gulf of Mexico to increase (Alexander et al., 2020; Moreles et al., 2021). The eddy kinetic energy in the central- and south-western basin is driven primarily by LCEs, with supporting or opposing influences from wind and buoyancy forcing (Martínez-López & Parés-Sierra, 1998; Teague et al., 2013; Luo et al., 2016; Barkan et al., 2017; Bracco et al., 2019; Justić et al., 2022; Olvera-Prado et al., 2024). The previous section also suggests that the frequency of eddy shedding may decrease with the dynamics associated with the retracted phase. With less eddies shed and advected to the west, what would drive mesoscale stirring to increase?

The available potential energy of the LC and its eddies is released through barotropic and baroclinic instabilities and transferred to kinetic energy, which then influences the energetics of the western basin. To investigate the barotropic component of the available potential energy, we observed the meridionally integrated ASPE in the LC region over time (Figure 3-2(a)). It is evident that the latter half of the time series has more ASPE correlating with the larger, positive amplitudes in SLA. Integrating ASPE from 22N to 28N and 84W to 88W, we isolated the ASPE associated with the LC during the extended phase ($\mathrm{ASPE}_{\mathrm{LC}}$). Because some of this energy is associated with the large cyclonic features in the LC region, and assuming that the energy that advects westward is associated with only positive SLA, we excluded values of $ASPE_{LC}$ that were associated with negative SLA. These values are compared to the TKE of the western basin integrated between 92W and 97W (TKE_{W}) in Figure 3-4(a). There appears to be three phases over this 27-year record, with the first phase occurring from January 1994 to December 2002. During this phase, $ASPE_{LC}$ and TKE_{W} are moderately correlated with a 3-month lag and a correlation value of 0.58 ($p < 0.05$). During the second phase from January 2003 to December 2009, $ASPE_{LC}$ and TKE_{W} are strongly negatively correlated with no lag and a correlation value of -0.80 ($p < 0.05$). During the last phase from January 2010 to December 2021, $ASPE_{LC}$ and TKE_{W} are strongly correlated with a correlation value of 0.76 ($p < 0.05$). While the overall trend of the time series for both $ASPE_{LC}$ and TKE_{W} were significant and positive, the trend associated with 2010-2021 was doubled for $ASPE_{LC}$ and increased by nearly a factor of 6 for TKE_{W}. The trend associated with TKE_{W} was also comparable to the average FSLE trend in the western region, linking the FSLE trend to the ASPE of the LC. These analyses suggest that the increased strength of mesoscale stirring in the western basin may be related to increases in potential energy within the LC.

3.3.4 Intra- and Interannual Climate Variability

Because the potential energy associated with the LC has implications for the energetics throughout the GoM, we assess the relationship between LC dynamics with intra- and interannual variability. To extract intra-annual amplitudes of $ASPE_{LC}$, sinusoids with an annual frequency were fit to the integrated quantity (Figure 3-4(c)). The amplitudes of the fits demonstrated a significant increasing trend over time of approximately 1.6 $kJ/m^2/yr$ based on linear regression. For interannual variability, there were moderate but significant correlations

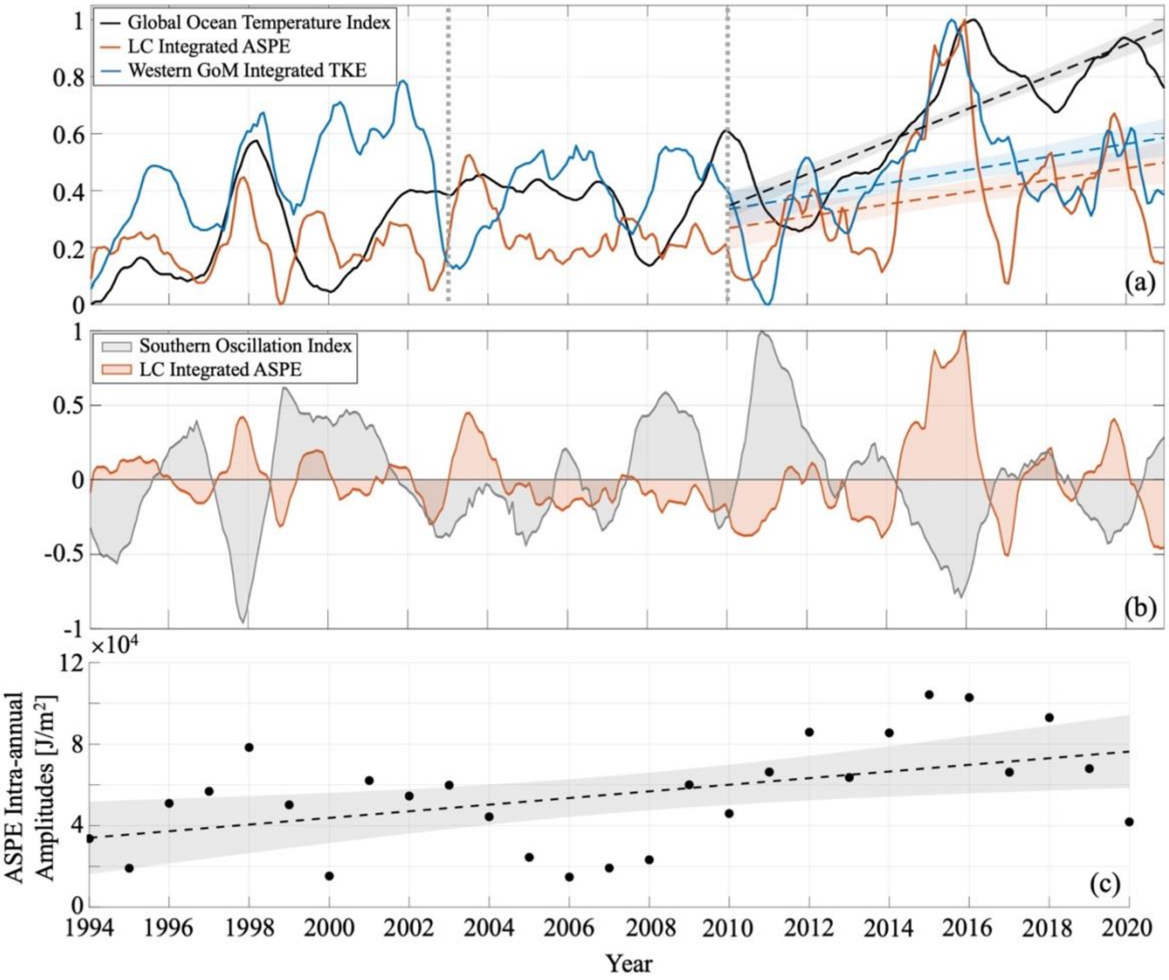

Figure 3-4. Energetic parameters with interannual climate variability indicators. (a) Loop Current ASPE (ASPE$_{LC}$) and TKE of the western basin (TKE$_{W}$) with the global ocean temperature index (normalized). The gray vertical dotted lines indicate the shifts between the different correlation phases. The black, red, and blue dashed lines from 2010-2021 indicate the regression trends of the global ocean temperature index, ASPE$_{LC}$, and TKE$_{W}$ respectively. The shaded regions represent the 95% confidence intervals. (b) Detrended and normalized ASPE$_{LC}$ compared to the Southern Oscillation Index (SOI). (c) Intra-annual amplitudes of Loop Current ASPE. The black dashed line indicates the regression line and the shaded region represents the 95% confidence intervals.

between the time variability in ASPE$_{LC}$ and global climate indices (SOI, NAO, and PDO). Over the entire time series, the correlations associated with SOI (Figure 3-4(b)) and PDO (not shown) were relatively higher with *R*-values of -0.45 and 0.41 ($p < 0.05$), respectively. With NAO, the *R*-value was 0.25 ($p < 0.05$) (not shown). Figure 3-4(a) indicates moderate correlations between

$ASPE_{LC}$ and the global ocean temperature index, with a correlation value of 0.57 ($p < 0.05$) over the entire time series.

3.4 Discussion

Observing trends in Lagrangian tools may highlight shifts in behaviors of dynamical features, and in our case, indicate disruptions in the mean flow patterns of the LC and its associated cyclonic eddies on time scales *O*(1-10 yrs). Although the LC behaves as a nonlinear oscillator (Lugo-Fernández, 2007) and it is difficult to predict its phases, patterns in the behavior have still been identified and our analysis reveals recent deviations. The increasing trend in FSLEs near the extended LC reflects the increasing presence of strong and elongated cyclonic eddies. These eddies have emerged from LCFEs and have been documented to block the intrusion of the Loop Current into the Gulf (Zavala-Hidalgo et al., 2002, 2006; Higuera-Parra et al., 2023). The cyclonic eddies have ASPE values that are at least one order of magnitude higher than the ASPE values associated with the extended LC (Figure 3-2(e)), but for all large cyclonic features detected in this time series, SLA and ASPE remain relatively constant. It is the frequency of these features that changes.

There are a few factors that may contribute to the frequency and duration of the large cyclonic eddies that are subject to intra- and interannual climate variability. While retracted, the LC may leak mass into the cyclonic flow, and variability with transport through the Yucatan Channel may govern the extent of this enhancement (Zavala-Hidalgo et al., 2006). This transport may also be influenced by SOI and NAO (Lugo-Fernández, 2007). Because these cyclonic features result from the merging of LCFEs, the generation frequency and energy levels of LCFEs may be increasing. LCFEs obtain their energy through an inverse energy cascade from the surrounding submesoscale field, which is intensified seasonally from riverine influx (Luo et al., 2016; Barkan et al., 2017; Hiron et al., 2020; Justić et al., 2022). With variability in precipitation increasing and freshwater influx through the Mississippi River anticipated to increase by up to 60% within this century, lateral buoyancy gradients may increase and drive this inverse energy cascade, especially during summer (Morey et al., 2003; Luo et al., 2016; Barkan et al., 2017; Day et al., 2019; Justić et al., 2022; Snedden et al., 2023). LCFEs are the most energetic when LC eddies shed, and with higher levels of kinetic energy, LCFEs have stronger SLAs and larger areas (Hiron et al., 2020). Lastly, the deacceleration of the AMOC may reduce and weaken the transport of the LC, and this may allow the highly energetic cyclonic feature to suppress the current for longer durations and inhibit the current from extending into the basin (Liu et al., 2012; Ezer et al., 2013; Moreles et al., 2021).

While our results suggest that the LC experiences longer retracted phases in more recent years with the prolonged presence of the large cyclonic eddies, it seems to contradict the result that mesoscale stirring highlighted by FSLEs appear to increase in the western basin. Further analysis into the relationship between $\mathrm{ASPE}_{\mathrm{LC}}$ and $\mathrm{TKE}_{\mathrm{W}}$ reveals periodic shifts between positive and negative correlations (Figure 3-4(a)). This calls to question other factors that influence the kinetic energy of the western basin and their relative contributions between these shifts. The eddy kinetic energy of the western GoM is influenced by freshwater forcing near the northern shelf, mesoscale stirring by LCEs in the central and south basin with cross-shelf exchange in the north, and wind forcing all throughout (Martínez-López & Parés-Sierra, 1998; Sutyrin et al., 2003; Vazquez de la Cerda et al., 2005; Vinogradova & Nechaev, 2006; Teague et al., 2013; Luo et al., 2016; Bracco et al., 2019; Gough et al., 2019; Guerrero et al., 2020; Yang et al., 2021; Justić et al., 2022; Olvera-Prado et al., 2023, 2024). Contributions from buoyancy forcing generated by riverine influx demonstrate seasonal variability, and primarily influence energetics of the northern basin (Luo et al., 2016; Barkan et al., 2017; Bracco et al., 2019; Gough et al., 2019; Yang et al., 2021). Since we focus on longer time scales, the kinetic energy was meridionally integrated over the entire basin, and our regression analyses evaluate parameters that were annually averaged or smoothed to remove seasonal variability, we will assume that freshwater forcing does not contribute significantly to the variability of TKE$_{W}$. Model simulations of Olvera-Prado et al. (2024) suggest that the contributions due to wind are influential, yet smaller than the contributions from LCEs. LCEs remain, and two aspects of LCEs have been identified to support our hypothesis on these shifts: eddy shedding frequency and available potential energy.

For 1994-2002 (positive correlation between ASPE$_{LC}$ and TKE$_{W}$), the average shedding periods are relatively longer, as demonstrated in literature and Figure 3-5 (Vukovich, 2012; Lindo-Atichati et al., 2013). The error bars for the average shedding periods, are large, signaling more variability. Positive values of SLA and ASPE are lower compared to the rest of the record (Figure 3-2). For 2003-2009 (negative correlation), the average shedding periods begin to drop to approximately 6 months with less variability (Figure 3-5). Vukovich (2012) and Lindo-Atichati et al. (2013) also reflect this shift, while suggesting that the increased frequency of shed eddies is attributed to a higher average SLA. After 2010 (positive correlation), our results indicate an increase in average shedding period and higher values in SLA and ASPE. This contradicts previous thought that higher average SLA could increase the frequency of shed eddies (Lindo-Atichati et al., 2013; Alexander et al., 2020; Moreles et al., 2021). Our analyses instead suggest that while the frequency of shed eddies may decrease as a result of the suppression of the Loop Current by large cyclonic eddies, the increases in SLA still lead to increases in TKE$_{W}$. Though

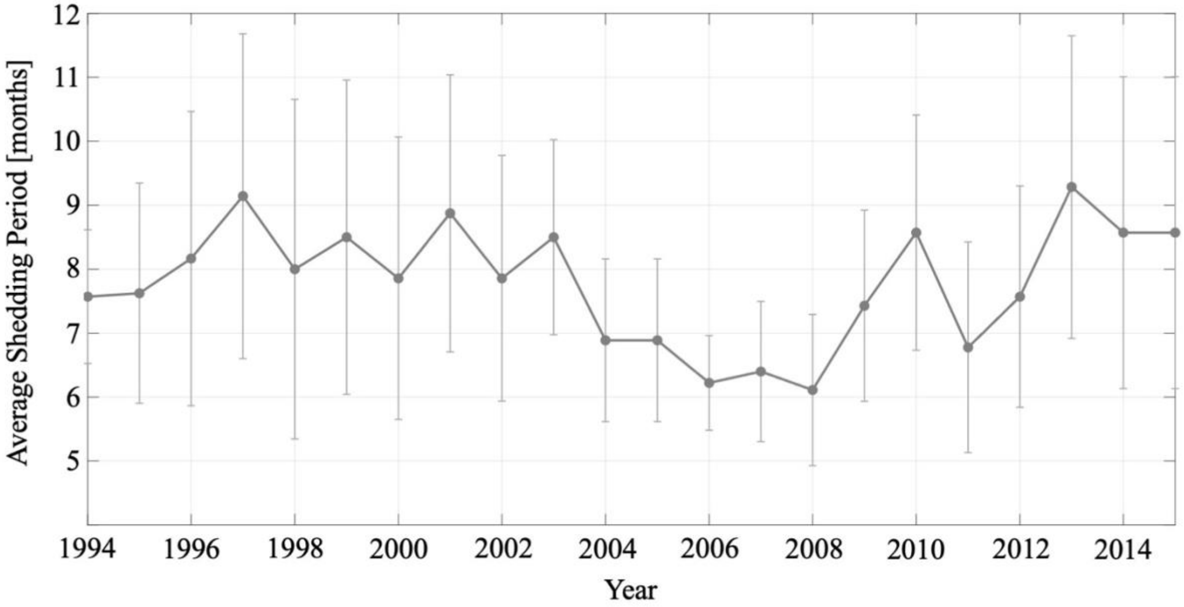

Figure 3-5. Five year running averages of Loop Current eddy shedding periods. Error bars represent standard error at the 95% confidence level.

there are less eddies in more recent years, on average, these eddies carry more energy to the western GoM. On longer times scales (O(1 yr)), the eddy shedding frequency may overshadow the effect of LCE available potential energy on the kinetic energy of the western GoM. The positive correlations between $\mathrm{ASPE}_{\mathrm{LC}}$ and $\mathrm{TKE}_{\mathrm{W}}$ indicate that available potential energy is the main driver of $\mathrm{TKE}_{\mathrm{W}}$, until increases in the frequency of LCE shedding contributes more to the energetics.

Because we have determined that the available potential energy associated with the LC may be the main driver of $\mathrm{TKE}_{\mathrm{W}}$, intra-annual variability in ASPE may reflect the kinetic energy of the western basin on shorter time scales (< O(1 yr)). It is known that LCEs have a tendency to be shed during certain seasons, though not absolute (Chang & Oey, 2012; Hall & Leben, 2016; Limer et al., 2020; Zhu & Liang, 2022); and with seasonal buoyancy forcing from riverine influx, the kinetic energy of the western basin may be higher at certain times of year (Luo et al., 2016; Barkan et al., 2017; Bracco et al., 2019; Gough et al., 2019; Justić et al., 2022). Our results indicate that the amplitudes of the intra-annual variability of ASPE are increasing over time (Figure 3-4(c)). Quantifying the impact of this on the eddy kinetic energy of the western basin is outside the scope of this work, however, it will be important to note this trend in these amplitudes and understand the impact of this variability in our changing climate.

Moderate correlations between ASPE and interannual variability may reflect relationships between these climate modes of variability and the variability of the LC, fluctuations in wind and transport at the Yucatan Channel, surface temperatures, SLA differences, and submesoscale activity through riverine influx (Alexander & Scott, 2002; Kennedy et al., 2007; Kurtzman & Scanlon, 2007; Lugo-Fernández, 2007; Ezer, 2022; Snedden, 2023). For example, wetter years (NAO positive anomalies, SOI negative anomalies) would lead to stronger riverine influx, which may encourage the formation of cyclones through the inverse energy cascade and encourage the formation of LCFEs. The moderate-strong correlation between $ASPE_{LC}$ and global ocean temperatures suggests potential influence of a warming climate on these processes. Increases in SST, and through steric height, SLA would lead to increases in ASPE of the LC, therefore increases in kinetic energy of the western basin. This argument is consistent with previous projections that the kinetic energy in the Gulf of Mexico would increase with climate change (Alexander et al., 2020; Moreles et al., 2021), but also proposes that the frequency of eddy shedding may not be responsible for the rise.

Figure 3-6 summarizes the relationships discussed above through a proposed causal chain. Though multiple factors rooting from climate change may impact the processes investigated here, we focus on increases in SST, sea level rise, and the deceleration of the AMOC. Our observational analysis provides evidence that suggests the influence of these factors on mesoscale stirring patterns. Without increases in sea level, which can be exacerbated by

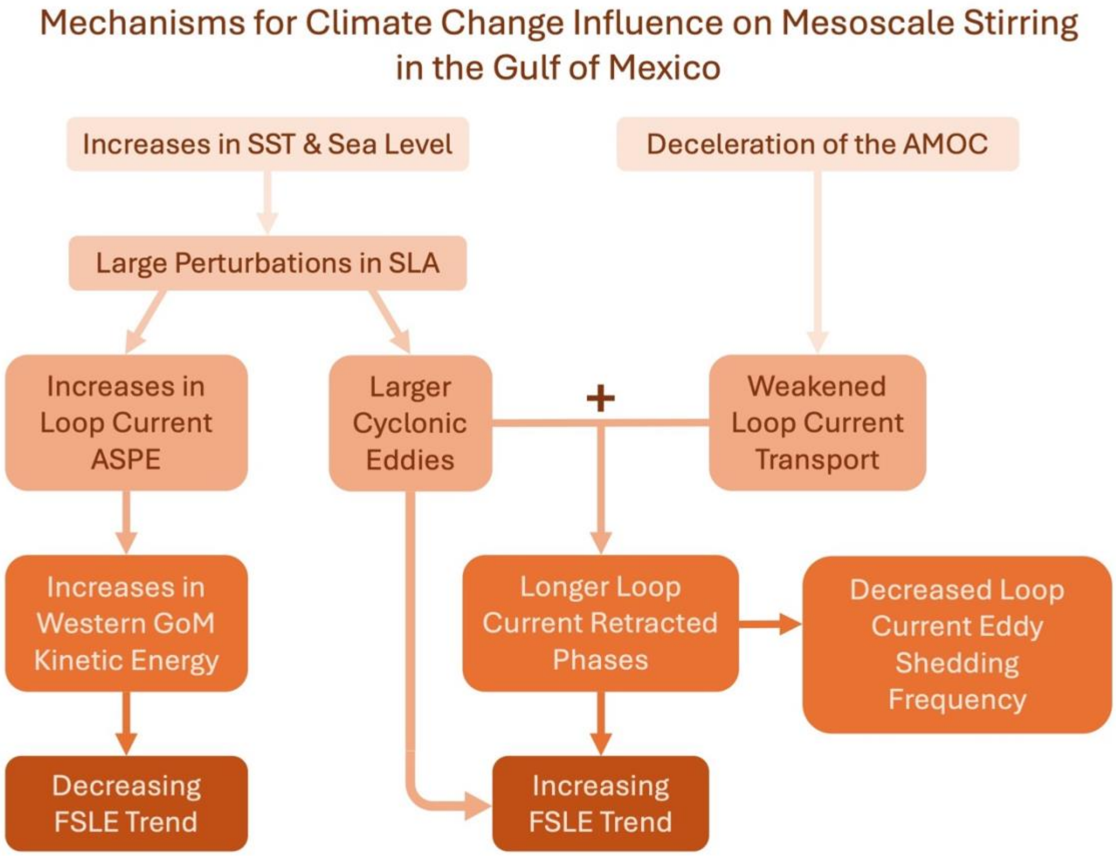

Figure 3-6. Proposed causal chain for shifts in GoM mesoscale stirring patterns.

increases in SST, the potential energy associated with the LC may primarily reflect interannual climate modes of variability on longer time scales, and result in kinetic energy levels with similar patterns in the western basin. Significant trends in FSLEs may not be detectable with this variability. The cyclonic eddies may exhibit the smaller spatial structure in Figure 3-3(e) without increases in SLA, and the “break” in the mean stirring pattern would not exist. If the LC did not experience a weakened transport by the deceleration of the AMOC, then the LC would have more momentum to overcome opposing forces exerted by the large cyclonic eddies. The duration of LC retracted and extended phases and eddy shedding frequency would still vary, but potentially without notable trends. It is important to acknowledge that these results, including the

FSLE regression analysis, are based on short time series (27-28 years) and are not long enough to fully resolve interannual climate variability or assess relationships to climate change. However, the moderate-strong correlations and significant trends found within this data are worthy of attention and could prompt further study and monitoring as records extend.

With less frequent shedding of LC eddies and stronger mesoscale stirring, there is a level of unpredictability as it pertains to the eddy-driven circulation patterns of the Gulf. LCEs carry pockets of heat and salt from the Caribbean Sea into the GoM. Our results imply that although these pockets of heat and salt may be delivered less frequently, when they are advected through the basin, stronger stirring may result in a more effective dissipation of these properties into the interior and across the continental shelves (Teague et al., 2013). This may also impact the interactions between the ocean and atmosphere. Heat from these eddies supply energy to hurricanes and influence atmospheric circulation (Putrasahan et al., 2017; Zhu et al., 2022). When LC eddies are present, these processes may be more intense, however the frequency of these events are uncertain. Additionally, biological processes could be impacted by a shift in these dynamics. LCEs can serve as a predictor for the dispersal potential of coral and fish larvae, as larvae can become trapped and transported in regions of convergence and strain (Bracco et al., 2019; Limer et al., 2020). Less frequent stirring could limit dispersal during spawning periods, however, stronger stirring when eddies are present could disperse larvae at further distances.

3.5 Conclusion

The circulation in the Gulf of Mexico depends largely on the dynamics of the Loop Current. With increases in SST, sea level rise, and a decelerating AMOC, consequent changes to the dynamics in this region continue to be explored. Through time series regression analysis of finite size Lyapunov exponents, we find that the average strength of mesoscale stirring decreases near the Loop Current and increases along continental shelves and slopes, particularly in the western basin. The trends near the LC may be attributed to shifts in average flow patterns, an increased presence of large cyclonic eddies, and prolonged LC retraction phases. Highly energetic, large cyclonic eddies may block the intrusion of the LC, thought to be weakened by the deceleration of the AMOC, and decrease LC eddy shedding frequency. The trends along the continental shelves and slopes in the western Gulf indicate increases in kinetic energy that may be associated with increases in SLA and the availability potential energy of the LC. Some of these dynamics may be influenced by intra- and interannual climate variability, and a longer data record can establish more confidence in the trends observed here. These results have implications for circulation by Loop Current eddies throughout the basin, impacting the exchanges of heat and salt, air-sea interactions, and biological processes.

3.6 Chapter Acknowledgements

Chapter 3, in part, is currently being prepared for submission for publication of the material. McKie, Taylor; MacKinnon, Jennifer; Ricke, Katharine; Lucas, Andrew. The dissertation author was the primary investigator and author of this paper. This material is also based upon work supported by the National Science Foundation Graduate Research Fellowship Program under Grant No. DGE-2038238. We’d also like to acknowledge Sarah Giddings for her support and guidance in the drafting of this chapter.

APPENDICES

Appendix A: Mixed Layer Salinity Budget

A mixed layer salinity budget was performed in an attempt to characterize some of the dynamics observed in the WW profiles as shown in Figure 1-3. This estimation is originally derived from a surface mixed layer heat balance equation which describes the time rate of change of salinity within the mixed layer due to surface freshwater fluxes, advection, turbulent fluxes, shear eddy fluxes, and entrainment (Cronin & McPhaden, 1998). Because of the lack of measurements with the capability to calculate some of these fluxes, the equation has been modified to estimate the change in mixed layer salinity with the acquired measurements. This estimation is expressed as:

$$\frac{\partial S_a}{\partial t} = \frac{1}{H} S_o(E - P) + R \tag{A1}$$

where $\frac{\partial S_a}{\partial t}$ is the time derivative of the average salinity within the mixed layer, H is the mixed layer depth, S_o is the sea surface salinity, E is evaporation, P is precipitation, and R represents advection, turbulent fluxes and entrainment as residual processes and error estimates. The mixed layer depth (MLD) was estimated as the depth where the density is 0.1 kg/m^3 greater than the nearest observed surface density (Chi et al., 2021).

Appendix B: Idealized Profile Parameters

Variables to generate the idealized stratification profiles for GOTM model initializations from Equation 1.1 are displayed in Table B1.

Supplemental Table B1. GOTM idealized stratification profile parameters. Units are as follows: SST [ºC], SSS [psu], N [s^{-2}], z [m], ε [m], and δ [m].

Profile	SST	SSS	N_{ML}	z_{ML}	$\varepsilon_{\mathrm{ML}}$	δ_{ML}	z_1
Deep ML	28	34	0.0001	-50	-5	15	-80
Shallow ML	29	33.5	0.0001	-15	-4	35	-75

Appendix C: Time Series of Surface Forcing for GOTM

Figure C1 depicts the surface forcing for the GOTM 1-D model two-box simulations for Case I, Case II, and the control. The heat fluxes remained the same in all simulations while the precipitation rate and wind speed varied depending on the scenario. Q_{net} is net-zero over the course of 24 hours.

Appendix D: Definition of Turner Angle

To expand the parameter space in considering other compensations in surface lateral thermohaline variability, Turner angle was used to define the bounds for types of compensations. Turner angle, Tu, is defined as

$$Tu = \tan^{-1}\left(\alpha\frac{\partial T}{\partial x} - \beta\frac{\partial S}{\partial x}, \alpha\frac{\partial T}{\partial x} + \beta\frac{\partial S}{\partial x}\right) \qquad (D1)$$

where α is the thermal expansion coefficient, β is the haline contraction coefficient, and the gradients in T and S represent temperature and salinity lateral gradients across a front (McDougall et al., 1988). Figure D1 illustrates a schematic for this concept. If -90º < Tu < -45º, then salinity dominates the lateral changes in density, and the gradient is compensated by temperature. If -45º < Tu < 0º, then the front can also be described salinity-dominated, but a temperature gradient is augmenting the overall density gradient. If 0º < Tu < 45º, the front is temperature-dominated, and a salinity gradient is augmenting the density gradient. And finally, if

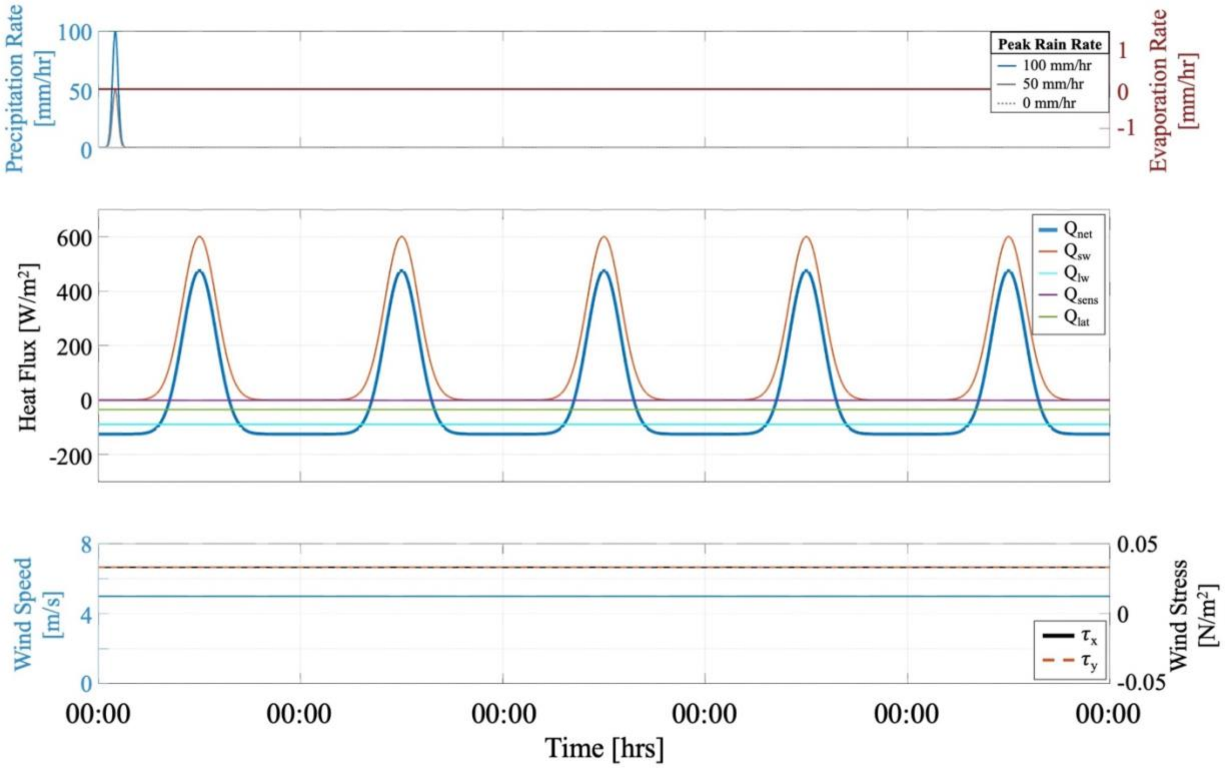

Supplemental Figure C1. Surface forcing for Case I, II, and the control. The top panel describes three precipitation rates and the evaporation rate. The middle panel describes the net, shortwave, longwave, sensible and latent heat fluxes. The last panel describes the wind parameter in both speed and stress.

$45^{\circ} < Tu < 90^{\circ}$, then the front is temperature-dominated and compensated by salinity (Ruddick, 1983). At $Tu = 0^{\circ}$, temperature and salinity are equally contributing to a stable density gradient. At $Tu = -90^{\circ}$ or $Tu = 90^{\circ}$, the front is fully compensated by both temperature and salinity, resulting in a density gradient of 0. For the purpose of this study, ‘reinforcing’ will refer to the shift of a surface lateral gradient towards $Tu = -45^{\circ}$, as precipitation reinforces salinity gradients. ‘Compensating’ refers to a shift away from $Tu = -45^{\circ}$. These definitions contrast from traditional definitions as reinforcing is typically recognized as a shift towards $Tu = 0^{\circ}$.

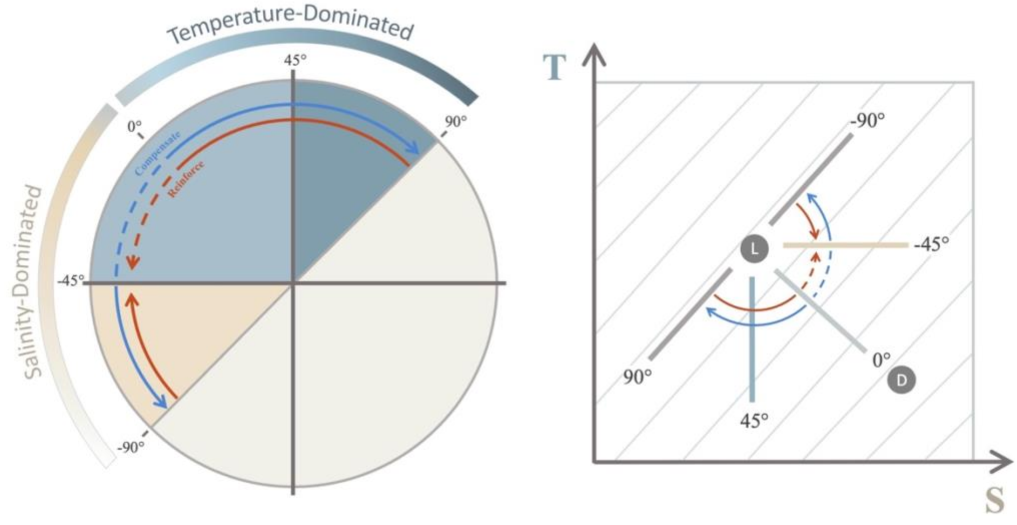

Supplemental Figure D1. Turner angle schematic with a corresponding diagram in T-S space. The red curved arrow indicates the direction of reinforcement and traditionally, is clockwise from Tu = -90º to Tu = 0º or counterclockwise from Tu = 90º to Tu = 0º. The dashed part of the red curved line signifies reinforcement towards salinity gradients. The blue curved arrow indicates the direction of compensation and is clockwise from Tu = 0º to Tu = 90º and counterclockwise from Tu = 0º to Tu = -90º. The dashed part of the blue curved line signifies compensation away from salinity gradients. The gray circles centered with ‘L’ and ‘D’ represent the light and dense side of a density gradient, respectively.

BIBLIOGRAPHY

Abascal, A. J., Sheinbaum, J., Candela, J., Ochoa, J., & Badan, A. (2003). Analysis of flow variability in the Yucatan Channel. *Journal of Geophysical Research: Oceans*, *108*(C12).

Adams, K., MacKinnon, J., Lucas, A. J., Nash, J., Shroyer, E., & Farrar, J. T. (2019). Multi-platform observations of small-scale lateral mixed layer variability in the northern Bay of Bengal. *Deep Sea Research Part II: Topical Studies in Oceanography*, *168*, 104629.

Alexander, M., & Scott, J. (2002). The influence of ENSO on air-sea interaction in the Atlantic. *Geophysical Research Letters*, *29*(14), 46–41.

Alexander, M. A., Shin, S.-I., Scott, J. D., Curchitser, E., & Stock, C. (2020). The response of the Northwest Atlantic Ocean to climate change. *Journal of Climate*, *33*(2), 405–428.

Athié, G., Sheinbaum, J., Leben, R., Ochoa, J., Shannon, M. R., & Candela, J. (2015). Interannual variability in the Yucatan Channel flow. *Geophysical Research Letters*, *42*(5), 1496–1503.

Bachman, S. D., & Taylor, J. R. (2014). Modelling of partially-resolved oceanic symmetric instability. *Ocean Modelling*, *82*, 15–27.

Balaguru, K., Chang, P., Saravanan, R., Leung, L. R., Xu, Z., Li, M., & Hsieh, J.-S. (2012). Ocean barrier layers' effect on tropical cyclone intensification. *Proceedings of the National Academy of Sciences*, *109*(36), 14343–14347.

Barkan, R., McWilliams, J. C., Shchepetkin, A. F., Molemaker, M. J., Renault, L., Bracco, A., & Choi, J. (2017). Submesoscale dynamics in the northern Gulf of Mexico. Part I: Regional and seasonal characterization and the role of river outflow. *Journal of Physical Oceanography*, *47*(9), 2325–2346.

Barkan, R., Molemaker, M. J., Srinivasan, K., McWilliams, J. C., & D'Asaro, E. A. (2019). The role of horizontal divergence in submesoscale frontogenesis. *Journal of Physical Oceanography*, *49*(6), 1593–1618.

Bellenger, H., Drushka, K., Asher, W., Reverdin, G., Katsumata, M., & Watanabe, M. (2017). Extension of the prognostic model of sea surface temperature to rain-induced cool and fresh lenses. *Journal of Geophysical Research: Oceans*, *122*(1), 484–507.

Benshila, R., Durand, F., Masson, S., Bourdallé-Badie, R., de Boyer Montégut, C., Papa, F., & Madec, G. (2014). The upper Bay of Bengal salinity structure in a high-resolution model. *Ocean Modelling*, *74*, 36–52.

Boccaletti, G., Ferrari, R., & Fox-Kemper, B. (2007). Mixed layer instabilities and restratification. *Journal of Physical Oceanography*, *37*(9), 2228–2250.

Boon, J. D. (2012). Evidence of sea level acceleration at US and Canadian tide stations, Atlantic Coast, North America. *Journal of Coastal Research*, *28*(6), 1437–1445.

Bower, A. S., Armi, L., & Ambar, I. (1997). Lagrangian observations of meddy formation during a Mediterranean undercurrent seeding experiment. *Journal of Physical Oceanography*, *27*(12), 2545–2575.

Bracco, A., Liu, G., & Sun, D. (2019). Mesoscale-submesoscale interactions in the Gulf of Mexico: From oil dispersion to climate. *Chaos, Solitons & Fractals*, *119*, 63–72.

Bretherton, F. P. (1972). Atmospheric frontogenesis models: Mathematical formulation and solution. *J. Atmos. Sci*, *29*(1), 1–37.

Buckingham, C. E., Gula, J., & Carton, X. (2021). The role of curvature in modifying frontal instabilities. part i: Review of theory and presentation of a nondimensional instability criterion. *Journal of Physical Oceanography*, *51*(2), 299–315.

Byers, H. R., Moses, H., & Harney, P. J. (1949). Measurement of rain temperature. *Journal of Atmospheric Sciences*, *6*(1), 51–55.

Capet, X., McWilliams, J. C., Molemaker, M. J., & Shchepetkin, A. F. (2008). Mesoscale to submesoscale transition in the California Current System. Part II: Frontal processes. *Journal of Physical Oceanography*, *38*(1), 44–64.

Caulfield, C. P., & Peltier, W. R. (2000). The anatomy of the mixing transition in homogeneous and stratified free shear layers. *Journal of Fluid Mechanics*, *413*, 1–47.

Chang, Y-L, & Oey, L.-Y. (2012). Why does the Loop Current tend to shed more eddies in summer and winter? *Geophysical Research Letters*, *39*(5).

Chang, Yu-Lin, & Oey, L.-Y. (2013). Loop Current growth and eddy shedding using models and observations: Numerical process experiments and satellite altimetry data. *Journal of Physical Oceanography*, *43*(3), 669–689.

Charney, J. G., & Stern, M. E. (1962). On the stability of internal baroclinic jets in a rotating atmosphere. *Journal of the Atmospheric Sciences*, *19*(2), 159–172.

Chérubin, L. M., Morel, Y., & Chassignet, E. P. (2006). Loop Current ring shedding: The formation of cyclones and the effect of topography. *Journal of Physical Oceanography*, *36*(4), 569–591.

Chi, N.-H., Lien, R.-C., & D'Asaro, E. A. (2021). The mixed layer salinity budget in the central equatorial Indian Ocean. *Journal of Geophysical Research: Oceans*, *126*(6), e2021JC017280.

Chi, N.-H., Thompson, E. J., Chen, H., Shcherbina, A., Bingham, F., & Rainville, L. (2023). Spatiotemporal Variability of Rainfall and Surface Salinity in the Eastern Pacific Fresh

Pool: A Joint In Situ and Satellite Analysis During the SPURS-2 Field Campaign. *Journal of Geophysical Research: Oceans*, *128*(12), e2022JC019599.

Chowdary, J. S., Srinivas, G., Fousiya, T. S., Parekh, A., Gnanaseelan, C., Seo, H., & MacKinnon, J. A. (2016). Representation of Bay of Bengal upper-ocean salinity in general circulation models. *Oceanography*, *29*(2), 38–49.

Cronin, Meghan F., & McPhaden, M. J. (1998). Upper ocean salinity balance in the western equatorial Pacific. *Journal of Geophysical Research: Oceans*, *103*(C12), 27567–27587.

Dale, A. C., Barth, J. A., Levine, M. D., & Austin, J. A. (2008). Observations of mixed layer restratification by onshore surface transport following wind reversal in a coastal upwelling region. *Journal of Geophysical Research: Oceans*, *113*(C1).

Dangendorf, S., Marcos, M., Wöppelmann, G., Conrad, C. P., Frederikse, T., & Riva, R. (2017). Reassessment of 20th century global mean sea level rise. *Proceedings of the National Academy of Sciences*, *114*(23), 5946–5951.

Dangendorf, S., Hendricks, N., Sun, Q., Klinck, J., Ezer, T., Frederikse, T., … Törnqvist, T. E. (2023). Acceleration of US Southeast and Gulf coast sea-level rise amplified by internal climate variability. *Nature Communications*, *14*(1), 1–11.

Dauhajre, D. P., & McWilliams, J. C. (2018). Diurnal evolution of submesoscale front and filament circulations. *Journal of Physical Oceanography*, *48*(10), 2343–2361.

Day, J. W., Domínguez, A. L. L., Herrera-Silveria, J., & Kemp, G. P. (2019). Climate change in areas of the Gulf of Mexico with high freshwater input--A review of impacts and potential mitigation. *JAINA, Costas y Mares Ante El Cambio Climático*, *1*(1), 87–108.

de Boyer Montégut, C., Mignot, J., Lazar, A., & Cravatte, S. (2007). Control of salinity on the mixed layer depth in the world ocean: 1. General description. *Journal of Geophysical Research: Oceans*, *112*(C6).

Desbiolles, F., Alberti, M., Hamouda, M. E., Meroni, A. N., & Pasquero, C. (2021). Links between sea surface temperature structures, clouds and rainfall: Study case of the Mediterranean Sea. *Geophysical Research Letters*, *48*(10), e2020GL091839.

DMI COI. (2007). *GHRSST Level 4 DMI OI Global Foundation Sea Surface Temperature Analysis (GDS version 2)*. doi:10.5067/GHGDM-4FD02

Dohan, K. (2021). *Ocean Surface Current Analyses Real-time (OSCAR) Surface Currents - Final 0.25 Degree (Version 2.0)*. doi:10.5067/OSCAR-25F20

Donoghue, J. F. (2011). Sea level history of the northern Gulf of Mexico coast and sea level rise scenarios for the near future. *Climatic Change*, *107*(1), 17–33.

Donohue, Kathleen A., Watts, D. R., Hamilton, P., Leben, R., & Kennelly, M. (2016a). Loop current eddy formation and baroclinic instability. *Dynamics of Atmospheres and Oceans*, *76*, 195–216.

Donohue, K. A., Watts, D. R., Hamilton, P., Leben, R., Kennelly, M., & Lugo-Fernández, A. (2016b). Gulf of Mexico loop current path variability. *Dynamics of Atmospheres and Oceans*, *76*, 174–194.

d’Ovidio, F., Fernández, V., Hernández-García, E., & López, C. (2004). Mixing structures in the Mediterranean Sea from finite-size Lyapunov exponents. *Geophysical Research Letters*, *31*(17).

Drushka, K., Asher, W. E., Ward, B., & Walesby, K. (2016). Understanding the formation and evolution of rain-formed fresh lenses at the ocean surface. *Journal of Geophysical Research: Oceans*, *121*(4), 2673–2689.

Drushka, K., Asher, W. E., Jessup, A. T., Thompson, E. J., Iyer, S., & Clark, D. (2019). Capturing fresh layers with the surface salinity profiler. *Oceanography*, *32*(2), 76–85.

EddyWatch Program, Woods Hole Group, personal communication, March 27, 2024.

Elliott, B. A. (1982). Anticyclonic rings in the Gulf of Mexico. *Journal of Physical Oceanography*, *12*(11), 1292–1309.

E.U. Copernicus Marine Service Information, C. (2022). *Global Ocean Gridded L 4 Sea Surface Heights And Derived Variables Reprocessed 1993 Ongoing*. doi:10.48670/moi-00148

E.U. Copernicus Marine Service Information, C. (2023). *Global Ocean Physics Reanalysis*. doi:10.48670/moi-00021

Ezer, T., Atkinson, L. P., Corlett, W. B., & Blanco, J. L. (2013). Gulf Stream’s induced sea level rise and variability along the US mid-Atlantic coast. *Journal of Geophysical Research: Oceans*, *118*(2), 685–697.

Ezer, T. (2022). Sea level variability in the Gulf of Mexico since 1900 and its link to the Yucatan Channel and the Florida Strait flows. *Ocean Dynamics*, *72*(11), 741–759.

Faghmous, J. H., Styles, L., Mithal, V., Boriah, S., Liess, S., Kumar, V., … dos Santos Mesquita, M. (2012). Eddyscan: A physically consistent ocean eddy monitoring application. *2012 Conference on Intelligent Data Understanding*, 96–103. IEEE.

Ferrari, R., & Rudnick, D. L. (2000). Thermohaline variability in the upper ocean. *Journal of Geophysical Research: Oceans*, *105*(C7), 16857–16883.

Fox-Kemper, B., Ferrari, R., & Hallberg, R. (2008). Parameterization of mixed layer eddies. Part I: Theory and diagnosis. *Journal of Physical Oceanography*, *38*(6), 1145–1165.

Frenger, I., Gruber, N., Knutti, R., & Münnich, M. (2013). Imprint of Southern Ocean eddies on winds, clouds and rainfall. *Nature Geoscience*, *6*(8), 608–612.

George, J. V., Vinayachandran, P. N., Vijith, V., Thushara, V., Nayak, A. A., Pargaonkar, S. M., … Matthews, A. J. (2019). Mechanisms of barrier layer formation and erosion from in situ observations in the Bay of Bengal. *Journal of Physical Oceanography*, *49*(5), 1183–1200.

Gershunov, A., & Barnett, T. P. (1998). ENSO influence on intraseasonal extreme rainfall and temperature frequencies in the contiguous United States: Observations and model results. *Journal of Climate*, *11*(7), 1575–1586.

Gosnell, R., Fairall, C. W., & Webster, P. J. (1995). The sensible heat of rainfall in the tropical ocean. *Journal of Geophysical Research: Oceans*, *100*(C9), 18437–18442.

Goswami, B. N., Venugopal, V., Sengupta, D., Madhusoodanan, M. S., & Xavier, P. K. (2006). Increasing trend of extreme rain events over India in a warming environment. *Science*, *314*(5804), 1442–1445.

Goswami, B. B., Murtugudde, R., & An, S.-I. (2021). Role of the Bay of Bengal warming in the Indian summer monsoon rainfall trend. *Climate Dynamics*, 1–19.

Gough, M. K., Beron-Vera, F. J., Olascoaga, M. J., Sheinbaum, J., Jouanno, J., & Duran, R. (2019). Persistent Lagrangian transport patterns in the northwestern Gulf of Mexico. *Journal of Physical Oceanography*, *49*(2), 353–367.

Greene, C. A., Thirumalai, K., Kearney, K. A., Delgado, J. M., Schwanghart, W., Wolfenbarger, N. S., … Blankenship, D. D. (2019). The climate data toolbox for MATLAB. *Geochemistry, Geophysics, Geosystems*, *20*(7), 3774–3781.

Guerrero, L., Sheinbaum, J., Mariño-Tapia, I., González-Rejón, J. J., & Pérez-Brunius, P. (2020). Influence of mesoscale eddies on cross-shelf exchange in the western Gulf of Mexico. *Continental Shelf Research*, *209*, 104243.

Gula, J., Molemaker, M. J., & McWilliams, J. C. (2014). Submesoscale cold filaments in the Gulf Stream. *Journal of Physical Oceanography*, *44*(10), 2617–2643.

Gula, J., Blacic, T. M., & Todd, R. E. (2019). Submesoscale coherent vortices in the Gulf Stream. *Geophysical Research Letters*, *46*(5), 2704–2714.

Gula, J., Taylor, J., Shcherbina, A., & Mahadevan, A. (2022). Submesoscale processes and mixing. In *Ocean Mixing* (pp. 181–214). Elsevier.

Haine, T. W. N., & Marshall, J. (1998). Gravitational, symmetric, and baroclinic instability of the ocean mixed layer. *Journal of Physical Oceanography*, *28*(4), 634–658.

Hall, C. A., & Leben, R. R. (2016). Observational evidence of seasonality in the timing of loop current eddy separation. *Dynamics of Atmospheres and Oceans*, *76*, 240–267.

Hamilton, P., Berger, T. J., & Johnson, W. (2002). On the structure and motions of cyclones in the northern Gulf of Mexico. *Journal of Geophysical Research: Oceans*, *107*(C12), 1–1.

Hamilton, P., Lugo-Fernández, A., & Sheinbaum, J. (2016). A Loop Current experiment: Field and remote measurements. *Dynamics of Atmospheres and Oceans*, *76*, 156–173.

Hayes, S. P., McPhaden, M. J., & Wallace, J. M. (1989). The influence of sea-surface temperature on surface wind in the eastern equatorial Pacific: Weekly to monthly variability. *Journal of Climate*, *2*(12), 1500–1506.

Haynes, P. H., & McIntyre, M. E. (1987). On the evolution of vorticity and potential vorticity in the presence of diabatic heating and frictional or other forces. *Journal of Atmospheric Sciences*, *44*(5), 828–841.

Higuera-Parra, S., Moreles, E., Olvera-Prado, E. R., & Zavala-Hidalgo, J. (2023). Stratification variability in the Yucatan Channel and its relationship with the Loop Current System. *Frontiers in Marine Science*.

Hiron, L., de la Cruz, B. J., & Shay, L. K. (2020). Evidence of Loop Current frontal eddy intensification through local linear and nonlinear interactions with the Loop Current. *Journal of Geophysical Research: Oceans*, *125*(4), e2019JC015533.

Hosegood, P., Gregg, M. C., & Alford, M. H. (2006). Sub-mesoscale lateral density structure in the oceanic surface mixed layer. *Geophysical Research Letters*, *33*(22).

Hoskins, B. J., Draghici, I., & Davies, H. C. (1978). A new look at the ω-equation. *Quarterly Journal of the Royal Meteorological Society*, *104*(439), 31–38.

Huang, W.-J., Cai, W.-J., Castelao, R. M., Wang, Y., & Lohrenz, S. E. (2013). Effects of a wind-driven cross-shelf large river plume on biological production and CO2 uptake on the Gulf of Mexico during spring. *Limnology and Oceanography*, *58*(5), 1727–1735.

Huang, M., Liang, X., Zhu, Y., Liu, Y., & Weisberg, R. H. (2021). Eddies connect the tropical Atlantic Ocean and the Gulf of Mexico. *Geophysical Research Letters*, *48*(4), e2020GL091277.

Huffman, G. J., Stocker, E. F., Bolvin, D. T., Nelkin, E. J., Jackson, T., & Savtchenko, A. (2019). *GPM IMERG Final Precipitation L3 1 day 0.1 degree x 0.1 degree V06*. doi:10.5067/GPM/IMERGDF/DAY/06

Hurlburt, H. E., & Thompson, J. D. (1980). A numerical study of Loop Current intrusions and eddy shedding. *Journal of Physical Oceanography*, *10*(10), 1611–1651.

Hurlburt, H. E., & Thompson, J. D. (1982). The dynamics of the Loop Current and shed eddies in a numerical model of the Gulf of Mexico. In *Elsevier Oceanography Series* (Vol. 34, pp. 243–297). Elsevier.

Hurlburt, H. E. (1986). Dynamic transfer of simulated altimeter data into subsurface information by a numerical ocean model. *Journal of Geophysical Research: Oceans, 91*(C2), 2372–2400.

Inc., T. M. (2023). *MATLAB version: 23.2.0 (R2023)*. Retrieved from https://www.mathworks.com

Iyer, S., & Drushka, K. (2021). The influence of preexisting stratification and tropical rain modes on the mixed layer salinity response to rainfall. *Journal of Geophysical Research: Oceans, 126*(10), e2021JC017574.

Jaeger, Gualtiero Spiro, Lucas, A. J., & Mahadevan, A. (2020). Formation of interleaving layers in the Bay of Bengal. *Deep Sea Research Part II: Topical Studies in Oceanography, 172,* 104717.

Jaeger, G. Spiro, MacKinnon, J. A., Lucas, A. J., Shroyer, E., Nash, J., Tandon, A., … Mahadevan, A. (2020). How spice is stirred in the Bay of Bengal. *Journal of Physical Oceanography, 50*(9), 2669–2688.

Johnson, L., Lee, C. M., & D’Asaro, E. A. (2016). Global estimates of lateral springtime restratification. *Journal of Physical Oceanography, 46*(5), 1555–1573.

Johnson, L., Lee, C. M., D’Asaro, E. A., Thomas, L., & Shcherbina, A. (2020a). Restratification at a California current upwelling front. Part I: Observations. *Journal of Physical Oceanography, 50*(5), 1455–1472.

Johnson, L., Lee, C. M., D’Asaro, E. A., Wenegrat, J. O., & Thomas, L. N. (2020b). Restratification at a California current upwelling front. Part II: Dynamics. *Journal of Physical Oceanography, 50*(5), 1473–1487.

Johnston, T. M. S., Chaudhuri, D., Mathur, M., Rudnick, D. L., Sengupta, D., Simmons, H. L., … Venkatesan, R. (2016). Decay mechanisms of near-inertial mixed layer oscillations in the Bay of Bengal. *Oceanography, 29*(2), 180–191.

Jouanno, J., Ochoa, J., Pallàs-Sanz, E., Sheinbaum, J., Andrade-Canto, F., Candela, J., & Molines, J.-M. (2016). Loop Current frontal eddies: Formation along the Campeche Bank and impact of coastally trapped waves. *Journal of Physical Oceanography, 46*(11), 3339–3363.

Justić, D., Kourafalou, V., Mariotti, G., He, S., Weisberg, R., Androulidakis, Y., Barker, C., Bracco, A., Dzwonkowski, B., Hu, C., Huang, H., Jacobs, G., Le Henaff, M., Liu, Y., Wiggert, J. (2022). Transport processes in the Gulf of Mexico along the river-Estuary-Shelf-Ocean continuum: A review of research from the Gulf of Mexico research initiative. *Estuaries and Coasts*, 1–37.

Kara, A. B., Rochford, P. A., & Hurlburt, H. E. (2000). An optimal definition for ocean mixed layer depth. *Journal of Geophysical Research: Oceans, 105*(C7), 16803–16821.

Kendall, M. G. (1948). *Rank correlation methods*.

Kennedy, A. J., Griffin, M. L., Morey, S. L., Smith, S. R., & O'Brien, J. J. (2007). Effects of El Niño--Southern Oscillation on sea level anomalies along the Gulf of Mexico coast. *Journal of Geophysical Research: Oceans*, *112*(C5).

Krishnamohan, K. S., Vialard, J., Lengaigne, M., Masson, S., Samson, G., Pous, S., … Madec, G. (2019). Is there an effect of Bay of Bengal salinity on the northern Indian Ocean climatological rainfall? *Deep Sea Research Part II: Topical Studies in Oceanography*, *166*, 19–33.

Kudryavtsev, V. N., & Soloviev, A. V. (1990). Slippery near-surface layer of the ocean arising due to daytime solar heating. *Journal of Physical Oceanography*, *20*(5), 617–628.

Kumar, K. K., Kamala, K., Rajagopalan, B., Hoerling, M. P., Eischeid, J. K., Patwardhan, S. K., … Nemani, R. (2011). The once and future pulse of Indian monsoonal climate. *Climate Dynamics*, *36*(11), 2159–2170.

Kurtzman, D., & Scanlon, B. R. (2007). El Nino--Southern Oscillation and Pacific Decadal Oscillation impacts on precipitation in the southern and central United States: Evaluation of spatial distribution and predictions. *Water Resources Research*, *43*(10).

Large, W. G., McWilliams, J. C., & Doney, S. C. (1994). Oceanic vertical mixing: A review and a model with a nonlocal boundary layer parameterization. *Reviews of Geophysics*, *32*(4), 363–403.

Laxague, N. J. M., & Zappa, C. J. (2020). The impact of rain on ocean surface waves and currents. *Geophysical Research Letters*, *47*(7), e2020GL087287.

Laxenaire, R., Chassignet, E. P., Dukhovskoy, D. S., & Morey, S. L. (2023). Impact of upstream variability on the Loop Current dynamics in numerical simulations of the Gulf of Mexico. *Frontiers in Marine Science*, *10*, 1080779.

Leben, R. R. (2005). Altimeter-derived loop current metrics. *Geophysical Monograph-American Geophysical Union*, *161*, 181.

Le Hénaff, M., Kourafalou, V. H., Morel, Y., & Srinivasan, A. (2012). Simulating the dynamics and intensification of cyclonic Loop Current Frontal Eddies in the Gulf of Mexico. *Journal of Geophysical Research: Oceans*, *117*(C2).

Lerczak, J. A., Hendershott, M. C., & Winant, C. D. (2001). Observations and modeling of coastal internal waves driven by a diurnal sea breeze. *Journal of Geophysical Research: Oceans*, *106*(C9), 19715–19729.

Li, G., Wang, Z., & Wang, B. (2022). Multidecade trends of sea surface temperature, chlorophyll-a concentration, and ocean eddies in the Gulf of Mexico. *Remote Sensing*, *14*(15), 3754.

Li, Q., Bruggeman, J., Burchard, H., Klingbeil, K., Umlauf, L., & Bolding, K. (2021). Integrating CVMix into GOTM (v6. 0): a consistent framework for testing, comparing, and applying ocean mixing schemes. *Geoscientific Model Development*, *14*(7), 4261–4282.

Limer, B. D., Bloomberg, J., & Holstein, D. M. (2020). The influence of eddies on coral larval retention in the flower garden banks. *Frontiers in Marine Science*, *7*, 372.

Lindo-Atichati, D., Bringas, F., & Goni, G. (2013). Loop Current excursions and ring detachments during 1993--2009. *International Journal of Remote Sensing*, *34*(14), 5042–5053.

Lindzen, R. S., & Nigam, S. (1987). On the role of sea surface temperature gradients in forcing low-level winds and convergence in the tropics. *Journal of Atmospheric Sciences*, *44*(17), 2418–2436.

Liu, C., Moncrieff, M. W., & Tuttle, J. D. (2008). A note on propagating rainfall episodes over the Bay of Bengal. *Quarterly Journal of the Royal Meteorological Society: A Journal of the Atmospheric Sciences, Applied Meteorology and Physical Oceanography*, *134*(632), 787–792.

Liu, Y., Lee, S.-K., Muhling, B. A., Lamkin, J. T., & Enfield, D. B. (2012). Significant reduction of the Loop Current in the 21st century and its impact on the Gulf of Mexico. *Journal of Geophysical Research: Oceans*, *117*(C5).

Lucas, A. J., Nash, J. D., Pinkel, R., MacKinnon, J. A., Tandon, A., Mahadevan, A., Omand, M., Freilich, M., Sengupta, D., Ravichandran, M., Le Boyer, A. (2016). Adrift upon a salinity-stratified sea: A view of upper-ocean processes in the Bay of Bengal during the southwest monsoon. *Oceanography*, *29*(2), 134–145.

Lugo-Fernández, A. (2007). Is the Loop Current a chaotic oscillator? *Journal of Physical Oceanography*, *37*(6), 1455–1469.

Lugo-Fernández, A., Leben, R. R., & Hall, C. A. (2016). Kinematic metrics of the Loop Current in the Gulf of Mexico from satellite altimetry. *Dynamics of Atmospheres and Oceans*, *76*, 268–282.

Lugo-Fernández, A. (2023). A new hypothesis on the intrusion of the Loop Current. *Dynamics of Atmospheres and Oceans*, *102*, 101359.

Luo, H., Bracco, A., Cardona, Y., & McWilliams, J. C. (2016). Submesoscale circulation in the northern Gulf of Mexico: Surface processes and the impact of the freshwater river input. *Ocean Modelling*, *101*, 68–82.

MacKinnon, J. A., Nash, J. D., Alford, M. H., Lucas, A. J., Mickett, J. B., Shroyer, E. L., Waterhouse, A., Tandon, A., Sengupta, D., Mahadevan, A., Ravichandran, M., Pinkel, R., Rudnick, D., Whalen, C., Alberty, M., Lekha, J., Fine, E., Chaudhuri, D., Wagner, G. (2016). A tale of two spicy seas. *Oceanography*, *29*(2), 50–61.

MacKinnon, J. A., Simmons, H. L., Hargrove, J., Thomson, J., Peacock, T., Alford, M. H., Barton, B., Boury, S., Brenner, S., Couto, N., Danielson, S., Fine, E., Graber, H., Guthrie, J., Hopkins, J., Jayne, S., Jeon, C., Klenz, T., Lee, C., Lenn, Y., Lucas, A., Lund, B., Mahaffey, C., Norman, L., Rainville, L., Smith, M., Thomas, L., Torres-Valdéz, S., Wood, K. (2021). A warm jet in a cold ocean. *Nature Communications*, *12*(1), 2418.

Mahadevan, A., Jaeger, G. S., Freilich, M., Omand, M. M., Shroyer, E. L., & Sengupta, D. (2016). Freshwater in the Bay of Bengal: Its fate and role in air-sea heat exchange. *Oceanography*, *29*(2), 72–81.

Mann, H. B. (1945). Nonparametric tests against trend. *Econometrica: Journal of the Econometric Society*, 245–259.

Manta, G., Durante, G., Candela, J., Send, U., Sheinbaum, J., Lankhorst, M., & Laxenaire, R. (2023). Predicting the Loop Current dynamics combining altimetry and deep flow measurements through the Yucatan Channel. *Frontiers in Marine Science*, *10*, 1156159.

Marshall, J. C., & Nurser, A. J. G. (1992). Fluid dynamics of oceanic thermocline ventilation. *Journal of Physical Oceanography*, *22*(6), 583–595.

Marshall, J., Jones, H., Karsten, R., & Wardle, R. (2002). Can eddies set ocean stratification? *Journal of Physical Oceanography*, *32*(1), 26–38.

Martínez-López, B., & Parés-Sierra, A. (1998). Circulation in the Gulf of Mexico induced by tides, wind and the Yucatan Current. *Ciencias Marinas*, *24*(1), 65–93.

McDougall, T. J., Thorpe, S. A., & Gibson, C. H. (1988). Small-scale turbulence and mixing in the ocean: A glossary. *Small-Scale Turbulence and Mixing in the Ocean*, Vol. 3. Elsevier.

McKie, T., Lucas, A. J., & MacKinnon, J. (2024). Submesoscale Dynamics in the Bay of Bengal: Inversions and Instabilities. *Journal of Geophysical Research: Oceans*, *129*(3), e2023JC020563.

McKie, T., Johnson, L., Schlosser, T., MacKinnon, J., & Lucas, A. (2024). *Precipitating Fronts on the Bay of Bengal*. doi:10.5061/dryad.59zw3r2gr

McKie, T., Lucas, A., & MacKinnon, J. (2023). *Submesoscale dynamics in the Bay of Bengal: Inversions and instabilities*. doi:10.5061/dryad.6q573n644

McWilliams, J. C. (1985). Submesoscale, coherent vortices in the ocean. *Reviews of Geophysics*, *23*(2), 165–182.

McWilliams, J. C. (2016). Submesoscale currents in the ocean. *Proceedings of the Royal Society A: Mathematical, Physical and Engineering Sciences*, *472*(2189), 20160117.

Meroni, A. N., Parodi, A., & Pasquero, C. (2018). Role of SST patterns on surface wind modulation of a heavy midlatitude precipitation event. *Journal of Geophysical Research: Atmospheres*, *123*(17), 9081–9096.

Meunier, T., Bower, A., Pérez-Brunius, P., Graef, F., & Mahadevan, A. (2024). The Energy Decay of Warm-Core Eddies in the Gulf of Mexico. *Geophysical Research Letters*, *51*(1), e2023GL106246.

Minobe, S., Kuwano-Yoshida, A., Komori, N., Xie, S.-P., & Small, R. J. (2008). Influence of the Gulf Stream on the troposphere. *Nature*, *452*(7184), 206–209.

Mishra, A. K., Nagaraju, V., Rafiq, M., & Chandra, S. (2019). Evidence of links between regional climate change and precipitation extremes over India. *Weather*, *74*(6), 218–221.

Moreles, E., Zavala-Hidalgo, J., Martínez-López, B., & Ruiz-Angulo, A. (2021). Influence of stratification and Yucatan Current transport on the Loop Current Eddy shedding process. *Journal of Geophysical Research: Oceans*, *126*(1), e2020JC016315.

Morey, S. L., Martin, P. J., O'Brien, J. J., Wallcraft, A. A., & Zavala-Hidalgo, J. (2003). Export pathways for river discharged fresh water in the northern Gulf of Mexico. *Journal of Geophysical Research: Oceans*, *108*(C10).

Moulin, A. J., Moum, J. N., Shroyer, E. L., & Hoecker-Martínez, M. (2021). Freshwater lens fronts propagating as buoyant gravity currents in the equatorial Indian Ocean. *Journal of Geophysical Research: Oceans*, *126*(8), e2021JC017186.

Munk, W. (1967). *Waves Across the Pacific*. The Lamont-Columbia University Marine Science Film Series.

Munk, W., Armi, L., Fischer, K., & Zachariasen, F. (2000). Spirals on the sea. *Proceedings of the Royal Society of London. Series A: Mathematical, Physical and Engineering Sciences*, *456*(1997), 1217–1280.

National Centre for Space Studies, N. (2018). *FSLE - Maps of Finite Size Lyapunov Exponents and Orientations of the associated eigenvectors*. doi:10.24400/527896/a01-2022.002

National Centers for Environmental Information, N. (2024a). *North Atlantic Oscillation (NAO)*. Retrieved from https://ncei.noaa.gov/access/monitoring/nao/

National Centers for Environmental Information, N. (2024b). *Pacific Decadal Oscillation (PDO)*. Retrieved from https://ncei.noaa.gov/access/monitoring/pdo/

National Centers for Environmental Information, N. (2024c). *Southern Oscillation Index (SOI)*. Retrieved from https://ncei.noaa.gov/access/monitoring/enso/soi/

National Centers for Environmental Information, N. (2024d). *The Global Anomalies and Index Data*. doi:ncei.noaa.gov/access/monitoring/global-temperature-anomalies/anomalies

Nof, D., & Pichevin, T. (2001). The ballooning of outflows. *Journal of Physical Oceanography*, *31*(10), 3045–3058.

Nof, D. (2005). The momentum imbalance paradox revisited. *Journal of Physical Oceanography*, *35*(10), 1928–1939.

Oey, L., Ezer, T., & Lee, H. (2005). Loop Current, rings and related circulation in the Gulf of Mexico: A review of numerical models and future challenges. *Geophysical Monograph-American Geophysical Union*, *161*, 31.

Oey, L. Y. (2008). Loop Current and deep eddies. *Journal of Physical Oceanography*, *38*(7), 1426–1449.

Ohlmann, J. C., & Niiler, P. P. (2005). Circulation over the continental shelf in the northern Gulf of Mexico. *Progress in Oceanography*, *64*(1), 45–81.

Olvera-Prado, E. R., Romero-Centeno, R., Zavala-Hidalgo, J., Moreles, E., & Ruiz-Angulo, A. (2023). Contribution of the wind, Loop Current Eddies, and topography to the circulation in the southern Gulf of Mexico. *Ocean Dynamics*, *73*(10), 597–618.

Olvera-Prado, E. R., Morey, S. L., & Chassignet, E. P. (2024). Contribution of the wind and Loop Current eddies to the circulation in the western Gulf of Mexico. *Frontiers in Marine Science*, *11*, 1185849.

Papa, F., Durand, F., Rossow, W. B., Rahman, A., & Bala, S. K. (2010). Satellite altimeter-derived monthly discharge of the Ganga-Brahmaputra River and its seasonal to interannual variations from 1993 to 2008. *Journal of Geophysical Research: Oceans*, *115*(C12).

Pei, S., Shinoda, T., Soloviev, A., & Lien, R.-C. (2018). Upper ocean response to the atmospheric cold pools associated with the Madden-Julian Oscillation. *Geophysical Research Letters*, *45*(10), 5020–5029.

Peltier, W. R. (2004). Global glacial isostasy and the surface of the ice-age Earth: the ICE-5G (VM2) model and GRACE. *Annu. Rev. Earth Planet. Sci.*, *32*, 111–149.

Pichevin, T., & Nof, D. (1997). The momentum imbalance paradox. *Tellus A*, *49*(2), 298–319.

Pinkel, Robert, Goldin, M. A., Smith, J. A., Sun, O. M., Aja, A. A., Bui, M. N., & Hughen, T. (2011). The Wirewalker: A vertically profiling instrument carrier powered by ocean waves. *Journal of Atmospheric and Oceanic Technology*, *28*(3), 426–435.

Pinkel, R., Nguyen, S., Smith, J. A., Lucas, A. J., Reineman, B. D., & Waterhouse, A. F. (2023). Vertical momentum transport by internal gravity waves above the equatorial undercurrent at 140 W. *Geophysical Research Letters*, *50*(14), e2022GL101630.

Putrasahan, D. A., Kamenkovich, I., Le Hénaff, M., & Kirtman, B. P. (2017). Importance of ocean mesoscale variability for air-sea interactions in the Gulf of Mexico. *Geophysical Research Letters*, 44(12), 6352-6362.

Ramachandran, S., & Tandon, A. (2020). Generation of submesoscale temperature inversions below salinity fronts in the Bay of Bengal. *Journal of Geophysical Research: Oceans*, *125*(12), e2020JC016278.

Ramachandran, S., Tandon, A., Mackinnon, J., Lucas, A. J., Pinkel, R., Waterhouse, A. F., Nash, J., Shroyer, E., Mahadevan, A., Weller, R., Farrar, J. (2018). Submesoscale processes at shallow salinity fronts in the Bay of Bengal: Observations during the winter monsoon. *Journal of Physical Oceanography*, *48*(3), 479–509.

Reverdin, G., Supply, A., Drushka, K., Thompson, E. J., Asher, W. E., & Lourenço, A. (2020). Intense and small freshwater pools from rainfall investigated during SPURS-2 on 9 November 2017 in the eastern tropical Pacific. *Journal of Geophysical Research: Oceans*, *125*(2), e2019JC015558.

Rousset, C., & Beal, L. M. (2010). Observations of the Florida and Yucatan Currents from a Caribbean cruise ship. *Journal of Physical Oceanography*, *40*(7), 1575–1581.

Ruddick, B. (1983). A practical indicator of the stability of the water column to double-diffusive activity. *Deep Sea Research Part A. Oceanographic Research Papers*, *30*(10), 1105–1107.

Rudnick, D. L., & Luyten, J. R. (1996). Intensive surveys of the Azores Front: 1. Tracers and dynamics. *Journal of Geophysical Research: Oceans*, *101*(C1), 923–939.

Rudnick, D. L., & Martin, J. P. (2002). On the horizontal density ratio in the upper ocean. *Dynamics of Atmospheres and Oceans*, *36*(1–3), 3–21.

Rudnick, D. L., Zarokanellos, N. D., & Tintoré, J. (2022). A four-dimensional survey of the Almeria--Oran Front by underwater gliders: tracers and circulation. *Journal of Physical Oceanography*, *52*(2), 225–242.

Sallenger, A. H., Jr, Doran, K. S., & Howd, P. A. (2012). Hotspot of accelerated sea-level rise on the Atlantic coast of North America. *Nature Climate Change*, *2*(12), 884–888.

Sarkar, S., Pham, H. T., Ramachandran, S., Nash, J. D., Tandon, A., Buckley, J., … Omand, M. M. (2016). The interplay between submesoscale instabilities and turbulence in the surface layer of the Bay of Bengal. *Oceanography*, *29*(2), 146–157.

Schott, F. A., Xie, S.-P., & McCreary, J. P., Jr. (2009). Indian Ocean circulation and climate variability. *Reviews of Geophysics*, *47*(1).

Sengupta, D., Bharath Raj, G. N., & Shenoi, S. S. C. (2006). Surface freshwater from Bay of Bengal runoff and Indonesian throughflow in the tropical Indian Ocean. *Geophysical Research Letters*, *33*(22).

Sengupta, D., Bharath Raj, G. N., Ravichandran, M., Sree Lekha, J., & Papa, F. (2016). Near-surface salinity and stratification in the north Bay of Bengal from moored observations. *Geophysical Research Letters*, *43*(9), 4448–4456.

Serra, N., Ambar, I., & Käse, R. H. (2005). Observations and numerical modelling of the Mediterranean outflow splitting and eddy generation. *Deep Sea Research Part II: Topical Studies in Oceanography*, *52*(3–4), 383–408.

Shackelford, K., DeMott, C. A., Van Leeuwen, P. J., Thompson, E., & Hagos, S. (2022). Rain-Induced Stratification of the Equatorial Indian Ocean and Its Potential Feedback to the Atmosphere. *Journal of Geophysical Research: Oceans*, *127*(3), e2021JC018025.

Shackelford, K., DeMott, C. A., Jan van Leeuwen, P., Mazloff, M. R., & Sun, R. (2024). A cold lid on a warm ocean: Indian Ocean surface rain layers and their feedbacks to the atmosphere. *Journal of Geophysical Research: Atmospheres*, *129*(4), e2023JD039272.

Shcherbina, A. Y., D'Asaro, E. A., Lee, C. M., Klymak, J. M., Molemaker, M. J., & McWilliams, J. C. (2013). Statistics of vertical vorticity, divergence, and strain in a developed submesoscale turbulence field. *Geophysical Research Letters*, *40*(17), 4706–4711.

Shcherbina, A. Y., Sundermeyer, M. A., Kunze, E., D'Asaro, E., Badin, G., Birch, D., Brunner-Suzuki, A., Callies, J., Kuebel Cervantes, B., Claret, M., Concannon, B., Early, J., Ferrari, R., Goodman, L., Harcourt, R., Klymak, J., Lee, C., Pascale Lelong, M., Levine, M., Lien, R., Mahadevan, A., McWilliams, J., Molemaker, M., Mukherjee, S., Nash, J., Özgökmen, T., Pierce, S., Ramachandran, S., Samelson, R., Sanford, T., Shearman, R., Skyllingstad, E., Smith, K., Tandon, A., Taylor, J., Terray, E., Thomas, L, Ledwell, J. (2015). The LatMix summer campaign: Submesoscale stirring in the upper ocean. *Bulletin of the American Meteorological Society*, *96*(8), 1257–1279.

Shcherbina, A. Y., D'Asaro, E. A., & Harcourt, R. R. (2019). Rain and sun create slippery layers in eastern Pacific fresh pool. *Oceanography (Washington, DC)*, *32*(2), 98.

Sheinbaum, J., Candela, J., Badan, A., & Ochoa, J. (2002). Flow structure and transport in the Yucatan Channel. *Geophysical Research Letters*, *29*(3), 10–11.

Sheinbaum, J., Athié, G., Candela, J., Ochoa, J., & Romero-Arteaga, A. (2016). Structure and variability of the Yucatan and loop currents along the slope and shelf break of the Yucatan channel and Campeche bank. *Dynamics of Atmospheres and Oceans*, *76*, 217–239.

Shenoi, S. S. C., Shankar, D., & Shetye, S. R. (2002). Differences in heat budgets of the near-surface Arabian Sea and Bay of Bengal: Implications for the summer monsoon. *Journal of Geophysical Research: Oceans*, *107*(C6), 5–1.

Sherin, V. R., Girishkumar, M. S., Shivaprasad, S., Sureshkumar, N., Farrar, J. T., Athulya, K., Ashin, K., Pattabhi Rama Rao, E., Sengupta, D., Venkatesan, R., Ravichandran, M. (2023). Importance of Seasonally Evolving Near-Surface Salinity Stratification on Mixed Layer Heat Budget During Summer Monsoon Intraseasonal Oscillation in the Northern Bay of Bengal in 2019. *Journal of Geophysical Research: Oceans*, *128*(11), e2023JC019800.

Shetye, S. R., Shenoi, S. S. C., Gouveia, A. D., Michael, G. S., Sundar, D., & Nampoothiri, G. (1991). Wind-driven coastal upwelling along the western boundary of the Bay of Bengal during the southwest monsoon. *Continental Shelf Research*, *11*(11), 1397–1408.

Shroyer, E. L., Gordon, A. L., Jaeger, G. S., Freilich, M., Waterhouse, A. F., Farrar, J. T., Sarma, V.V.S.S., Venkatesan, R., Weller, R., Moum, J., Mahadevan, A. (2020). Upper layer thermohaline structure of the Bay of Bengal during the 2013 northeast monsoon. *Deep Sea Research Part II: Topical Studies in Oceanography*, *172*, 104630.

Shroyer, E., Tandon, A., Sengupta, D., Fernando, H. J. S., Lucas, A. J., Farrar, J. T., Chattopadhyay, R., de Szoeke, S., Flatau, M., Rydbeck, A., Wijesekera, H., McPhaden, M., Seo, H., Subramanian, A., Venkatesan, R., Joseph, J., Ramsundaram, S., Gordon, A., Bohman, S., Pérez, J., Simoes-Sousa, I., Jayne, S., Todd, R., Bhat, G.S., Lankhorst, M., Schlosser, T., Adams, K., Jinadasa, S. U. P., Mathur, M., Mohapatra, M., Pattabhi Rama Rao, E., Sahai, A. K., Sharma, R., Lee, C., Rainville, L., Cherian, D., Cullen, K., Centurioni, L., Hormann, V., MacKinnon, J., Send, U., Anutaliya, A., Waterhouse, A., Black, G., Dehart, J., Woods, K., Creegan, E., Levy, G., Kantha, L., Subrahmanyam, B. (2021). Bay of Bengal intraseasonal oscillations and the 2018 monsoon onset. *Bulletin of the American Meteorological Society*, *102*(10), E1936–E1951.

Snedden, G. A. (2023). ENSO and NAO linkages to interannual salinity variability in north central Gulf of Mexico estuaries through teleconnections with precipitation. *Estuarine, Coastal and Shelf Science*, *293*, 108487.

Soloviev, A. V., Matt, S., & Fujimura, A. (2015). Three-dimensional dynamics of freshwater lenses in the ocean's near-surface layer. *Oceanography*, *28*(1), 142–149.

Spall, M. A. (1995). Frontogenesis, subduction, and cross-front exchange at upper ocean fronts. *Journal of Geophysical Research: Oceans*, *100*(C2), 2543–2557.

Spiro Jaeger, G., & Mahadevan, A. (2018). Submesoscale-selective compensation of fronts in a salinity-stratified ocean. *Science Advances*, *4*(2), e1701504.

Strobach, E., Klein, P., Molod, A., Fahad, A. A., Trayanov, A., Menemenlis, D., & Torres, H. (2022). Local air-sea interactions at ocean mesoscale and submesoscale in a Western boundary current. *Geophysical Research Letters*, *49*(7), e2021GL097003.

Storie, J., Ramos, R., Leber, M., Nowak, H., Young, M., & Magnell, B. (2023). Evaluation of Loop Current/Loop Current Eddy Fronts to guide offshore oil & gas operations. *Offshore Technology Conference*, D031S035R002. OTC.

Sturges, W., & Leben, R. (2000). Frequency of ring separations from the Loop Current in the Gulf of Mexico: A revised estimate. *Journal of Physical Oceanography*, *30*(7), 1814–1819.

Sutyrin, G. G., Rowe, G. D., Rothstein, L. M., & Ginis, I. (2003). Baroclinic eddy interactions with continental slopes and shelves. *Journal of Physical Oceanography*, *33*(1), 283–291.

Taylor, J. R., & Ferrari, R. (2010). Buoyancy and wind-driven convection at mixed layer density fronts. *Journal of Physical Oceanography*, *40*(6), 1222–1242.

Taylor, J. R., & Ferrari, R. (2011). Ocean fronts trigger high latitude phytoplankton blooms. *Geophysical Research Letters*, *38*(23).

Taylor, J. R., & Thompson, A. F. (2023). Submesoscale dynamics in the upper ocean. *Annual Review of Fluid Mechanics*, *55*, 103–127.

Teague, W. J., Wijesekera, H. W., Jarosz, E., Fribance, D. B., Lugo-Fernández, A., & Hallock, Z. R. (2013). Current and hydrographic conditions at the East Flower Garden Bank in 2011. *Continental Shelf Research*, *63*, 43–58.

Thadathil, P., Gopalakrishna, V. V., Muraleedharan, P. M., Reddy, G. V., Araligidad, N., & Shenoy, S. (2002). Surface layer temperature inversion in the Bay of Bengal. *Deep Sea Research Part I: Oceanographic Research Papers*, *49*(10), 1801–1818.

Thadathil, P., Muraleedharan, P. M., Rao, R. R., Somayajulu, Y. K., Reddy, G. V., & Revichandran, C. (2007). Observed seasonal variability of barrier layer in the Bay of Bengal. *Journal of Geophysical Research: Oceans*, *112*(C2).

Thadathil, P., Suresh, I., Gautham, S., Prasanna Kumar, S., Lengaigne, M., Rao, R. R., … Hegde, A. (2016). Surface layer temperature inversion in the Bay of Bengal: Main characteristics and related mechanisms. *Journal of Geophysical Research: Oceans*, *121*(8), 5682–5696.

Thangaprakash, V. P., Girishkumar, M. S., Suprit, K., Kumar, N. S., Chaudhuri, D., Dinesh, K., Kumar, A., Shivaprasad, S., Ravichandran, M., Farrar, J., Sundar, R., Weller, R. (2016). What controls seasonal evolution of sea surface temperature in the Bay of Bengal? Mixed layer heat budget analysis using moored buoy observations along 90 E. *Oceanography*, *29*(2), 202–213.

Thirion, G., Birol, F., & Jouanno, J. (2024). Loop Current eddies as a possible cause of the rapid sea level rise in the Gulf of Mexico. *Journal of Geophysical Research: Oceans*, *129*(3), e2023JC019764.

Thomas, L. N. (2005). Destruction of potential vorticity by winds. *Journal of Physical Oceanography*, *35*(12), 2457–2466.

Thomas, L. N. (2008). Formation of intrathermocline eddies at ocean fronts by wind-driven destruction of potential vorticity. *Dynamics of Atmospheres and Oceans*, *45*(3–4), 252–273.

Thomas, L. N., Tandon, A., & Mahadevan, A. (2008). Submesoscale processes and dynamics. *Ocean Modeling in an Eddying Regime*, *177*, 17–38.

Thomas, L. N., Taylor, J. R., Ferrari, R., & Joyce, T. M. (2013). Symmetric instability in the Gulf Stream. *Deep Sea Research Part II: Topical Studies in Oceanography*, *91*, 96–110.

Thomas, L. N., Taylor, J. R., D’Asaro, E. A., Lee, C. M., Klymak, J. M., & Shcherbina, A. (2016). Symmetric instability, inertial oscillations, and turbulence at the Gulf Stream front. *Journal of Physical Oceanography*, *46*(1), 197–217.

Thompson, E. J., Moum, J. N., Fairall, C. W., & Rutledge, S. A. (2019). Wind limits on rain layers and diurnal warm layers. *Journal of Geophysical Research: Oceans*, *124*(2), 897–924.

Tokay, A., & Short, D. A. (1996). Evidence from tropical raindrop spectra of the origin of rain from stratiform versus convective clouds. *Journal of Applied Meteorology and Climatology*, *35*(3), 355–371.

Toy, M. D., & Johnson, R. H. (2014). The influence of an SST front on a heavy rainfall event over coastal Taiwan during TiMREX. *Journal of the Atmospheric Sciences*, *71*(9), 3223–3249.

Tozuka, T., & Cronin, M. F. (2014). Role of mixed layer depth in surface frontogenesis: The Agulhas Return Current front. *Geophysical Research Letters*, *41*(7), 2447–2453.

Vallis, G. K. (2017). *Atmospheric and oceanic fluid dynamics*. Cambridge University Press.

Van Roekel, L., Adcroft, A. J., Danabasoglu, G., Griffies, S. M., Kauffman, B., Large, W., … Schmidt, M. (2018). The KPP boundary layer scheme for the ocean: Revisiting its formulation and benchmarking one-dimensional simulations relative to LES. *Journal of Advances in Modeling Earth Systems*, *10*(11), 2647–2685.

Vázquez de la Cerda, A. M., Reid, R. O., DiMarco, S. F., Jochens, A. E., Sturges, A., & Lugo-Fernández, A. (2005). *Circulation in the Gulf of Mexico: observations and models*. Geophysical Monograph Series 161, American Geophysical Union, Washington, DC.

Vecchi, G. A., & Harrison, D. E. (2002). Monsoon breaks and subseasonal sea surface temperature variability in the Bay of Bengal. *Journal of Climate*, *15*(12), 1485–1493.

Veneziani, M., Griffa, A., Garraffo, Z., & Mensa, J. A. (2014). Barrier layers in the tropical South Atlantic: Mean dynamics and submesoscale effects. *Journal of Physical Oceanography*, *44*(1), 265–288.

Vinayachandran, P. N., Murty, V. S. N., & Ramesh Babu, V. (2002). Observations of barrier layer formation in the Bay of Bengal during summer monsoon. *Journal of Geophysical Research: Oceans*, *107*(C12), SRF-19.

Vinayachandran, P. N., Shankar, D., Vernekar, S., Sandeep, K. K., Amol, P., Neema, C. P., & Chatterjee, A. (2013). A summer monsoon pump to keep the Bay of Bengal salty. *Geophysical Research Letters*, *40*(9), 1777–1782.

Vinogradova, N. T., & Nechaev, D. A. (2006). Impacts of frontal stability and topography on cross-shelf exchange in the Northern Gulf of Mexico. *Journal of Oceanography*, *62*, 667–680.

Vukovich, F. M., & Crissman, B. W. (1986). Aspects of warm rings in the Gulf of Mexico. *Journal of Geophysical Research: Oceans*, *91*(C2), 2645–2660.

Vukovich, F. M. (2012). Changes in the Loop Current's Eddy shedding in the period 2001--2010. *International Journal of Oceanography*, *2012*.

Wang, Z., Boyer, T., Reagan, J., & Hogan, P. (2023). Upper-Oceanic Warming in the Gulf of Mexico between 1950 and 2020. *Journal of Climate*, *36*(8), 2721–2734.

Wijesekera, H. W., Paulson, C. A., & Huyer, A. (1999). The effect of rainfall on the surface layer during a westerly wind burst in the western equatorial Pacific. *Journal of Physical Oceanography*, *29*(4), 612–632.

Wijesekera, Hemantha W., Shroyer, E., Tandon, A., Ravichandran, M., Sengupta, D., Jinadasa, S. U. P., Fernando, H., Agrawal, N., Arulananthan, K., Bhat, G. S., Baumgartner, M., Buckley, J., Centurioni, L, Conry, P., Farrar, J., Gordon, A., Hormann, V., Jarosz, E., Jensen, T., Johnston, S., Lankhorst, M., Lee, C., Leo, L., Lozovatsky, I., Lucas, A., Mackinnon, J., Mahadevan, A., Nash, J., Omand, M., Pham, H., Pinkel, R., Rainville, L., Ramachandran, S., Rudnick, D., Sarkar, S., Send, U., Sharma, R., Simmons, H., Stafford, K., Laurent, L., Venayagamoorthy, K., Venkatesan, R., Teague, W., Wang, D., Waterhouse, A., Weller, R., Whalen, C. (2016). ASIRI: An ocean--atmosphere initiative for Bay of Bengal. *Bulletin of the American Meteorological Society*, *97*(10), 1859–1884.

Yang, Y., Weisberg, R. H., Liu, Y., & San Liang, X. (2020). Instabilities and multiscale interactions underlying the loop current eddy shedding in the Gulf of Mexico. *Journal of Physical Oceanography*, *50*(5), 1289–1317.

Yang, Y., McWilliams, J. C., San Liang, X., Zhang, H., Weisberg, R. H., Liu, Y., & Menemenlis, D. (2021). Spatial and temporal characteristics of the submesoscale energetics in the Gulf of Mexico. *Journal of Physical Oceanography*, *51*(2), 475–489.

You, Y. (2002). A global ocean climatological atlas of the Turner angle: implications for double-diffusion and water-mass structure. *Deep Sea Research Part I: Oceanographic Research Papers*, *49*(11), 2075–2093.

Yu, L., & McPhaden, M. J. (2011). Ocean preconditioning of Cyclone Nargis in the Bay of Bengal: Interaction between Rossby waves, surface fresh waters, and sea surface temperatures. *Journal of Physical Oceanography*, *41*(9), 1741–1755.

Zavala-Hidalgo, Jorge, Morey, S. L., & O'Brien, J. J. (2002). On the formation and interaction of cyclonic eddies with the Loop Current using NCOM and a suite of observations. *OCEANS'02 MTS/IEEE*, *3*, 1463–1466. IEEE.

Zavala-Hidalgo, J., Morey, S. L., O'brien, J. J., & Zamudio, L. (2006). On the Loop Current eddy shedding variability. *Atmósfera*, *19*(1), 41–48.

Zheng, B., Lucas, A. J., Pinkel, R., & Le Boyer, A. (2022). Fine-scale velocity measurement on the Wirewalker wave-powered profiler. Journal of Atmospheric and Oceanic Technology, 39(2), 133-147.

Zhu, Y., & Liang, X. (2022). Characteristics of Eulerian mesoscale eddies in the Gulf of Mexico. *Frontiers in Marine Science, 9*, 1087060.